Laser Fabricated Plasmonic Nanoparticle Templates For Sensor Applications

Jacob Leonard Spear

A thesis submitted in partial fulfillment of the requirements of Nottingham Trent University for the degree of Doctor of Philosophy

29th June 2019

Abstract

Traditionally, localised surface plasmon resonance, LSPR, spectroscopy sensing surfaces are produced with a highly specific functionalised layer atop a plasmonic nanostructure. Here we present that by removing this functionalisation, not only is the difficulty of the fabrication procedure reduced, but the '*naked*' plasmonic nanoparticle template is still able to act as a high quality optical sensing surface for detecting the surface abundance of a lead salt, showing a clear and measurable shift to the optical response of the template from as little as $0.0001 at\%$ or $100 ppm$.

The increased desire for flexible devises is driving a need to be able to fabricate a high quality micro- and nano-structures on flexible substrates. This research describes a methodology for the laser fabrication of a plasmonic nanoparticle template on a polymer substrate by modifying the polymer surface to increase the surface roughness of the polymer substrate and the inclusion of a silicon dioxide interlayer between the polymer and the metallic thin film. By combining these two processes, laser annealing can be transplanted onto a substrate as thermally sensitive as PET and still allow for the fabrication of a plasmonic nanoparticle template, with the highest quality template being produced with a $PET/SiO_2(100nm)/Ag(10nm)$ structure.

Through the a simultaneous experimental and computational investigation of the effect an interlayer has on the laser annealing process, caused by multiple reflections within a silica interlayer. Demonstrating a direct correlation between the experimentally seen variance of the processing window - increased threshold energy and a reduction to the ablation limit with the calculated minimum and maximum absorption of the laser line in the silver thin film. Allowing this understanding to provide an additional control on the laser annealing process.

Further to this, a novel optical characterisation technique to assess the angle and polarisation dependent reflectance, at both specular and diffuse angels. Due to the lack of a commercially available system to measure this effect, a custom designed and built goniometric system to accurately and reliably quantify this effect was produced. The analysis of the angle and polarisation dependent reflectance of the nanoparticle templates revealed that the S-polarisation reflectance showed minimal (up to a maximum of 5 nm) variation at any angle of incidence, while the P-polarisation reflectance showed a dramatic blue shift to the LSPR peak of the nanoparticle templates at steep angles (above 50°). This colour changing phenomenon can be attributed to a combination of thin film interference, and the differing planes being probed by the two separate polarisations.

Acknowledgments

Before anyone else, I must thank Rebecca Palfrey. Firstly because I made a promise that I would. But more importantly, because without her this journey would never have begun - for this I both love and hate you.

I can say with certainty that I am lucky to have had Dr. Demosthenes Koutsogeorgis as my Director of Studies. He has provided me with more support, guidance, wonderful discussions, time, effort and attention than I could have hoped for. Especially during the times when I wouldn't have minded a little less! For this and so much more I thank you.

I have been lucky enough to work with an excellent supervisory team consisting of Prof. Carl Brown and Dr. Christopher Castleton. I thank you both for your time, wonderful advice, encouragement and above all else your willingness to answer my endless and often nonsensical questions.

To Dr. Nikos Kalfagiannis, I offer special thanks. You showed me the ropes but never let me hang myself. I will always be grateful.

It has been my great honor to have worked with: Prof. Panos Patsalas and group at the Aristotle Univesity of Thessaloniki; Dr. Lefteris Lidorikis and group at the University of Ioannina; as well as Prof. Wayne Cranton and Mr. Stuart Creasey at Sheffield Hallam University. Without your patience, insight, patience, guidance and patience I could not have achieved what I have. For letting my loose in your labs, I offer my eternal gratitude and will forever be in your debt.

From the bottom of my heart I thank the NTU technician team, in particular: Mr. Dave Parker; Mr. Phil Aubrey; Mr. Chris Mutton; Mr. Ryan Toms. You wonderful people do not get half the gratitude that you deserve. Thank you.

To my colleagues, past and present, in iSMART, I must first say sorry! You poor people had to put up with me for 4 years! I thank you for your support and for allowing me to work beside some of the most passionate people I have had the fortune to meet.

Finally, to my family, friends and in particular AZKABANTS. It is not possible to tell you how grateful to you I am. This has not been a straight or easy road, and you were there through it all, wishing me the best and ready to lend a hand, advice or a drink whenever it was needed. There are no words for how much I love you, or for how thankful I am that you are part of my life.

If you don't know physics and you don't know Greek, what do you know?

Contents

List of Figures

Chapter 1

Introduction

Plasmonics is a field that has gained remarkable popularity over the course of the last 20 years. However, despite the vast amount of new research occurring all around the world, the effect being exploited has been known and exploited for a thousand years by glass-smiths. This cannot be seen more clearly than when looking at the *Lycurgus Cup*, as shown in figure 1.1. The Lycurgus cup, and the field of plasmonics unique optical phenomena stems from the localised surface plasmon resonance effect. This is a resonant oscillation of the surface electrons of a nanostructure caused by the coupling of an incident photon with a corresponding frequency.

Figure 1.1: Image of the Lycurgus Cup, from the British Museum. The cup appears green when viewed with an external light source (left), while when viewed with an internal light source the cup appears red (right).

The LSPR effect results in a significant increase in the scattering and absorption cross-section of the nanostructure, where this is characterised by a Lorentz peak specific to the material, size, shape, surface distribution and local dielectric environment of the nanostructure. This effect has been achieved with a variety of different materials, but most commonly the coinage metals: copper; silver; and gold, with silver allowing for a LSPR response across the visible wavelength region.

Plasmonic nanostructures have been shown to offer superior performance in a wide range of applications, including but not limited to: solar cells; memory devices; cancer treatment; and optical sensing. Due to the extreme correlation of the exact spectral position of the LSPR peak to the local dielectric environment, optical sensing with plasmonic nanostructures has been able to show single molecule detection, identification of drug delivery to specific binding sites and *in situ* process monitoring. To date, despite the vast array of research work, there are a very limited number of commercially available plasmonic devices, and of that limited number, they are predominantly sensors or sensing techniques. To date, there has been extensive investigations, both experimental and theoretical, into the mechanics of the laser annealing process on a silicon substrate. But there has been limit development of a laser fabricated nanostructure on a more versatile substrate such as a polymer.

1.1 Research Aim

The primary aim of this research is to investigate the sensor and sensing applications of metallic plasmonic nanoparticle templates fabricated with a unique laser annealing methodology. Beyond this, the aim is to develop several sensors or sensing techniques on a known substrate (silicon) as well as on new substrates, such as polymers.

1.2 Research Objectives

Here we will present the research objectives of this research work.

- Identify LSPR focused optical sensors and sensing techniques.
- Investigate the use of laser fabricated plasmonic nanoparticle templates, on a silicon substrate, in a sensing application.
- Preform laser annealing on a polymer substrate.
- Optimise the laser annealing process on a polymer substrate.

- Investigate the use of laser fabricated plasmonic nanoparticle templates, on a polymer substrate, in a sensing application.

Chapter 2

Literature Review

2.1 Introduction

This chapter will present and discuss the background information and leading literature on the phenomenon of the localised surface plasmon resonance effect, its applications, with focus on its' use within sensing, and how the effect is characterised. Further to this we will present photonic processing for nanostructuring and how this relates to this research.

2.2 Plasmonics

Plasmonics is a relatively new, but rapidly developing field within nanophotonics, which is dedicated to understanding and exploiting the interactions between electromagnetic fields and matter at an interface between a metal and a dielectric medium. One of the many advantages of plasmonics, is the remarkable fact that the underlying mechanisms involved are firmly rooted within a classical electromagnetism approach, based on Maxwell's equations, a free electron gas and an understanding of the negative real component of the dielectric function. While as a field of active research plasmonics is relatively new, being prominent for the last 30 years with predictions for plasmonic effects appearing as early as 1957 [3], the optical effect that this field describes have been exploited by glassmiths for centuries when producing red and yellow stained glass.

To understand the optical properties any given material you must first consider their complex dielectric function. This allows for a prediction of the variation in optical response based on the spectral regime that the material is illuminated by. However, in the case of metals and metal-like materials within plasmonics, the dielectric function can be used to predict their optical behaviour. As we see in our daily lives metals like gold and silver, for electromagnetic (EM) radiation or fields with frequencies up to and including the visible spectrum, are highly reflective and do not allow EM fields to penetrate deeply into them (skin depth) or even to travel through them. However, at higher frequencies, such as in the ultra-violet (UV) region and beyond, the behaviour of these metals shifts, and they gain characteristics more generally associated with dielectric materials, due to absorptions between electron levels within the metal. This phenomenon, in conjunction with the electron band transitions of the noble metals, particularly in the case of a metal like gold, result in significant absorption bands at these frequencies, allowing for a fuller description of a metals optical properties.

This behaviour can be quantified and explained using the modified Drude model, or *plasma model*, where we can consider a free electron gas oscillating against fixed position positive ion cores. Using the Drude model allows us to fully describe the optical properties and behaviour of metals over varying spectral regions depending on their band structures. However, this method cannot be used exclusively to fully describe these properties, but it can be used until the presence of interband transitions, at certain frequency regions, be it below at or above the visible frequencies, limit the validity of this approach [4, 5].

While the Drude model can be used as a basis for describing the optical properties, the complex dielectric function, $\varepsilon(\omega)$, can be used across the entire electromagnetic spectrum and can be used at a more fundamental level to categorise a material, where the equation defining the complex dielectric function can bee see in equation 2.1. In equation 2.1, $\varepsilon(\omega)$ is the frequency dependent dielectric constant, ω_p is the plasma frequency of the free electron gas, ω is the frequency of the electric field and γ is the collision frequency $(1/\tau)$. When an electromagnetic field is incident onto a metal, the oscillation of the electrons within the metal changes in response to this applied field. This induced oscillation is inherently damped by the relaxation time (τ) of the free electron gas. This induced motion of the electrons caused by the applied field itself induces an additional independent electromagnetic field. This induced field is out of phase with the applied field and the combination of these two fields contributes dramatically to the overall macroscopic polarisation.

$$\varepsilon(\omega) = \frac{\omega_p^2}{\omega^2 + i\gamma\omega} \tag{2.1}$$

To fully categorise the optical properties of a material, while it is possible to use the dielectric function, more commonly, optical materials are grouped based on their complex refractive index. The refractive index can be calculated from the dielectric function, where the complex index, $n(\omega)$, is defined as: $n(\omega) = \sqrt{\varepsilon(\omega)}$ [6]. By solving Maxwell's equations, we can derive the dielectric function of this free electron gas, where considering this equation at different frequency regimes, such as when $\omega < \omega_p$ where traditional metals behave with their characteristic metallic optical behaviour.

2.2.1 Surface Plasmon Polariton and Localised Surface Plasmon Resonance

The field of plasmonics focuses its attention on the interaction of light with metallic surfaces at a dielectric interface, such as air and one of the noble or coinage metals (gold, silver and copper). However, this field can be subdivided into two main areas of research, surface plasmon polaritons (SPP) and localised surface plasmon resonance (LSPR) [7, 8].

SPP's are a type of dispersive evanescent surface wave that occur at a single, flat interface between a dielectric medium and a metallic film, where SPP's can be initiated by either an electron or photon interaction [9–11]. For the case of either photon or electron excitation, for this effect to be realised, vitally the incident momentum of the photon or electron must match and be able to couple directly to that of the free electron gas at the metal's surface. As such, to achieve a SPP, a coupling system is required to achieve the necessary momentum matching. This coupling can be achieve with a prism or a waveguide in one of two primary configurations, either where the matching system is in direct contact with the metal surface, as in the case of the Kretschmann configuration [12, 13] or where there is a dielectric gap between the matching system and the metal, as used by the Otto configuration [14, 15]. Most commonly, the Otto configuration is used with a waveguide mating system. To assess SPP's, a monochromatic light source is illuminated on to the matching system, be it either a prism or a waveguide, at a specific angle to induce the surface wave.

Similarly, yet distinctly different, is the localised surface plasmon resonance, LSPR, effect. The LSPR effect is a non-propagating, resonant oscillation of the conducting electrons at interface between the surface of a metallic nanostructure and a dielectric material such as air. Unlike SPP, LSPR can only be triggered by an incident photon, when this incident photons frequency can couple to the plasma frequency of the free electron gas. Due to the nature of the nanostructure surface inherent to the LSPR effect, the incident light can couple directly to the nanostructure, completely removing the need for a complex matching system. Once coupled, the free electron gas oscillates against the restoring force of the positive nuclei. This resonant oscillation causes several changes to the optical properties of the nanostructure, including a significant increase to its' scattering and absorption cross section. This can be attributed to the induced oscillation, as we can now consider the nanostructure to be behaving as a dipole [16]. In addition to this, the induced oscillation leads to an amplification of the local electric field, internally and in the near-field zone around the nanostructure [6, 17, 18]. In contrast to SPP's, the unique optical properties of the LSPR effect can be assessed with relatively simple equipment and processes *via* far-field optical techniques such as reflectance, transmission and absorption spectroscopy. LSPR can be assessed with such relatively simple techniques due to the presence of a characteristic Lorentz peak associated with the LSPR effect. The exact spectral position and bandwidth of this peak is highly dependent on a number of factors including: the size; shape; composition and distribution of the nanostructure; and the exact nature of the dielectric environment that the nanostructure experiences [6, 19–21], as can be seen in figure 2.1.

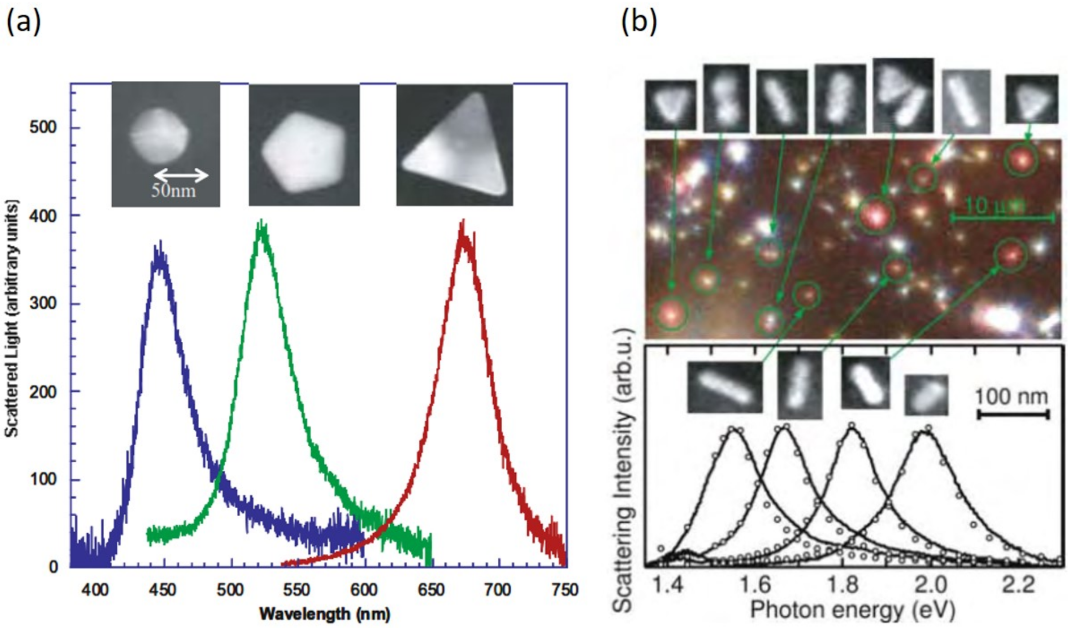

Figure 2.1: Image a) Dark-field scattering spectra of individual silver nanoparticles, showing the dependence of the spectral position of the LSPR peak and the shape. Image b) Optical dark-field images and corresponding scattering spectra for light incident along the long axis of the asymmetric nanoparticles. Images taken from [1].

2.3 Applications of Plasmonics

Since its inception, plasmonics has become a key, and in some cases vital, component or factor within a remarkable number of diverse devices and application spread across a wide range of fields [8]. Plasmonic nanostructures have found a place in: solar cells [22, 23] improving their efficiency by introducing scatting centres; cancer therapy [24, 25] by exploiting a photo-thermal effect; non-volatile memory devices [26, 27] acting as a charge trapping layer; and wave guides [28–31] allowing for 2D mode-confinement perpendicular to the propagation plane. While potentially the most abundant and well-known application of plasmonics is sensing [8]. Due to the unique optical properties of plasmonic nanostructures, they have allowed for the development of existing sensing methodologies and have even enabled the creating of techniques that could not exist without this plasmonic behaviour [32].

Perhaps the most famous sensing methodology to utilise a plasmonic nanostructure is surface enhanced Raman scattering (SERS) [8, 33]. SERS functions by exploiting the LSPR effect to locally enhance the electric field of either the incident, or scattered illumination to enhance the detectable signal. Since the discovery of an increased Raman signal from a roughened silver electrode [34], surface enhanced Raman spectroscopy has become one of the most widely used analysis techniques used across all areas of scientific research [35]. SERS has allowed for increased signal to noise ratio my many orders of magnitude, enhanced sensitivity and remarkable chemical identification at increasingly lower and lower concentrations. SERS is a prime example of a plasmonic nanostructure allowing for the improvement of an existing sensing technique [36–38], where Raman scattering has progressed from being limited by inherently low signal and has progressed to detecting micro-, nano-, femto- and pico-molar concentrations. This has culminated in a plasmonic nanoparticle template and a single nanoparticle, being able to detect a single molecule of a given Raman active analyte [39–41].

While SERS is perhaps the most widely recognised plasmonic sensing methodologies, it is most certainly not the only technique to utilise the power of plasmonic effects to great advantage. Perhaps one of the simplest plasmonic sensing techniques is *colourmetric sensing.* This technique uses the sensitivity of a plasmonic structure to changes in its local environment, which causes a specific change to their optical response. This sensitivity can be exploited by a nanoparticle array on a substrate; a single isolated nanoparticle; a colloidal suspension of nanoparticles; or a metallic film. This optical response change can be attributed directly to the presence of a given material, molecule or compound [42, 43]. This is the exact methodology used within LSPR spectroscopy [44–46]. LSPR spectroscopy, where the spectral position of the characteristic plasmonic peak of a plasmonic nanoparticle template or single nanoparticle, changes when a material or compound is captured by a functionalisation layer on the structures surface. This technique is used heavily within the field of filtration, to monitor the growth of thin films and monitoring drug delivery and surface binding. While the LSPR effect is more widely used for sensing, it would be unfair to ignore the power of SPP sensing techniques [47], used extensively within biochemistry to monitor surface binding, such as drug delivery and DNA binding events. Additionally, SPP sensing has been shown to monitor the success and rate of solution-based reactions and binding events by assessing changes to the refractive index of a buffer solution [48–50]. Where the change in refractive index can be quantified by the change of the initiation angle, wavelength or energy of the surface plasmon polariton.

2.4 Nanostructuring

Modern technology has developed too such an extent that the capabilities of devices double every 12 - 18 months [51]. This has led to a global incentive to be able to equip devices with more applications, which in turn has led to a need to be able to fabricate components at smaller and smaller scales. This is clear when considering the development of the range of routes towards nanofabrication, allowing for new techniques and methods for precisely and reproducibly fabricating these necessary structures. This technology has become the backbone of plasmonics, being used by research groups worldwide to produce highly ordered nanostructures, as at a fundamental level, the localised surface plasmon resonance effect involves the interaction of light with a nanostructure. Thus far, we have presented the phenomenon, but little attention has been paid to the nanostructure itself.

The shrinking of structures has been driving research since the late 1970's, where groups were able to produce a sub-micron feature size [52] and by the 1980's groups such as *H. Ahmed L. Lee* could be seen to produce features of between 100 - 1000 angstroms (A) [53, 54] using the techniques of nanolithography [55–58], in a traditional *top-down* methodology. Top-down techniques use physical process where material is removed from the bulk to produce the desired features. A prime example of a top-down technique utilised for nanofabrication is lithography. The wide range of lithographical techniques exemplify the disadvantages of top-down processes, namely being extremely expensive in terms of both time and essential equipment and limited potential processing area. Nanolithography has been shown to be able to produce nanoscale features by using an electron and ion beams to restructure a material as well as using photons to selectively cure areas of a resits material. Simultaneously however, nanoscale lithography offers incredible levels of control and specificity [59].

Despite the extensive number of publications and demonstrations of traditional lithographic techniques being used to produce nanoscale features, there are several other possible routes towards this goal. One of the more widely realised methodologies for this, is an inverse approach decried as a *bottom-up* technique. Such techniques use an existing nanoscale (or microscale) material as a building block to create a desired structure. These building blocks are driven by local chemical and physical forces to self-assemble into a specific structure. A primary example of this type of nanofabrication is referred to as natural or colloidal lithography [60–62], where the building blocks are initially stored in a colloidal solution that can be spun, drop cast or evaporated onto a given substrate. Natural lithography has been highlighted by groups such as *B. Tang, et al.* and *V. Ng et al.*, who have demonstrated the ability to produce features in the order of the size of the initial nanoscale building blocks [63, 64]. This type of approach has a number of advantages over more traditional lithographic techniques, as it can be used to pattern large areas [65,66]; is a very fast process; can be used on substrates which are highly chemically and thermally sensitive; in addition to its most desirable advantage that it does not require the use of complicated and specialist equipment [67,68]. Despite the number of advantages, natural lithography and other bottom-up processes do not offer the levels of control, specificity, or more vitally reproducibility offered from a more traditional top-down technique.

2.5 Photonic Processing

While these two schools of thought, *top-down* and *bottom-up* processes, are most often compared and contrasted [69, 70] and even combined [71, 72], there does exists a third option for nanofabrication, namely photonic processing [2] where light is utilised to modify an existing surface or structure. Light has been used for high quality micro- and nanostructuring most notably *via* photolithography [73]. Photolithography has been shown to function across a wide range of variations, from single-photon [74] and multi-photon [75] methods to interference-based techniques [76]. However, all these photolithographical approaches are based on traditional lithographic techniques and can be considered as a layer-by-layer production method as opposed to a direct fabrication technique offered by other forms of photonic processing.

As shown in figure 2.2, lasers have become an increasingly common tool in a wide variety of processing methods due to their phenomenal versatility in terms of wavelength, pulse width and length, power delivered and spot size which has led to such a diverse range of laser processing techniques.

With the development of higher power and shorter pulse length lasers, more direct laser processing techniques have been developed, many of which can and have been utilised for nanofabrication. Photonic processing has been developed from the existing and well understood processes such as laser machining and thermal annealing. Laser machining processes such as ablation, milling, drilling, cutting and welding [77–79] have been re-purposed at the micro- and nanoscale, by exploiting the same mechanisms as their macroscopic counterparts [80, 81].

One of the most widely used laser processing techniques is laser ablation [82, 83]. Laser ablation describes the removal of material due to the localised super heating of a material caused by the specific absorption of the laser wavelength in the processed material. Laser ablation has been used extensively within macro- and microscopic laser drilling and patterning of hard materials such as steel [84] and ceramics [85,86]. In addition to being able to modify traditionally tough materials, laser ablation has been shown to function equally well for softer, more thermally sensitive materials such as polymers [87] and biological materials [88, 89]. Another widespread

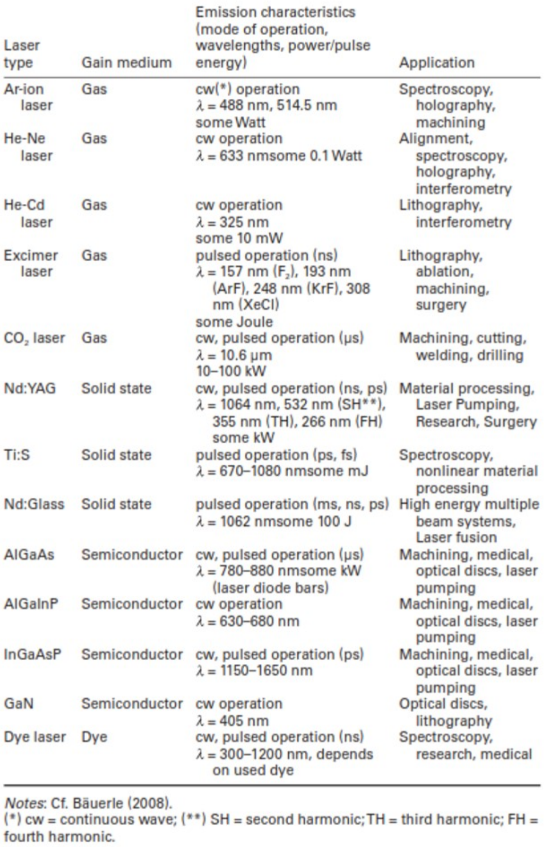

Laser type	Gain medium	Emission characteristics (mode of operation, wavelengths, power/pulse energy)	Application
Ar-ion laser	Gas	cw(*) operation λ = 488 nm, 514.5 nm some Watt	Spectroscopy, holography, machining
He-Ne laser	Gas	cw operation λ = 633 nmsome 0.1 Watt	Alignment, spectroscopy, holography, interferometry
He-Cd laser	Gas	cw operation λ = 325 nm some 10 mW	Lithography, interferometry
Excimer laser	Gas	pulsed operation (ns) λ = 157 nm (F_2), 193 nm (ArF), 248 nm (KrF), 308 nm (XeCl) some Joule	Lithography, ablation, machining, surgery
CO_2 laser	Gas	cw, pulsed operation (μs) λ = 10.6 μm 10–100 kW	Machining, cutting, welding, drilling
Nd:YAG	Solid state	cw, pulsed operation (ns, ps) λ = 1064 nm, 532 nm (SH**), 355 nm (TH), 266 nm (FH) some kW	Material processing, Laser Pumping, Research, Surgery
Ti:S	Solid state	pulsed operation (ps, fs) λ = 670–1080 nmsome mJ	Spectroscopy, nonlinear material processing
Nd:Glass	Solid state	pulsed operation (ms, ns, ps) λ = 1062 nmsome 100 J	High energy multiple beam systems, Laser fusion
AlGaAs	Semiconductor	cw, pulsed operation (μs) λ = 780–880 nmsome kW (laser diode bars)	Machining, medical, optical discs, laser pumping
AlGaInP	Semiconductor	cw operation λ = 630–680 nm	Machining, medical, optical discs, laser pumping
InGaAsP	Semiconductor	cw, pulsed operation (ps) λ = 1150–1650 nm	Machining, medical, optical discs, laser pumping
GaN	Semiconductor	cw operation λ = 405 nm	Optical discs, lithography
Dye laser	Dye	cw, pulsed operation (ns) λ = 300–1200 nm, depends on used dye	Spectroscopy, research, medical

Notes: Cf. Bäuerle (2008).
(*) cw = continuous wave; (**) SH = second harmonic; TH = third harmonic; FH = fourth harmonic.

types.jpg

Figure 2.2: Table showing a range of different types of lasers, their emission characteristics and the application / technique most commonly associated with the given laser type. Table taken from reference [2], chapter 6, table 6.1, page 169.

and commonly experienced application of laser ablation is within the field of thin film fabrication, where laser ablation is used as part of pulsed laser deposition [90–92]. This phenomenon has been shown to be able to produce features ranging from 10's of nm to 1micron, across large areas. The phenomenon used for pulsed laser deposition is identical to that used when patterning a sample at a micro- and nanoscale. Beyond a direct fabrication technique for producing a specific surface structure, laser ablation has been shown by a wide number of groups to be able to produce nanoparticles from a bulk target. Laser ablation of a bulk material has been shown to produce nanoparticles in a gaseous environment [93, 94] and allows for the direct deposition of metallic nanoparticles onto a specific substrate. Beyond this, nanoparticles can be directly fabricated as a colloidal solution *via* laser ablation [95, 96], were the produced nanoparticles can be produced as a pure nanoparticle or in a core-shell morphology dependent on the solution used. The production of these nanoparticles in solution are produced *via* the same phenomenon as pulsed laser deposition and in fact often makes use of identical experimental equipment.

In addition to using laser processing to fabricate a nanostructure. Laser annealing [97] is a highly similar yet distinctly different technique exists that allows for the modification of an existing nanostructure like a colloidal suspension of nanoparticles [98–100] and within the field of semiconductor research to modify thin film properties [2, 97, 101–106]. Laser annealing is based on the concept of rapid thermal annealing [107, 108] which has been shown extensively within the semiconductor research to alter dopant densities; the nature of the film interfaces; and change the crystal structures of the films being processed. Laser annealing makes use of material specific absorption of the laser wavelength to allow for localised heating. Through the selection of the processing wavelength to correspond to the specific absorption maxima for the given material gives rise to a local temperature rise of for an ultra-short period of time can be achieved with minimal heating to surrounding layers and therefore minimising stress to the sample entire [97, 109]. Laser annealing has been shown to be able to recreate all the notable effects of rapid thermal annealing, with the specific advantage of being able to specifically treat only the desired areas. Laser annealing has the additional advantage that because of the ability to treat only specific areas of the sample, laser annealing can be used to produce a specific pattern on a single sample [110–112].

Chapter 3

Experimental Methods

3.1 Introduction

This chapter will focus on the range of experimental techniques used for fabrication and characterisation throughout this research. Here we will focus on the underlying mechanisms, the rational for their use and an exploration of the systems used for these techniques. Additionally, we will present the key features of the specific equipment used and finally discuss the specific parameters necessary for the equipment used.

3.2 Thin Film Fabrication

3.2.1 Radio Frequency Magnetron Sputtering, RFMS

Sputtering, classified as a physical vapour deposition (PVD) technique, is widely used to produce thin films, both within industry and research due to its compatibility with large area and volume requirements, the diverse range of materials available for sputtering and its low cost [113]. All sputtering techniques are conducted in an evacuated environment, in the presence of a specific sputtering gas, under the influence of an electric field. The sputtering process occurs when gas ions bombard the surface of a bulk solid target material, liberating atoms that are subsequently deposited on a substrate. Testament to the utility of sputtering is the range of sputtering variations, including but not limited to: reactive sputtering (the production of an oxide or nitride material by inducing a chemical reaction between the sputtered species and the sputtering gas) and co-sputtering (a single deposition process where multiple sputtering targets are actively used).

Argon (Ar), is widely used as a sputtering gas because of its low reactivity with the sputtered species in addition to its relatively high molecular mass, ensuring the ease of liberating atoms for the target surface. The Ar gas is ionised through collisions with electrons (e^-) accelerated by the electric field between the anode (substrate holder / chamber walls) and cathode (target). These Ar ions are then in turn accelerated towards the target surface, bombarding the target. The sputtered species then travel to the substrate, gradually depositing through several intermediate stages of island growth, interconnected islands and eventually forming a continuous thin film [114, 115].

The Ar ions incident onto the target surface undergo 1 of 4 possible interactions:

1. Liberating (sputtering) energetic neutral species from the target, when the energy imparted from the Ar ions is greater than the binding energy of the target atoms.
2. Ar ions are reflected as high energy neutral Ar. Induces a positive charge at the target surface.
3. Secondary electron emission from the target surface. Induces a positive charge at the target surface.
4. Ar ions impregnate the target material.

The categorisation of a sputtering system is generally defined by the nature of the applied electric field, generally either a direct current (DC) or radio frequency (RF) power supply [113, 116]. This research was preformed using a radio frequency (RF) power supply, operating at 13.56 MHz. RF sputtering offers the advantage of being able to more reliably sputter insulating materials when compared to DC sputtering, as the oscillating field polarity causes the target to cycle between ion and electron bombardment, allowing the electrons to neutralise any positive charge build up at the target surface. A diagrammatic view of a RF sputtering system can be seen in figure 3.1. Due to this, RF sputtering could be used as a single thin film fabrication methodology to produce all the thin films required for this work.

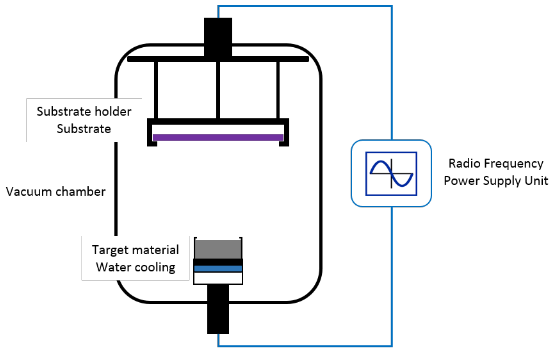

Target:	+	-	+	-	+
Substrate:	-	+	-	+	-

Figure 3.1: Diagram of a radio frequency sputtering system.

Another sputtering variant is magnetron sputtering (MS), achieved by the addition of a set of permanent magnets below the target material, superimposing a magnetic field over the electric field from the power supply - both DC and RF sputtering can be used in conjunction with such a magnet arrangement. The magnetic field acts to increase the plasma density close to the target by trapping the primary and secondary electrons, which decreases the temperature rise at the substrate, while offering no impedance to the action of the Ar ions. Due to the increased plasma density, the number of Ar ionisation events are increased, leading to a higher deposition rate even at lower deposition pressures due to an increase in plasma stability [113, 115, 116]. RFMS has the advantage of high levels of efficiency and significantly greater film uniformity and step coverage than techniques such as thermal evaporation, balanced by a slower rate of deposition an increased thermal load to the target.

This research makes use of non-reactive radio frequency magnetron sputtering (RFMS), to take advantage of both the individual advantages of RF and magnetron sputtering. Additionally, this allowed for the beneficial film formation stages during growth necessary for this work, as this research requires the formation of both thin (nominally 10 nm) discontinuous metal films and thick (50 nm and above) continuous dielectric films. RFMS offers a single, low cost, low temperature methodology to produce both film structures with excellent quality and high reproducibility in house. Specifically, in this research two pre-existing custom built, multi-target vacuum vessels were used, namely Chamber 2 (maximum of 3 target materials) and Chamber 1 (maximum of 4 target materials). Each RFMS system was pumped to high vacuum ($x10^{-}6$ mbar) through a combination of a primary diffusion pump and a backing rotary vane pump. In both these systems, a range of RF powers were used, depending on the target material, ranging from 40W (silver) - 120W (silicon dioxide). Additionally, the operating, or sputtering, pressure was optimised for each system to ensure the highest possible film quality at 5 mTorr for Chamber 2 (used for silver, silicon dioxide and yttrium oxide) and 3 mTorr for Chamber 3 (used for AZO and ZnO). Prior to each experimental series, each sputtering system was loaded with the necessary targets for this work.

3.2.2 Evaporation Deposition

Evaporation deposition is another method for the formation of thin films. The process can be clearly visualised if you consider a pot of boiling water, as shown in figure 3.2.

As with sputtering, evaporation deposition is conducted in an evacuated environment, within a vacuum chamber, to increase the mean free path of the evaporated species, to prevent a chemical reaction and to minimise cooling during travel. There are a number of advantages to thermal evaporation such as a higher deposition rate than that of sputtering and high film purities. This allows for the deposited thin film to make the transition to a high quality continuous film

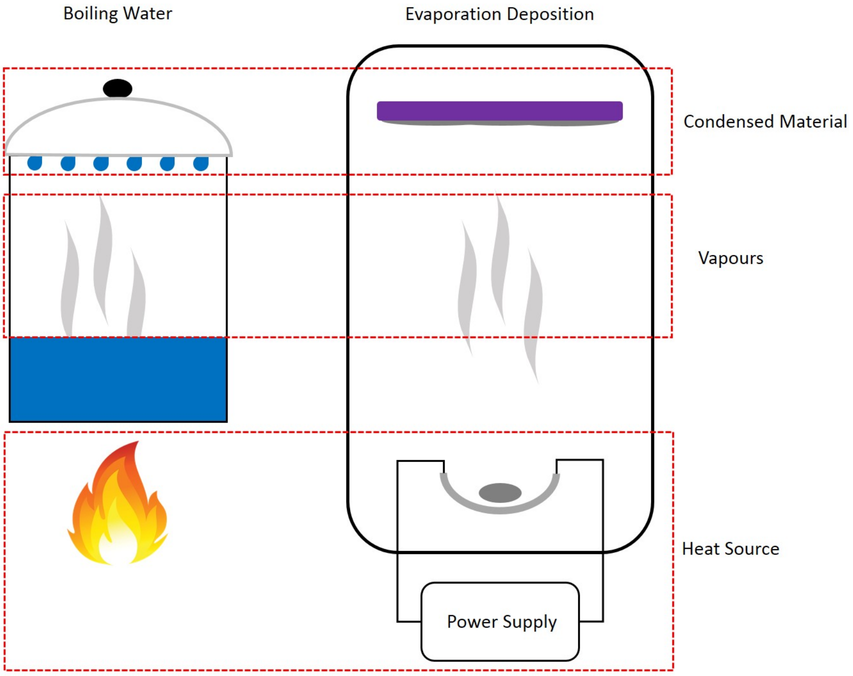

Figure 3.2: Schematic comparison between boiling water and evaporation deposition.

at smaller nominal thicknesses. However, evaporation requires the operator to more seriously consider the effect of shadowing [115,117]. Shadowing, also called *step coverage*, is a phenomenon that occurs during deposition on a rough or structured substrate, such as an integrated circuit of a multilayer sample [118]. As during an evaporation process the source material and the substrate remain in fixed positions, the evaporated species arrive at the substrate form a single direction, resulting in a high contribution of line of sight deposition, any areas of high roughness or containing protruding features can block the deposition onto surrounding areas, severely affecting the uniformity of the produced thin film.

3.2.3 Thermal Oxidation of Silica

Thermal oxidation describes a process where an oxidising agent diffuses into a surface and reacts, under high temperature, to produce a uniform oxide film. This technique is widely used both within research and industry for increasing the thickness of the silica (SiO_2) layer on a silicon wafer.

The oxide growth is described by the *Deal-Grove* model [119,120] can also be used to calculate the time necessary for the growth of a specific thickness at a given temperature. This model predicts that the oxidising reaction only occurs at the oxide / substrate interface, which leads to the oxidising agent needing to initially diffuse from the bulk gas to the samples surface, then diffuse through any existing oxide layer, before finally reacting with the substrate. It is important to note that in the case of silicon, there will always be an intrinsic, naturally occurring silica layer, with a nominal thickness of 2 nm, which is created at atmospheric conditions. The formation of this native oxide layer is also described by this model.

Thermal oxidisation can occur in either a *wet* or *dry* environment which will influence the growth rate of the oxide layer. In a wet environment, the oxidising agent is water vapour, usually as steam due to the high temperature, while in a dry environment molecular oxygen acts as the oxidiser. While dry oxidisation allows for a slower growth rate, the oxide produced has a higher density and dielectric strength when compared to wet oxidisation, in addition to the high quality and cleaner substrate / oxide interface achievable [120,121]. A comparison the necessary growth time for a range of oxide thicknesses can be seen in figure 3.3.

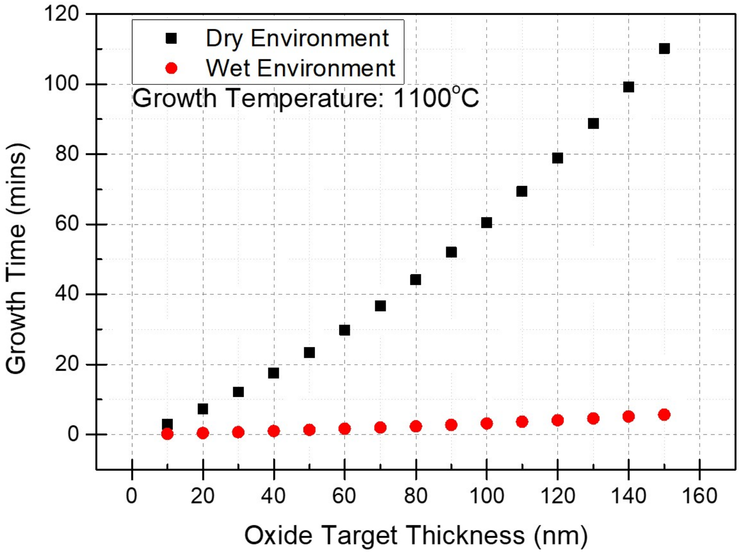

Figure 3.3: Thermal oxide growth times, calculated with the Deal-Grove model, at a growth temperature of $1100^{O}C$ in two distinct environments, a wet environment (red circles) and a dry environment (black squares).

This research uses dry oxidisation to produce silica films on a silicon substrate. The slower growth rate and inherent long growth time for thick films, does not diminish the quality of the silica layer produced. An electric high temperature oven (able to achieve a maximum temperature of 1200 °C) was used to heat the silicon substrates to the desired temperature and maintain this temperature until enough time had passed to allow for the growth of specific oxides thicknesses.

3.3 Thin Film Thickness Characterisation

It is a necessity within thin film technology to be able to assess the thickness of these films. Thin film thickness can be measured in a variety of ways, from full contact physical techniques, such as with a stylus, to non-contact post-fabrication techniques, such as *via* thin film interference. The method chosen is heavily dependent on the thin film material under investigation and the assumed or targeted thickness. In this research, two methods for investigating the thin film thickness have been used, at two distinct stages of sample preparation. The first method is to monitor the film thickness *in situ* as it grows during RF magnetron sputtering, while the second method makes use of thin film interference to calculate the thickness of a fabricated film.

3.3.1 Quartz Crystal Microbalance

A quartz crystal microbalance or QCM, when used within thin film technologies, enables *in situ* monitoring of thin film fabrication, monitoring both the growth rate and film thickness for a wide range of fabrication techniques and is often referred to as quartz crystal monitors [122]. A QCM can in some cases be used for more than monitoring, as they can be used to control the process, allowing for real time adjustment to achieve a desired growth rate or can terminate the growth process when the desired thickness is achieved, and are therefore often described as a quartz crystal controller or QCC.

A QCM calculates the growth rate and thickness of a thin film by assessing the frequency change of a quartz resonator due to the mass change at the surface. As a quartz crystal is a well-known piezoelectric material, an AC voltage applied across the crystal can be used to produce a highly stable resonance allowing for the precise identification of the resonant frequency. During a deposition process, material will accumulate on the surface of the quartz crystal, increasing the effective thickness of the quartz. As the resonant thickness of a quartz crystal is, in part, dependent on the thickness of the crystal, the deposited mass can be considered as the quartz crystal increasing in thickness [123], where the additional mass can be calculated according to the Sauerbrey relationship [**?**, 124, 125]:

$$\Delta f = \frac{2f_0^2}{A\sqrt{\rho_q \mu_q}}\Delta m \tag{3.1}$$

Where: Δf is the change in frequency; f_0 is the resonant frequency of the quartz crystal; Δm is the mass change due to the deposited material; A is the crystal area; ρ_q is the density of quartz; and μ_q is the shear modulus of quartz. With the change of mass, Δm, calculated from the Sauerbrey equation, and the know density of the deposited material, the thickness can be calculated using the density relationship:

$$t = \frac{\Delta m}{A} \times \frac{1}{\rho} \tag{3.2}$$

Where: t is the thickness of the material deposited onto the quartz crystal, ρ is the density of the deposited material and A is the exposed area of the quartz crystal.

While this technique allows for the calculation of the deposition thickness on the quartz crystal, this is of little of interest, as the goal is to be able to identify the thickness of material deposited onto the substrate. Consequently, a correlation between the know thickness (the thickness deposited onto the quartz crystal) and the desired thickness (the thickness deposited onto the substrate) must be found. It can be easily visualised, that if the crystal and the substrate are equidistant and were orientated identically to the source, or target material, then these two thicknesses would be the same. However, it is often the case that due to the directional nature of many thin film fabrication techniques, to achieve this, would result in a significant shadowing effect on either the substrate of QCM. As such, it is common that the QCM and substrate are positioned differently to ensure that the QCM does not impede the thin film fabrication on the substrate. Which introduces an inherent discrepancy in the thickness and rate measured at the QCM to that experienced at the substrate. Therefore a *tooling factor* (TF) is introduced to adjust the values calculated, where when the QCM is located below the substrate / closer to the source the tooling factor will be below 100%, while when the QCM is above / further from the source the tooling factor will be above 100%, as shown in figure 3.4. The tooling factor can be calculated as the ratio of the independently measured deposition thickness (d) to the QCM measured deposition thickness (t), scaled by the assumed tooling factor used for said deposition [118, 122, 123].

$$TF_{true} = \frac{d}{t} \times TF_{assumed} \tag{3.3}$$

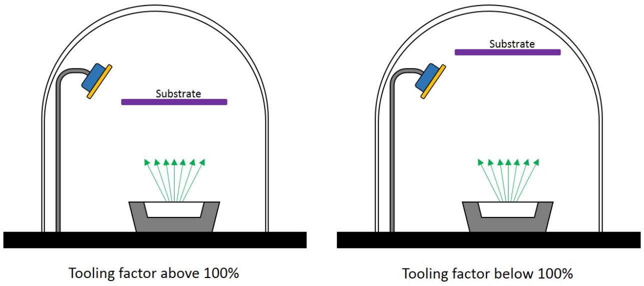

Figure 3.4: Diagram showing how the value of the tooling factor will change depending on the relative positions of the substrate and the quartz crystal microbalance.

In this research, a quartz crystal microbalance was used to monitor the real time thickness and growth rate of thin films, during both thermal evaporation and RF magnetron sputtering with tooling factors individually calculated for each material ranging from 120% for silicon dioxide to 349% for silver. This enabled the production of consistent thin films with the desired nominal thin film thickness necessary for the work.

3.3.2 Thin Film Interference - Filmetrics

Thin film interference is an optical, non-destructive method for assessing the thickness, refractive index and roughness. This phenomenon is well understood and has been observed in nature and scientifically studied extensively, where this effect arises from light matter interactions as the interference of light reflected from the upper and lower interface of a thin film, as shown in figure 3.5, influence the overall reflectance of the sample. As with other forms of interference, thin film interference can be either constructive, when $t = m\frac{1}{2n}\lambda$, resulting in an increase of reflectance, or destructive, when $t = (m + \frac{1}{2})\frac{1}{2n}\lambda$, resulting in a decrease of reflectance, where: t is the thin film thickness; n is the refractive index of the thin film material; λ is the wavelength of light; and m is an integer value. Where we assume that the light is incident onto the thin film material form air.

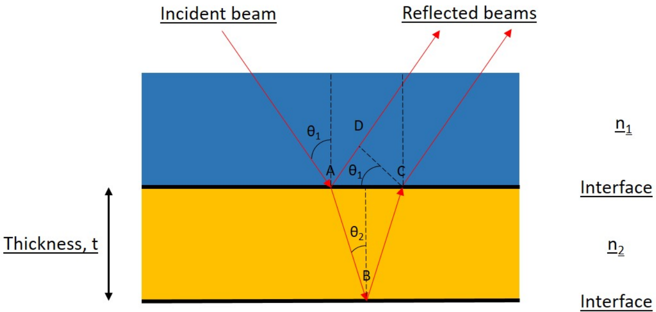

Figure 3.5: Diagram of thin film interference, where the interference occurs between the light reflected from the upper and lower interface of the thin film material. The incident beam is shown at an angle, however experimentally this is performed very near the normal incidence.

At each interface, a certain percentage of the incident light will be reflected, and another percentage will be transmitted, as described by the Fresnel equations. The light reflected at the two interfaces, as shown in figure 3.5, will interfere, where the nature of this interference will depend on the phase difference of the two light beams. The phase difference can manifest as either constructive or destructive interference. These two conditions can be identified by calculating the difference in optical path difference (OPD) [4, 126].

$$OPD = n_2(AB + BC) - n_1(AD) \tag{3.4}$$

Where, we can see from figure 3.5, that: $AB = BC = \frac{t}{cos(\theta_2)}$ and $AD = 2.t.tan(\theta_2).sin(\theta_1)$. Then, by using *Snell's Law* ($n_1 sin(\theta_1) = n_2 sin(\theta_2)$) we can rearrange equation 3.4.

$$OPD = n_2(\frac{2t}{cos(\theta_2)}) - 2.t.tan(\theta_2).n_2.sin(\theta_2) \tag{3.5}$$

$$OPD = 2n_2t\frac{1 - sin^2(\theta_2)}{cos(\theta_2)} \tag{3.6}$$

$$OPD = 2n_2tcos(\theta_2) \tag{3.7}$$

Where, if the OPD is equal to an integer number of wavelength ($OPD = m\lambda$), there will be constructive interference. Allowing for any material specific phase changes at reflection.

If the above measurement of a uniform thin film is conducted instead with a white light source, the broadband reflectance of the film will show inherent wavelength specific high and low reflectance, due to the wavelength dependence of the interference condition. This effect can clearly be seen from different thicknesses of silicon dioxide or titanium nitrate, which produce highly specific colours at certain thicknesses in addition to the coloration of different insects and birds [127]. Simultaneously, this broadband measurement can be used to calculate n and k for the material across the wavelength range used. Additionally, by monitoring the periodicity and amplitude of the reflectance versus wavelength, it is possible to quantify the surface or interface roughness.

This research uses the normal incidence broadband reflectance of thin films, fabricated *via* RF magnetron sputtering and thermal oxidation of silicon, to assess the quality of the material by comparing the calculated refractive index to those available within the literature, while simultaneously allowing for an independent measurement of the thin film thickness.

3.4 Laser Annealing

Nanofabrication and nanostructuring have become key aspects in modern research and technologies, where there are two distinct approaches that can be taken to achieve the necessary surface morphology, namely, top-down and bottom-up strategies. Top-down processes, such as traditional forms of lithography, allow for unparalleled levels of control and reliability, however there are significant restrictions to the maximum processing area and the processes is expensive in terms of time and necessary equipment. Conversely, bottom-up processes, which make use of chemical driven self-assembly processes, can be used to rapidly produce significantly larger areas with low cost and readily available equipment, with a notable loss to the reproducibility and control over the final structure. Photonic processing, processes making use of light in place or more traditional energy sources such as heat, acts as an intermediate between top-down and bottom-up techniques, by allowing for large area rapid processing with exceptional levels of control and reliability [2, 128]. Photonic processing has been used for remarkable benefits for both fabrication and post-processing, allowing for previously unattainable devices and structures to be achieved easily, where such processes are generally performed with high power lasers, both pulsed and continuous wave systems [2].

Laser annealing (LA) is a photonic technique that allows for the selective processing of the key element within the sample, based on the absorption of the processing wavelength by a specific material within the sample. This research focuses on the laser annealing of thin, discontinuous metal films on various substrates, to produce and modify plasmonic nanoparticle templates (PNT), with a custom laser delivery system, as shown in figure 3.6.

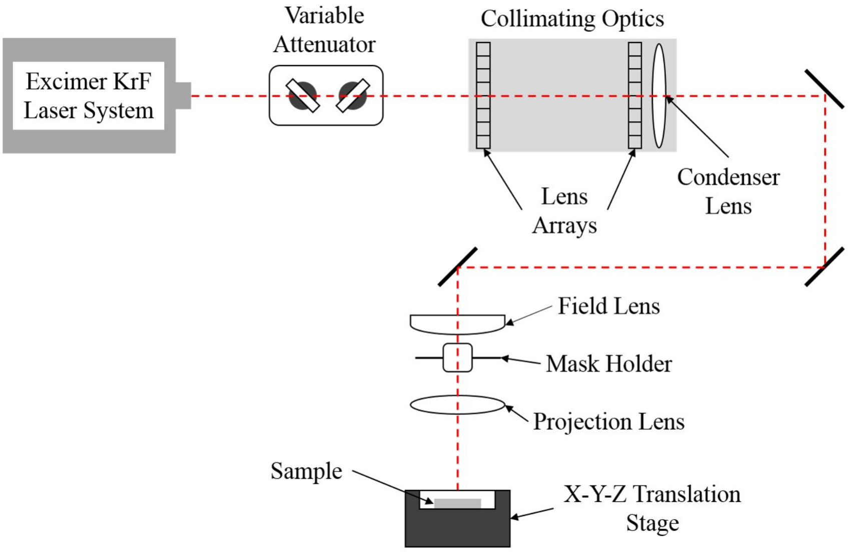

Figure 3.6: Schematic diagram of the custom laser delivery system used for laser annealing in this research.

It is more accurately to consider laser annealing as two distinct processes, differentiated by the number of laser pulses used. With one laser pulse, the as deposited metal film is transformed into a nanoparticle template through laser induced self-assembly, or LISA [128,129]. The LISA process is a rapid thermal process, where the high absorption of the processing wavelength in an active, discontinuous layer, most commonly a metallic thin film, induces a dramatic local temperature rise of up to 5000 °K, where the temperature rise is proportional to the heat conduction of the thin film material. When the temperature rise is above the melting temperature of the thin film material, the material undergoes a phase transition and melts. The molten metal poorly wets the substrate, where the poor wetting of the substrate increases the likelihood of the liquid phase breaking up. Subsequently the molten metal experiences a heightened rate of cooling at the edges, and the molten metal breaks into nano-scale droplets due to the Rayleigh instability and cools back to the solid state producing a PNT [130–132]. The time necessary for the metallic film to achieve room temperature, or cooling time, is comparable to the pulse length of the processing laser (25 ns). Such nanoparticle templates are often bimodal in nature, where there are two distinct families of nanoparticle sizes, one larger and one smaller, giving rise to a characteristic double peaked optical response. At higher laser fluences (energy densities), the size difference of the two nanoparticle families is reduced.

When using a multi-pulses sequence, the first pulse acts to produce the nanoparticle template, as described above (LISA), while the following pulses change the surface morphology, or induce a modification of the nanoparticle arrays (MONA) [128]. This process is driven by the selective heating of the larger nanoparticles, which melt and reform into smaller nanoparticles, where there is a mass transfer to the pre-existing smaller nanoparticles, in the opposite action to that described by Ostwald ripening, allowing for multiple laser pulses to form a more homogeneous nanoparticle template. This allows of a minimised size distribution.

This research produces arrays of LA areas, with a MONA-LISA process, at two laser wavelengths of $248nm$ and $193nm$ in 25 ns laser pulses at a repetition rate of 1 Hz, with the collimating optics and the condenser lens producing a 2-dimensional top-hat beam profile. Throughout this work, the primary parameters under investigation are the laser fluence ($350mJcm^{-2} - 900mJcm^{-2}$ in a 2.45 mm x 2.45 mm square spot) and number of pulses (1 - 15 pulses) to produce a series of nanoparticle arrays for individual assessment and characterisation.

3.5 Plasma Etching

Plasma etching, or plasma patterning, is a form of post-fabrication surface modification, commonly used within the semiconductor industry to produce very precise patterns and structures for electrical devices and components.

Plasma etching operates by bombarding the sample surface with ions and high energy neutrals from a plasma, where an appropriate plasma species must be selected to ensure a suitable etching rate. Additional concern must be paid to ensure that any chemical reaction that may occur between the plasma and the etched material will not result in the formation of a dangerous compound. In the case where plasma etching is used to alter the structure of a metallic surface, the formation of a volatile compound during the process can act to increase the etch rate and improve the resolution of the patterning. The etching process is equivalent to sputtering, which inherently leads to the impregnation of the surface with the plasma species. This results in a two-fold surface modification, the first coming from the alteration of the surface topography, while the second stems from the influence of the implanted plasma species [133, 134].

This research makes use of an oxygen in argon plasma (10% O_2 in Ar) to etch and modify the surfaces, enabling the direct modification of the interface between subsequent thin film layers for a sample.

3.6 Finite-Difference Time Domain Method

Finite-difference time-domain method (FDTD), is a widely popular mathematical modelling technique used to solve Maxwell's equations, allowing for theoretical solutions to electromagnetic problems. The basis for FDTD is to discretise, in both time and space Maxwell's equations using central difference approximations. This methodology can be used in one, two- or three-dimensional calculations with relative ease [128, 129, 135].

FDTD method can be described as a "*leap-frog*" technique. This stems from the calculation process, where first the electric component is solved at time t, then the magnetic components are solved at time $t+$ and repeated until the required [136,137]. Where a diagrammatic representation of this can be seen in figure 3.7.

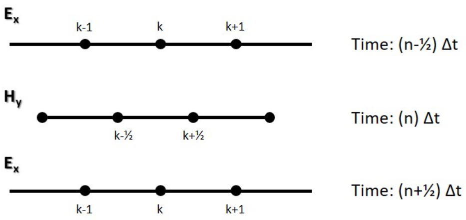

Figure 3.7: Diagram of the Yee one dimensional scheme for updating electromagnetic fields in both space and time.

A FDTD computational cell must be set up with a specific boundary condition at each face of the cell. There are a few boundary conditions that can be used in the x, y and z axes that will influence the nature of the calculated solution. For this research, the computational cells have been built with *Bloch periodic boundaries* on the x and y axis and *perfectly matched layer (PML)* boundary in the z axis. The periodic boundary conditions allow for the construction of a simpler computational cell containing, perhaps a single nanoparticle, which will be periodically duplicated in neighbouring cells, thus creating an ideal nanoparticle template. The PML boundary is included to absorb all the light incident to it, which prevents any reflections form the cell edge. A PML is comprised of multiple layers (commonly multiples of 4), where each layer has a gradually increasing refractive index and a minimal interface, preventing any incident fields escaping once they enter the PML boundary. This allows for the simulations to calculate the response of the structure contained within the computational cell. An example computational cell can be seen in figure 3.8.

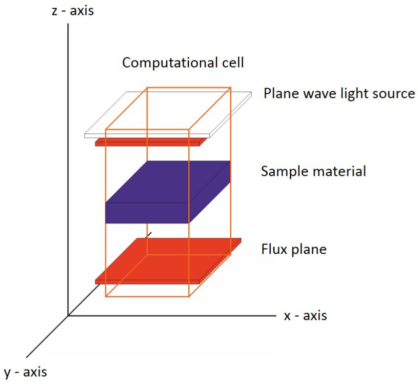

Figure 3.8: Schematic view of a 3D computational cell complete akin to those used in the research. The cell contains a plane wave light source (white) two flux planes (red) and a single layer sample under investigation (blue).

This research makes use of FDTD in two ways, firstly to calculate the optical reflectance, transmission and absorption spectra of a nanoparticle template and secondly to simulate the temperature rise and cooling rate of specific layers within the sample structure.

3.7 Optical Characterisation

The samples produced for this research were fabricated to have specific optical properties. It is therefore inherently vital that the optical properties of these samples are quantified. Optical assessment is one of the most diverse types of characterisation available thanks to the depth of knowledge that exists relating to the field of optics and photon - matter interactions. This research uses optical characterisation to both assess the as fabricated samples, both the as grown and the nanoparticle templates, as well as to probe the viability of the samples to act as sensing surfaces or components within a sensing device.

3.7.1 Optical Reflectance Spectroscopy, ORS

One of the simplest, most effective and widely used ways to identify and characterise a plasmonic nanoparticle template is to assess their optical response. While this can be accomplished *via* either reflectance, transmission or adsorption spectroscopy, this research makes use of predominantly reflectance spectroscopy in a variety of ways.

The optical reflectance of a material, R, is defined as the ratio of the intensity of light reflected from the material, I_m, to the intensity of light incident onto the material, I_0:

$$R = \frac{I_m}{I_0} \tag{3.8}$$

This enables the calculation of the reflectance spectrum of any given material or surface. However, the intensity of the light incident on the material is inherently a combination of both the light source, which is not necessarily known, and the ambient light condition, which is a value that is susceptible to large temporal fluctuations. As a result, it is preferable to modify equation 3.8 to remove I_0, which will allow us to account for any variation or unknowns in the lighting conditions. This process can be demonstrated if we consider the case where we wish to calculate the reflectance of a thin film as shown in figure 3.9.

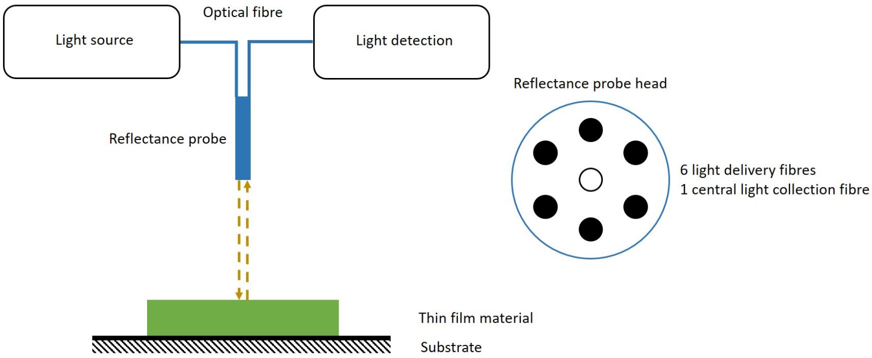

Figure 3.9: Schematic of the experimental set up used to measure the reflectance of a sample.

Using the definition of reflectance, we can see that the reflectance of the thin film:

$$R_{TF} = \frac{I_{TF}}{I_0} \tag{3.9}$$

At this point we must also consider the reflectance of a known material, or '*reference mirror*':

$$R_{ref} = \frac{I_{ref}}{I_0} \tag{3.10}$$

With these two simultaneous equations, we can remove the need for the I_0 term in the final reflectance equation, by initially rearranging equation 3.10, to produce an equation for I_0,

$$I_0 = \frac{I_{ref}}{R_{ref}} \tag{3.11}$$

This equation for I_0 (3.11) can now be substituted into the equation for the reflectance of the thin film, equation 3.9:

$$R_{TF} = \frac{I_{TF}}{I_{ref}} \times R_{ref} \tag{3.12}$$

The final stage is to correct for the dark current of the detector used:

$$AR = \frac{I_{TF} - I_{Dark}}{I_{ref} - I_{Dark}} \times R_{ref} \tag{3.13}$$

While this equation only accounts for the reflectance of a single wavelength, we can calculate the broadband reflectance by using a spectrometer to measure the broadband reflected intensities of a thin film and repeating this calculation for all wavelengths. This allows us to calculate the reflectance, or *absolute* reflectance (AR), of any material by measuring the reflected intensities of the sample, a reference mirror, which has a known reflectance, and the dark spectrum. During this research, a range of reference mirrors were used: aluminium (Al), silver (Ag), gold (Au) and silicon (Si), where the mirror used would depend on the sample structure (as it is preferable to use a material not found in the sample), and the spectral range under investigation.

In addition to the calculation and assessment of the absolute reflectance, this research will also present the calculated *Reflectance Relative to the Effective Substrate* or RRES. Here, the reflected intensities of the sample are normalised to the reflected intensities of the effective substrate, rather than to a reference mirror. The RRES spectra show a minimised response from the underlying structure, when compared to the calculated absolute reflectance for the same nanoparticle template. This allows the response of the nanoparticle template to be more easily identified.

$$RRES = \frac{I_{Sample} - I_{Dark}}{I_{EffSub} - I_{Dark}} \tag{3.14}$$

The effective substrate is defined as the complete structure that exists below the layer that is laser processed. For example, if we consider a sample consisting of a silicon wafer substrate, a 100 nm of thermally grown silica interlayer and a 10 nm thin silver film that will be laser annealed: $Si/SiO_2(100nm)/Ag(10nm)$, here we would define the effective substrate as the silicon wafer and silica interlayer: $Si/SiO_2(100nm)$.

Through the calculation of the AR and / or RRES, the optical response of a given plasmonic nanoparticle template can be seen. As the focus of this work is to assess the functionality of laser fabricated PNT for optical sensors, this is of vital importance. All of the absolute reflectance and

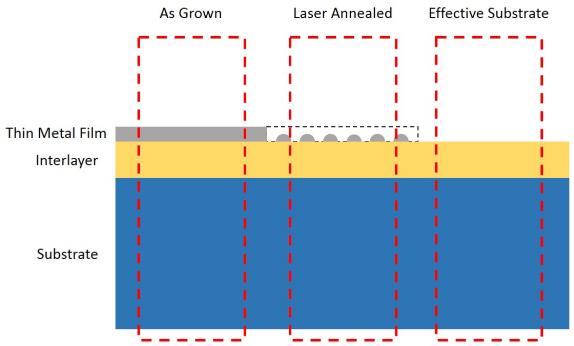

Figure 3.10: Schematic showing the three distinct areas of every laser processed sample: the 'As Grown' area; the 'Laser Annealed' areas; and the 'Effective Substrate' area.

reflectance relative to effective substrates have an error bar indicating the error in the spectral position of the primary LSPR peak, generated from measurements of duplicate samples. This error is between 3 and 5 nm for all samples discussed in this work.

3.7.2 Raman Spectroscopy

The technique of Raman spectroscopy allows for the accurate identification of a chemical molecule *via* monochromatic optical probing (usually using a laser source) of the vibrational states of specific chemical bonds through the analysis of the scattered light. Raman scattering can be subdivided into Stokes and anti-Stokes scattering, where by the frequency of the scattered photon is distinctly different to that of the probing photon by one vibrational energy mode, as show in in figure 3.11. The inelastic nature of the Raman signal results in Raman scattering being an inherently weak phenomenon when compared to an elastic event such as Rayleigh scattering, where it can be considered that 1 in 10 million scattering events are Raman events. Raman scattering most often refers specifically to Stokes scattering, where there is a specific red-shift to the scattered photon. While it is possible to acquire a Raman spectrum using anti-Stokes scattering, the necessary population inversion of the vibrational states (see figure 3.11) further reduces the number of relevant scattering events. Despite this, due to its specificity, reliability and ease of use, Raman scattering has become a technique that is universally recognised and widely used across the entire scientific community for chemical identification [138, 139].

Raman spectroscopy systems are designed around a traditional scattering system, where a narrow bandwidth laser source is used. Raman spectroscopy is compatible with a wide range of wavelengths, from ultra-violet (244 nm - 364 nm) to visible (457 nm - 660 nm) to infra-red (785 nm - 1064 nm), as the characteristic Raman peaks are independent on the incident

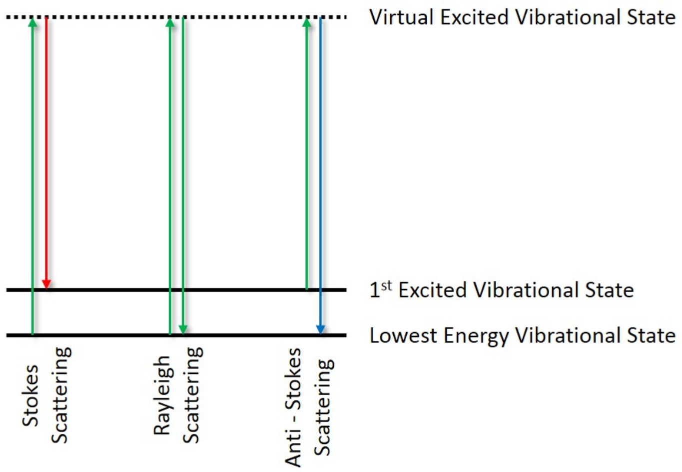

Figure 3.11: Diagrammatic view of the mechanisms behind Stokes, anti-Stokes and Rayleigh scattering.

(pumping) wavelength. However, wavelength selection can have a significant influence on the experimental results based on the material under investigation: infra-red wavelengths act to suppress fluorescence; while visible wavelengths are more suited to inorganic materials; and ultra-violet wavelengths allow for improved assessment of bio-molecules. In addition to selection based on material type, the wavelength of the Raman system directly influences the signal to noise ratio, as the Raman scattering is proportional to the frequency (ν^4) [138].

There are two main variations of a Raman spectroscopic systems, either a 90° or 180° systems, where the angle dictates the detection angle of the Raman scattered signal. A 90° system, most commonly used for assessing a liquid sample, is one where the pumping laser and the scattered signal are perpendicular. While in a 180° system, both the pumping laser and the Raman signal pass through the objective lens (this style is more common and are generally described as a Raman microscope), as shown in figure 3.12 [138].

Despite the power of Raman spectroscopy, the inherent weakness of Raman spectroscopy is the necessity for inelastic scattering events. This has led to extensive research into a methodology for increasing the intensity of the Raman signal. Since the discovery of an increase in the measured signal from a roughened silver electrode, Surface Enhanced Raman Spectroscopy, or SERS [140–143], has become a tool that has led to Raman spectroscopy being able to detect single molecules. SERS makes use of plasmonic nanoparticle templates to enhance either the Raman scattered light, or the probing laser line and can significantly enhance the signal by many orders of magnitude, as shown in equation 3.15 [144], where M_{Surf}/M_{Raman} is the number of molecules excited during the SERS and Raman spectra, S_{Surf}/S_{Raman} is the geometric area of the analyte

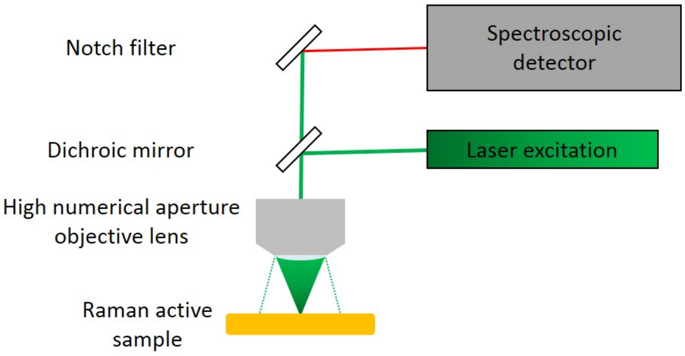

Figure 3.12: Diagram of a 180° Raman spectroscopic microscope.

film and I_{Surf}/I_{Raman} is the intensity of the SERS and Raman measurement respectively. The ideal SERS surface must have a high uniformity (monodisperse nanoparticle size distribution and uniform interparticle distance) and provide a high field enhancement (*via* the LSPR effect). Such surfaces are commercially available, on a rigid substrate. However, to date there does not exist a robust and flexible SERS surface, either within the literature or commercially.

$$G = \frac{I_{Surf} x S_{Surf} x M_{Raman}}{I_{Raman} x S_{Raman} x M_{Surf}} \tag{3.15}$$

In this research, Raman spectroscopy and a Raman microscope has been used to identify the unique Raman spectra from specific compound(s), as well as using SERS to assess the ability of a plasmonic nanoparticle template to enhance this signal.

3.8 Surface Analysis

Wolfgang Pauli once said *God created the volume, but the surface was invented by the devil.* As the surface of any material at any scale, represents an interface between two phases, the physical and chemical properties at the surface will differ, in some cases significantly, from those of the bulk material. This effect is felt predominantly in the top most atomic layers of the material and is of note when one considers the extent to which scientific research focuses on the controlled structuring and usage of surfaces. This work has used surface characterisation to assess the exact nature of the surface morphology, of both the as grown and the laser processed areas, as well as to quantify the exact atomic makeup of the sample surface.

3.8.1 Scanning Electron Microscope, SEM

A scanning electron microscope, or SEM, functions fundamentally in the same way as a traditional optical microscope, where in place of a white light source, a focused electron beam is scanned, sometimes described as rastering, across the sample surface as shown in figure 3.13. As a SEM makes use of electrons in place of photons of light, the resolution is not limited by the diffraction limit, as the De Broglie wavelength of an electron is significantly smaller than the wavelengths of visible light, which allows a skilled user to achieve images with up to 1 nm resolution.

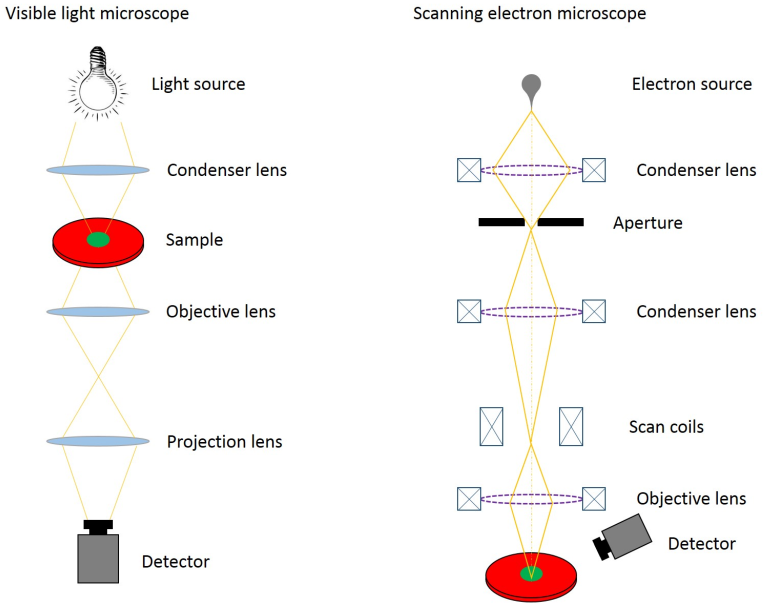

Figure 3.13: Schematic comparison of a visible light microscope and a scanning electron microscope.

At heart, a SEM comprises of:

- An electron source
- An ultra-high vacuum column containing a series of apertures, electromagnetic lenses and scan coils
- A high vacuum sample chamber
- A selection of electron detectors
- A computer interface.

When the electron beam impacts the surface of a sample, the electron beam penetrates the sample surface, to a depth depending on the accelerating voltage applied, with interactions at different depths producing different signals, for example reflected or backscattered electrons, secondary electrons and x-rays, as shown in figure 3.14. Each interaction often requires the use of a specifically optimised detector. A SEM can be fitted with a variety of electron sources, including a tungsten filament (SEM) or a field emission gun (FEG-SEM). The electron source dictates the nature of the electrons in the beam, as a tungsten filament produces hot electrons *via* thermionic emission, while a field emission gun uses field electron emission. A field emission gun produced by applying a high voltage across a sharpened single tungsten crystal so that the potential difference at the tip causes electron emission. This allows for improved imaging resolution as the electron beam is narrower, significantly brighter and has improved coherence than the beam produced by a tungsten filament under the same voltage. The narrowness of the electron beam in a FEG-SEM acts to increase the depth of field, allowing for greater topographical information and a characteristic 3D appearance to the SEM micrographs [145].

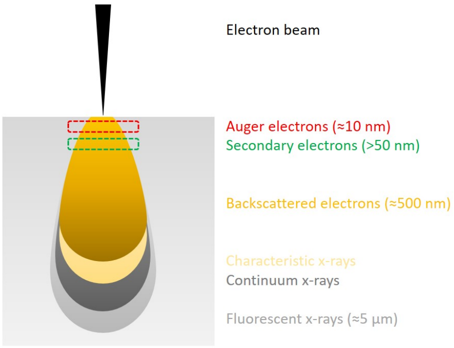

Figure 3.14: Diagram showing the different electron interactions possible as a function of depth below the surface.

This research uses a FEG-SEM to achieve high resolution micrographs of the structure of the fabricated nanoparticle templates and the as grown thin films. This enables an understanding of the exact surface structure - size, shape and surface distribution - of the nanoparticles, as well as how subsequent laser pulses influence this structure. In combination with the optical response, quantified *via* ORS, it is possible to have a complete understanding of the nature of a plasmonic nanoparticle template.

3.8.2 X-ray Photoelectron Spectroscopy, XPS

X-ray photoelectron spectroscopy (XPS), sometimes called electron spectroscopy for chemical analysis or ESCA, is a highly sensitive technique for the assessment of the elemental composition (apart from hydrogen); chemical sate of the cations or anions; and the chemical shift of the sample surface. XPS is a surface characterisation method that is used universally by physicists, chemists and material scientists. One of the key reasons for the widespread usage of XPS, is its extreme surface sensitivity, as the phenomenon at the heart of XPS is the photoelectron effect. An XPS scan will probe up to a maximum depth of 3 nm below the surface, ensuring that the analysis contains surface specific information that is not diminished by the signal from the bulk material [146].

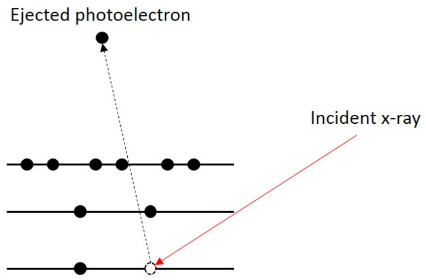

Figure 3.15: Schematic of the photoelectron effect, where the energy of the incident x-ray must exceed the work function of an electron to eject it.

The photoelectron effect [147] occurs when an incident photon, generally ultra violet and above, with enough energy to overcome the work function of the material, causes the ejection of an inner shell electron, as shown in figure 3.15. The kinetic energy of the released electron is dependent on the energy of the incident photon and the work function or binding energy:

$$E_{kinetic} = hf - E_{binding} \tag{3.16}$$

While it is the kinetic energy of the electrons that is detected by the XPS system, through a hemispherical analyser, it is the characteristic, material specific binding energy that allows for such reliable elemental identification.

$$E_{binding} = hf - E_{kinetic} \tag{3.17}$$

The hemispherical analyser is an electrostatic system which acts to separate the incoming electrons according to their kinetic energy, such that electrons with higher energies travel through the analyser with a larger radius, working in a similar way to a prism splitting light by wavelength according to the speed of the different wavelengths of light in the medium. The analyser consists or two hemispheres with a potential applied between them, where electrons enter the analyser, undergo dispersion and exit to a detector [146]. This research uses XPS to identify the surface

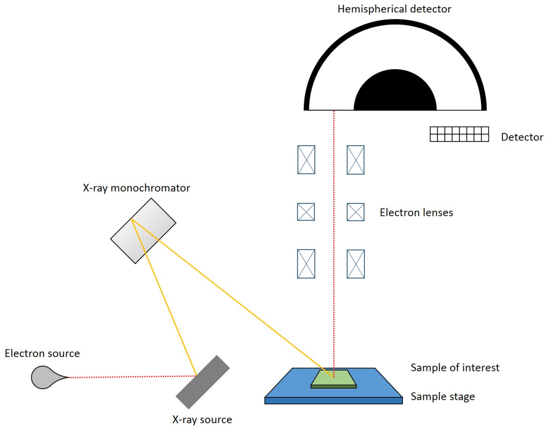

Figure 3.16: Schematic of an XPS system. Electron beam paths are shown in red, while x-ray paths are shown in yellow.

presence and abundance of specific compounds and ions on a plasmonic nanoparticle template after the deposition from solutions at predetermined concentrations. XPS was selected because of its high surface sensitivity, allowing low quantities of a material at the surface being detected, as other, more penetrating surface analysis techniques lose surface specificity due to the increased contribution form the bulk material.

Chapter 4

Naked Nanoparticle Localised Surface Plasmon Resonance Spectroscopy

4.1 Introduction

This chapter will discuss an investigation into the use of a naked, or nonfunctionalised, laser fabricated plasmonic nanoparticle template as a LSPR spectroscopy sensing surface for the detection of heavy metals, like lead, adsorbed from solution. Detailed studies of the fabrication of these plasmonic nanoparticle templates as a function of laser fluence and the number of treatment pluses are shown to achieve a sensing surface with the greatest possible sensitivity, as well as the response from the fabricated nanoparticle templates after exposure to solutions of specific concentrations.

4.1.1 Localised Surface Plasmon Resonance Spectroscopy

Surface sensing has a number of advantages when compared to solution sensing: it requires less sample for testing; can be easily scaled up; can provide real time analysis; and enables multiple parallel assays to be run on a single sensor [148], allowing for duplexed sensing. Of note is that label-free sensing, such as LSPR spectroscopy, have been seen to achieve comparable sensitivity with the more common labelled sensing such as ELISA [149]. To the extent that label-free surface sensing has been shown to be able to detect biological analyte in the attomolar regime, proving the power and sensitivity of surface sensing [139].

LSPR spectroscopy, is a highly sensitive, label-free surface sensing platform, where the optical response of a nanoparticle templates is assessed before, during and after a given process has occurred, for example a drug delivered to a specific site of the growth of a thin film. The resultant optical reflectance shift caused by the process being completed or at any given point during it can be calculated [139]. LSPR spectroscopy makes us of the extreme sensitivity of a plasmonic nanoparticle template (or single plasmonic nanoparticle) to minute changes in the local dielectric environment or refractive index, due to either surface adsorption or a chemical reaction. The sensitivity can be favourably compared with other surface sensing techniques, with the additional benefit of simplified sensor fabrication - as at a fundamental level, all that is needed is a nanoparticle template [150]. In addition to this, the low cost of the necessary measurement instrumentation - a way to measure the real-time reflectance of the sensor - results in a surface sensing technique that has gain remarkable popularity. Although LSPR spectroscopy has found a home within pharmacology [151], it has become increasing popular as a method for measuring the surface absorption of heavy metals [152–155]. This area of research is of significant real-world importance as a build-up of heavy metals in the human body have severe negative effects on health with the additional concern that there is no biological route to dissipate this build up. While it may be natural to compare LSPR sensing with surface plasmon polariton (SPP) sensing [156], LSPR spectroscopy has several advantages when compared to SPP sensing, the most prevalent of which are the greater surface sensitivity and reduced sensitivity to bulk index changes in the solution because of the reduced field decay length [**?**].

While LSPR spectroscopy offers a diverse sensing platform that can be used to assess both the progress and successful completion of a given process, a distinct issue towards the more widespread usage of LSPR spectroscopy is the necessity to functionalise the plasmonic nanostructure. This functionalisation, while greatly advantageous, as it promotes maximum and uniform surface adsorption of the analyte, the necessity of its use adds an obvious level of complexity to the sensor fabrication. While vital in some cases, particularly when considering the case of a duplexed sensor, it acts to limit the more widespread use of LSPR spectroscopy by adding an inherently complex process to fabrication and simultaneously limits the possible usage of the single sensor to the analyte favoured by the functionalisation.

It was suggested that in the case where the surface adsorption of the analyte was assured by a separate mechanism, such as filtration, the need to utilise a process designed to maximize surface adsorption would be greatly diminished if not negated completely. As such, it was further suggested that if a LSPR spectroscopy-based sensing surface could be built into the surface of a water filter, a filter specifically designed to selectively filter heavy metals for example, where the surface adsorption was guaranteed by said filter, then it could be possible for a LSPR spectroscopy sensor to be functional without the need for functionalisation. Heavy metal poisoning, defined as the build-up of a heavy metal(s) in the soft tissues of the body to a toxic level [157], is a serious problem as there is no biological route for the removal of these heavy metals from the body, and chronic exposure can lead to serious physical and mental symptoms from muscle tremors, low circulation and unexplained pain to mood swings, forgetfulness and depression.

From this, a series or research objectives were established, where the successful completion of each would provide enough evidence to claim that naked nanoparticle sensing is applicable in certain applications:

- Fabricate and assess the optical response of a series of plasmonic nanoparticle templates.
- Prepare a series of solutions of a heavy metal, across a range of suitable concentrations.
- Assess the optical response of the plasmonic nanoparticle templates after the evaporative deposition of the heavy metal from solution.
- Identify any spectral shift due to the suspected surface presence of the heavy metal.
- Quantify the surface composition of the nanoparticle templates to identify the surface abundance of the heavy metal.
- Investigate if it is possible to correlate the surface abundance of the heavy metal to the measured spectral shift.

Where these research objectives were used to produce a research plan described below, with figure 4.1, showing a diagrammatic version of the experimental plan.

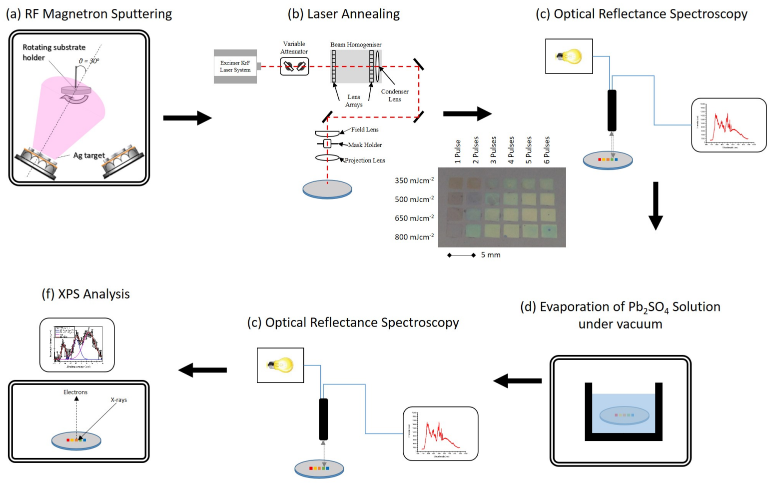

Figure 4.1: Diagrammatic visualisation of the experimental methodology used for the fabrication, processing, treatment and characterisation applied in this work. Beginning with (a) the fabrication of a silver metallic thin film, (b) the laser annealing of this film, (c) its optical characterisation, (d) its treatment with the various concentrations of lead salt solutions and finally (e) the post treatment optical characterisation and (f) analysis with XPS.

4.2 Experimental Results

4.2.1 Proof of Concept

The first and most vital stage of this investigation is to identify a suitable material to monitor the surface presence of. One of the most common heavy metals associated with heavy metal poisoning is lead, it was a clear candidate for this work as in addition to the detection of metallic lead we would be able to identify in parallel the presence of any lead salts.

As such, an aqueous solution was prepared to the maximum possible solubility, 44 part per million (ppm), of the selected lead salt, in this case lead (II) sulphate (Pb_2SO_4) for the initial testing with a series of laser fabricated naked PNTs. As an increasingly popular use of LSPR spectroscopy is as a filtration monitoring system, a lead salt was selected due to leads high toxicity and the inherent necessity to have be able to assess its abundance in any given water supply. While other lead salts are available, with higher water solubility, most are salts containing nitrogen, chlorine or iodine which could react with the silver nanoparticles, significantly reducing or even quenching the LSPR response of the nanoparticle template. The initial testing would be conducted by placing a fixed volume of the aqueous solution atop each of the individual nanoparticle templates and allowing the solution to evaporate to mimic the action of a filtration surface actively trapping the analyte. This process would act to provide an insight into how the various types of nanoparticle template morphologies would influence the ability of that template to act as a sensing surface as well as identifying the morphology that could provide the greatest spectral shift.

Consequently, a number of grids of PNT's were produce for this work fabricated from a thin layer of silver (Ag) on a commercial, 4" n-type silicon (Si), (100) wafer substrate with the associated native oxide layer. The precursor discontinuous silver thin film was fabricated *via* radio frequency magnetron sputtering (RFMS) in a high vacuum chamber (base pressure of $< 10^{-6} mbar$), from a round (3") Ag target (99.99% purity), in the presence of argon (Ar) (99.999% purity), at a fixed flow rate of 4 standard cubic centimetres per minute (sccm) resulting in a working pressure of 5 mTorr in the vacuum chamber. The power applied to the target was set to 40 W while the Si substrates was rotated at 12 revolutions per minute (rpm) to ensure a uniform deposition. Finally, the deposition time was set in conjunction with the use of a quartz crystal microbalance to achieve an effective thickness of 10 nm.

Initially is was unknown which nanoparticle morphology would be best suited for a sensing surface. However, it was clear that an assessment of as wide a range of surface structures, including bimodal and monodisperse arrangements, in addition to hemispherical and multifaceted nanoparticles, would allow for the best understanding of any influence on the sensing ability due to templates morphology. As such, following the growth process, the Ag film was subjected to a UV MONA-LISA process. The initial LISA process is a rapid thermal process, where the high absorption of the processing wavelength in an active, discontinuous layer, most commonly a metallic thin film, induces a dramatic local temperature rise of up to 5000 °K, where the temperature rise is proportional to the heat conduction of the thin film material. When the temperature rise is above the melting temperature of the thin film material, the material undergoes a phase transition and melts. The molten metal poorly wets the substrate, where the poor wetting of the substrate increases the likelihood of the liquid phase breaking up. Subsequently the molten metal experiences a heightened rate of cooling at the edges, and the molten metal breaks into nano-scale droplets due to the Rayleigh instability and cools back to the solid state producing a PNT [130–132]. The time necessary for the metallic film to achieve room temperature, or cooling time, is comparable to the pulse length of the processing laser (25 ns). Such nanoparticle templates are often bimodal in nature, where there are two distinct families of nanoparticle sizes, one larger and one smaller, giving rise to a characteristic double peaked optical response. At higher laser fluences (energy densities), the size difference of the two nanoparticle families is reduced. The following pulses change the surface morphology, or cause a modification of the nanoparticle arrays (MONA) [128]. This process is driven by the selective heating of the larger nanoparticles, which melt and reform into smaller nanoparticles, where there is a mass transfer to the pre-existing smaller nanoparticles, in the opposite action to that described by Ostwald ripening, allowing for multiple laser pulses to form a more homogeneous nanoparticle template. This allows of a minimised size distribution. This was done using a Lambda Physik LPX 305i, krypton fluorine (KrF) excimer laser system, delivering unpolarised 248 nm light at up to 1200 mJ per pulse (25 ns pule width, 1 Hz repetition rate). The sample was exposed to four specific fluences: $350mJcm^{-2}$, $500mJcm^{-2}$, $650mJcm^{-2}$ and $800mJcm^{-2}$, with 6 different numbers of treatment pulses, 1, 2, 3, 5, 10 and 15 pulses to produce 24 individual PNTs.

Due to the hydrophobic nature of the PNTs, the aqueous solution was seen to exhibit a contact angle of between 74°and 61°, prevented the uniform wetting of the entire nanoparticle templates as shown in figure 4.2, where the deposition pattern exhibited a distinct and highly terraced coffee-ring.

From this, it was concluded that to more reliably assess the ability of naked nanoparticle templates to operate as a LSPR spectroscopy sensor, a method was needed to alter the wetting conditions. As the wetting of a surface by a liquid depends on the surface and the liquid equally, it was concluded that the preferred methodology would be to modify the lead solution. This was identified as the appropriate method for a variety of reasons, but primarily it was selected due to the existing evidence that creating a binary liquid with an alcohol would influence the wetting

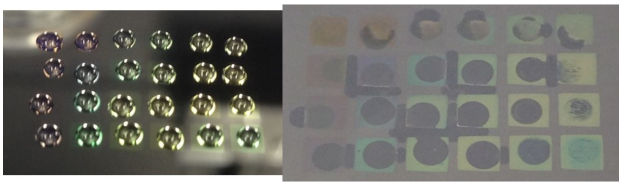

Figure 4.2: Images of $2\mu L$ droplets of 44 ppm aqueous solution of lead (II) sulphate on each of the plasmonic nanoparticle templates, before (*left*) and after (*right*) the solution has evaporated.

sate [158], in addition to the fact that any surface modification of the nanoparticles would run counter to the goal of this work.

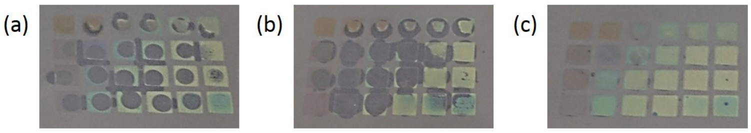

Figure 4.3: Images of $2\mu L$ droplets of: (a) 100:0 aqueous $PdSO_4$ to ethanol; (b) 75:25 aqueous $PdSO_4$ to ethanol; and (c) 50:50 aqueous Pd_2SO_4 to ethanol, evaporated on a series of plasmonic nanoparticle templates, fabricated with $350 - 800 mJcm^{-2}$ and 1-15 pulse.

Subsequently, the 44 ppm solution was mixed to produce a series of different ratios of aqueous $PbSO_4$ to ethanol, to identify the mixture that would allow for the most uniform wetting of the nanoparticle templates. As expected from the available literature, the most uniform wetting exhibited by the 50:50 mixture, as shown in figure 4.3(c). As the lead salt used in this work is insoluble in alcohol, it was found that if the ethanol ratio was increased beyond 50%, then the Pb_2SO_4 salt would precipitate out of the solution. Additionally, as can be seen in figure 4.4, there was a dramatic change to the static contact angle caused by the introduction of the ethanol, allowing for significantly greater surface wetting.

From the evaporation of the 22 ppm solution of 50:50 aqueous $PdSO_4$ and ethanol, it was possible to identify if one of the naked nanoparticle templates was able to show a spectral shift due to the surface presence of metallic lead and the lead salt. This can be clearly identified from the comparison of the reflectance after the evaporation of a 0 ppm solution (50:50 solution of water and ethanol) and a 22 ppm solution of $PbSO_4$ in aqueous ethanol, as shown in figure 4.5, where the calculated spectral shift can be seen in figure 4.6.

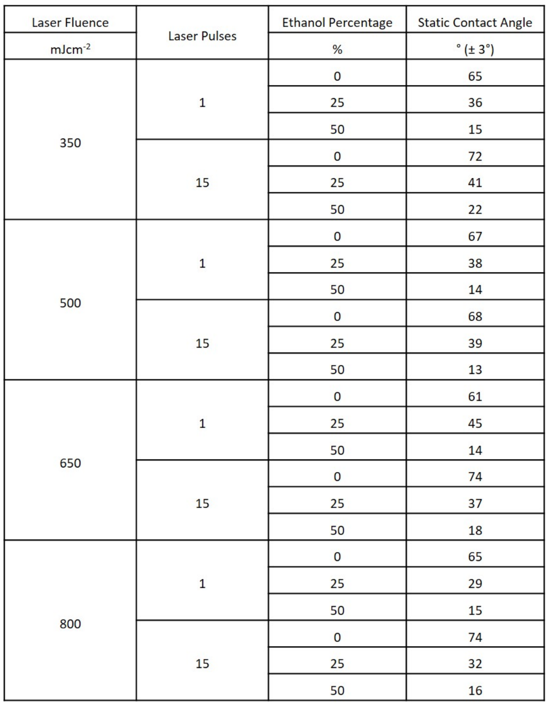

Laser Fluence $mJcm^{-2}$	Laser Pulses	Ethanol Percentage %	Static Contact Angle ° (± 3°)
350	1	0	65
		25	36
		50	15
	15	0	72
		25	41
		50	22
500	1	0	67
		25	38
		50	14
	15	0	68
		25	39
		50	13
650	1	0	61
		25	45
		50	14
	15	0	74
		25	37
		50	18
800	1	0	65
		25	29
		50	15
	15	0	74
		25	32
		50	16

Figure 4.4: Tabulated static contact angle measurements of the $350-800mJcm^{-2}$ 1 and 15 pulses templates, showing the influence of the ethanol concentration on the contact angle achieved on each of these PNTs.

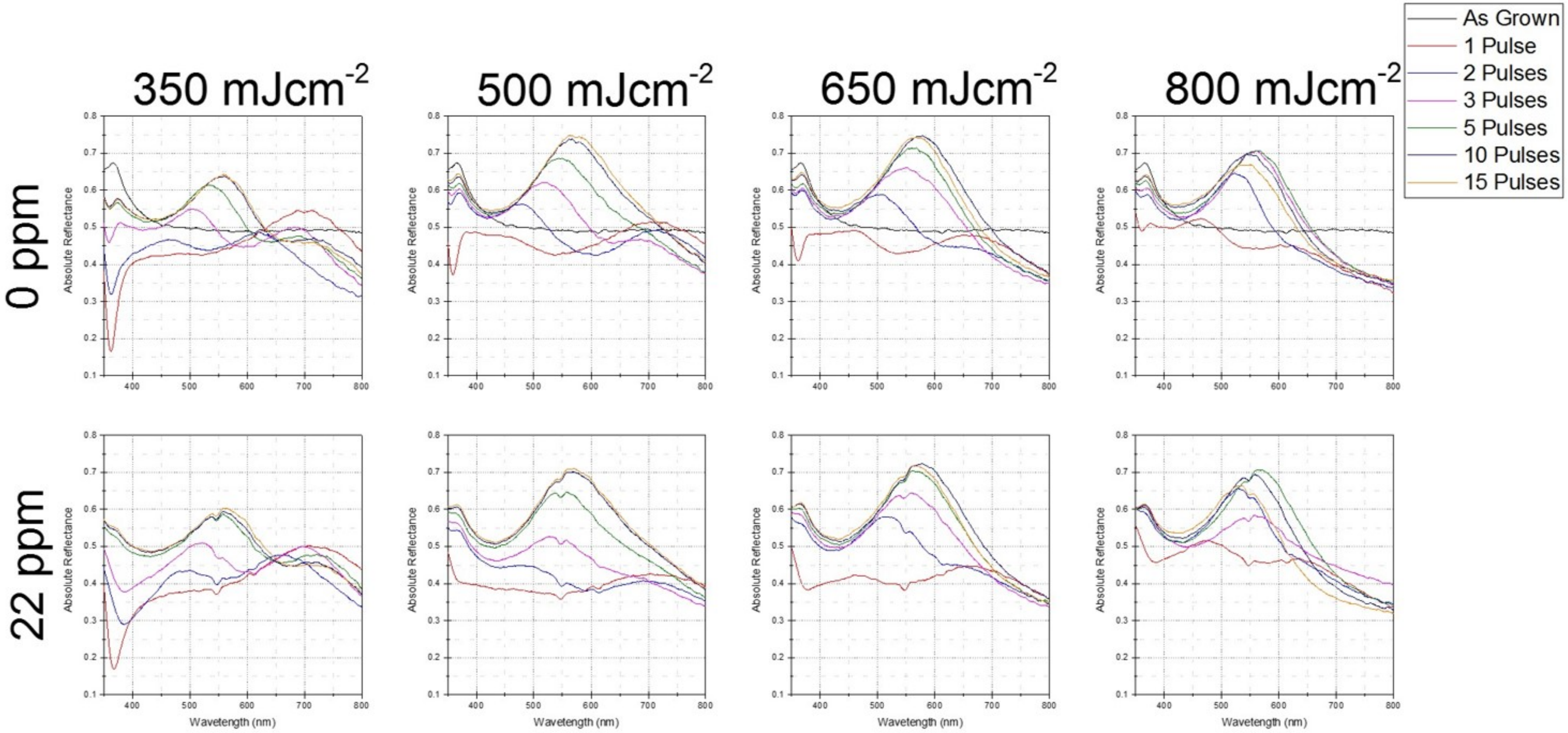

Figure 4.5: Comparison of the calculated absolute reflectance of the as fabricated plasmonic nanoparticle templates, after the exposure to a: 0 ppm $PbSO_4$ aqueous ethanol solution (*top row*); and 22 ppm $PbSO_4$ in aqueous ethanol solution (*bottom row*).

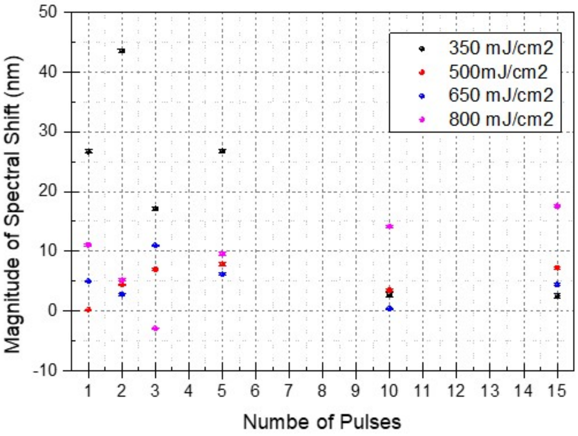

Figure 4.6: Comparison of the measured spectral shift across all of the produced plasmonic nanoparticle templates shown in 4.5.

From the analysis of the optical reflectance of these laser fabricated PNTs, the spectral shift ($\Delta\lambda$), can be calculated as the magnitude of the difference between the spectral position of the primary reflectance peak before and after the evaporation of any solution and the position of the same peak after the evaporation of the 22 ppm solution, as $\Delta\lambda = \lambda_{Peak0ppm} - \lambda_{Peak22ppm}$. While it was initially hypothesized that a monodisperse arrangement of hemispherical nanoparticle would offer the greatest spectral shift, it was necessary to assess the individual PNTs to see if this was correct. In the case that the nanoparticles presented a bimodal distribution, where there exist two distinct nanoparticle size families with correspondingly two unique optical reflectance peaks were apparent in the reflectance profile, both peaks were assessed individually. While it was evident that there was a distinct and measurable spectral shift caused by the evaporation of the $PbSO_4$ solution, it was equally evident that the spectral shift observed was not constant from all the templates, as shown in figure 4.7. As each PNT was treating identically, with the same solution, it can be concluded that this variation in the magnitude of the spectral shift seen from one PNT to another must be caused by the surface morphology. It can be seen that while there are distinct differences in the optical reflectance measured for the PNTs produced with 1 pulse, it is evident that the nanoparticle templates fabricated with successive laser treatment pulses, such as 5 and 10 pulses, the spectral shift is diminished, resulting in spectral shifts up to a maximum of 10 nm for 10 pulses and decreasing even further to 3 - 5 nm for 15 treatment pulses, as highlighted in figure 4.8. Therefore, it was concluded that, in contradiction to the original theory, that the preferred morphology for a PNT to be used as a surface sensing platform is a bimodal distribution.

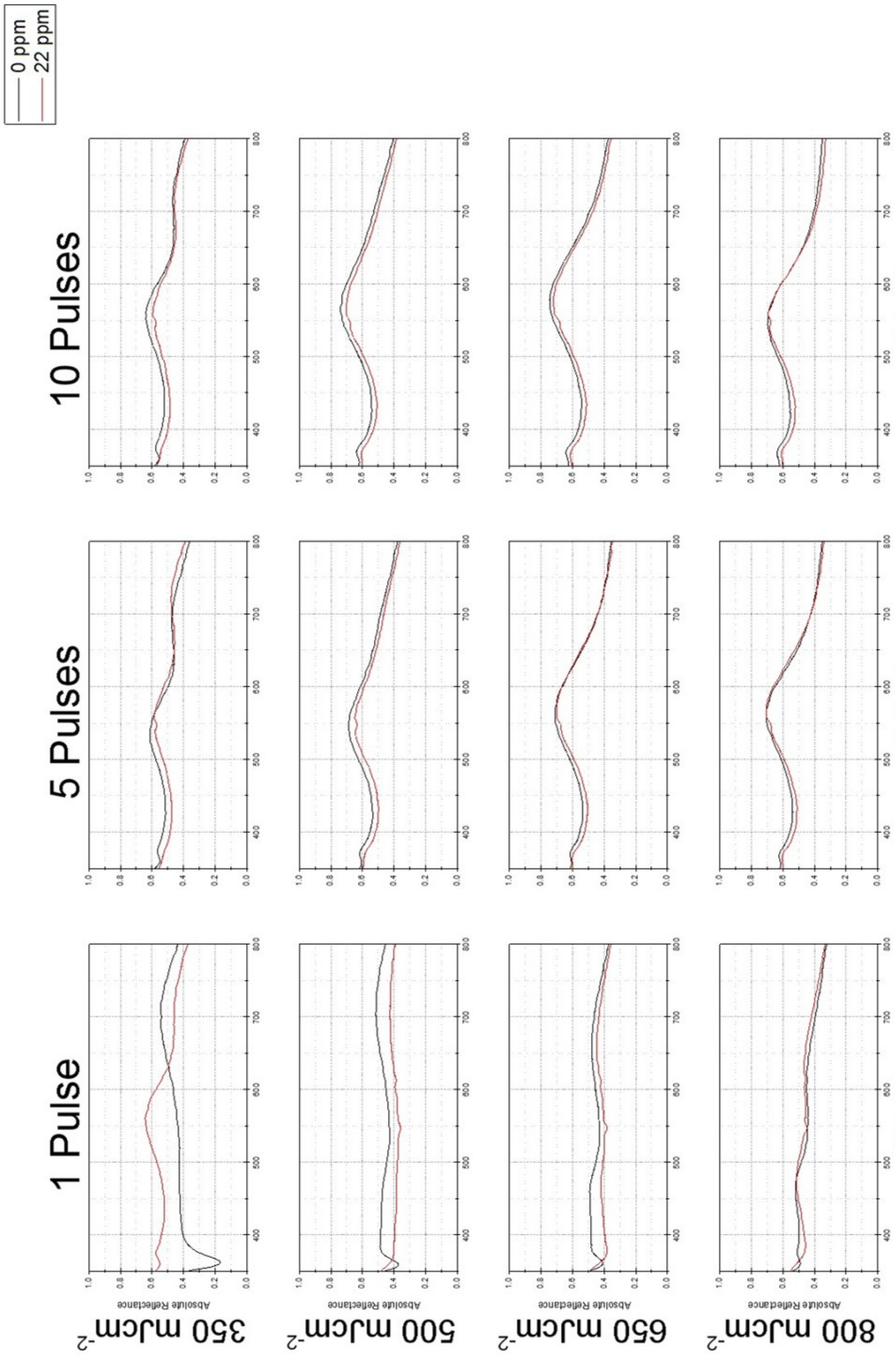

Figure 4.7: Comparison of the optical reflectance seen after the evaporation of a 22 ppm $PbSO_4$ in aqueous ethanol solution for selected PNTs to show the variation in spectral shift based on the nanostructure present.

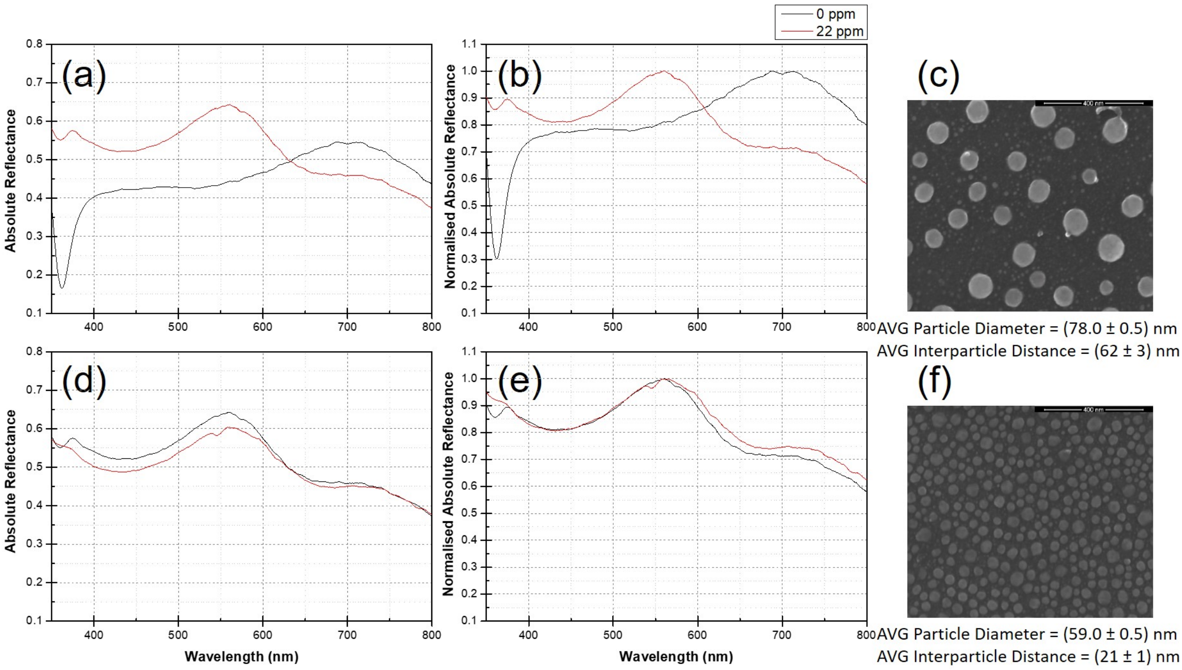

Figure 4.8: Normal incidence optical reflectance spectroscopy (ORS) spectra showing the absolute reflectance of the nanoparticle templates fabricated with $350mJcm^{-2}$ and (a) 1 pulse and (d) 15 pulses as fabricated (0 ppm) and after the evaporation of the 22 ppm Pb2SO4 solution. Spectra (b) and (e) show the normalised absolute reflectance for these two nanoparticle templates. SEM micrographs (c) and (f) show the surface morphology for the 1 and 15 pulses templates respectively.

4.2.2 Naked Nanoparticle Sensing

From this, it was decided that a series of new identical PNT grids would be produced on a single silicon wafer substrate, using the same laser fluences as previously ($350 - 800mJcm^{-2}$), but with a different pulse progression of 1 - 6 pulses, as it was evident that with 5 treatment pulses there was a low spectral shift and the use of further treatment pulses did not equate to a greater spectral shift. In parallel to the production of these UV MONA-LISA grids, a series of Pb_2SO_4 in aqueous ethanol solutions, at the 50:50 ratio previously identified, of 0, 4, 8, 12, 16 and 20 ppm were produced to assess the sensitivity of these naked nanoparticle templates. Due to the low maximum solubility of Pb_2SO_4 in water ($44ppm$) and its insolubility in alcohol, higher concentrations could not be produced. Now it would be possible to have one laser fabricated grid to remain untouched and act as a control, while each of the remaining six grids could be tested with an individual concentration. It was further considered that in place of the individual treatment of each PNT with a fixed volume droplet, each of the PNT grids would be initially washed with 0.1 mL of pure ethanol, to minimise surface contamination and then submerged in 0.2 mL of the specific concentration solution, as this would be analogous to the situation that a real time sensor would experience. Once exposed to the specific solution, the PNT grid was placed within a vacuum chamber to simultaneously speed up the evaporation, or drying time, as well as acting to maximise as much as possible the uniform wetting and prevent the formation of a coffee-ring.

From the UV MONA-LISA grids produced as above, two of these laser fabricated plasmonic nanoparticle templates warrant greater discussion, namely $500mJcm^{-2}$ 1 pulse and $500mJcm^{-2}$ 6 pulses, described as 1x500 and 6x500 henceforth. These templates were selected due to the difference in their optical response after the evaporation of the various Pb_2SO_4 solutions, where the 1x500 template showed a systematic change in optical response with increasing solution concentration, while the 6x500 template did not show a strong relationship between the seen optical shift and the solution concentration. Additionally, both laser annealing conditions result in two distinct bimodal distributions of large NP's in a sea of smaller NP's, with differently sized nanoparticle families as seen in figure 4.9, where the 1x500 template showed a systematic change with solution concentration, while the 6x500 template showed an erratic variation of the spectral response. It was identified that the 1x500 template showed the most significant relationship between the Pb_2SO_4 solution concentration and the calculated spectral shift, while conversely the 6x500 template showed the least promising relationship, where the discrepancy can only be due to the nanostructure, suggesting that the quality of the produced sensor may depend heavily on the size, shape and surface coverage of the PNT. Despite the 6x500 nanoparticle template showing no clear link between the spectral shift and the solution concentration, it was identified that there was a clear spectral shift achieved with each solution, subsequently it was proposed that with further analysis it may be possible to gain an understanding of the reason for this erratic relationship.

Of particular note is the blue-shift or shift towards shorter wavelengths (negative values of reflectance shift), seen from both templates. This phenomenon runs contrary to the response seen with traditional LSPR spectroscopy, where the binding of the analyte to the functionalisation inducing a characteristic red-shift. This can be clearly understood when we consider a traditional LSPR spectroscopy, where the analyte is captured by the functionalisation, thereby altering the local dielectric environment and increasing the refractive index. However as in this work we present naked PNTs, the analyte, specifically Pb++ and PbSO3, have instead adsorbed directly onto both the metallic nanoparticles and Si substrate. Due to the difference between the Fermi energies (E_F) of silver and lead (5.49 eV and 9.47 eV respectively), the physical proximity of the atoms could allow for an electron transfer from higher energy states in the lead to vacant, lower energy states in the conduction band of silver until an equilibrium state was achieved. This transfer of electrons, would increase the number of electrons within the silver, increasing the number of oscillators and shifting the plasma frequency to higher energies, where this can be seen diagrammatically in figure 4.10.

Essential for the assessment of the naked nanoparticle templates to relate the spectral shift to the concentration of the solution, a LSPR spectroscopy sensor is used to assess the surface abundance, through adsorption, of the analyte. As such, a highly sensitive methodology for quantifying the surface composition and abundance of the PNT's was required. It was identified that XPS would be used to accurately identify the surface state of the 1x500 and 6x500 PNTs, to quantify both the surface composition and the chemical state of the sensor surface. These selected PNTs were analysed at Aristotle University of Thessaloniki, in collaboration with Professor Panos Patsalas and group, using an Axis Ultra DLD XPS system, equipped with: a monochromatic Al $K\alpha$ x-ray source; a 0.5 m hemispherical analyser; and a multichannel detector. The XPS measurements were acquired using a pass energy of 20 eV resulting in a full width at half maximum (FWHM) of the Ag-3d peak of less than 500 meV. An example of the acquired spectra can be seen in figure 4.11.

The surface abundance and chemical state analysis of these PNTs showed that, in addition to Si and Ag, inherent to the structure of the nanoparticle templates, and trace amounts of C and O, the XPS showed significant amounts of lead as both metallic Pb^{++} and $PbSO_3$, with their 4f peaks separated by a characteristic 5.2 eV, as shown in figure 4.12 (a and b). Again, it is clear for the 1x500 template, that there is a strong link between the measured spectral shift and the quantity of lead adsorbed to the nanoparticle surface, while the 6x500 template again shows little link, provided further evidence that the 1x500 template offers the superior sensing surface. As shown in figure 4.12 (c), for the 1x500 template the surface abundance of silicon decreases with the abundance of lead, we can conclude that, as both Pb^{++} and $PbSO_3$ ions, the lead from the solution will preferentially adsorb to the silicon in the gaps between the silver nanoparticles and when we consider 4.12 (d), we can see that the 6x500 template does not show the same type of response, suggesting that the lead is forces to adsorb directly to the nanoparticles themselves.

The true power of a LSPR spectroscopy sensor is derived form the ability to quantify the surface presence of an analyte with a simple optical measurement. Therefore, to assess the ability of these naked nanoparticle templates as a LSPR spectroscopy sensor style for detecting and monitoring the presence of a heavy metal, in this case lead (as both Pb^{++} and $PbSO_3$), it is essential to correlate these two factors and to produce a calibration. In addition to a direct calibration between the spectral shift and the surface abundance of lead, it is possible to produce a calibration between the spectral shift and the original solution concentration. In a real-world environment, these two calibrations would allow for a single optical measurement to provide information on both these factors simultaneously.

In the case of the 1x500 template, it was clear that such quantitative calibrations could be produced due to the proportional nature of these two relationships. Conversely, from the spectral shift and XPS results of the 6x500 template, it was clear that no quantitative relationship between either the spectral shift and the solution concentration or the measured surface abundance of lead and the spectral shift existed. Due to this, it was concluded that no further use could be made of the 6x500 template, as there was no benefit using this template for an exclusively qualitative comparison.

Due to the high level of reliability in the assessment of the spectral shift (maximum error across 3 samples of $\pm 8nm$), the limit of detection for the identification of the surface abundance of the Pb_2SO_4 could be defined as any measurable spectral shift greater than 8 nm. However, as can be seen in 4.13, there is an measured spectral shift of 38 nm from the 0 ppm solution (equal mixture of ethanol and water), a realistic limit of detection should be considered to be a spectral shift of greater than or equal to 40 nm. This spectral shit equates to a solution concentration of 4.5 ppm and a surface abundance of 0.009 atomic% of lead at the surface.

$$SurfaceAbundanceofLead(at\%) = -1.9 \times 10^{-4} \times \Delta\lambda(nm) + 1 \times 10^{-3} \tag{4.1}$$

$$SolutionConcentration(ppm) = -0.29 \times \Delta\lambda(nm) - 8 \tag{4.2}$$

4.3 Conclusion

Here we have presented an alternative, simplified yet sophisticated route towards the fabrication of a highly sensitive surface sensing platform, akin to a LSPR spectroscopy sensor, for the detection of the surface presence of a heavy metal, in this case lead. This has been achieved by utilising naked, or nonfunctionalised, nanoparticle templates which have the dual benefits of further simplifying the fabrication of the sensing surface and broadening the scope of a single surface. Here we have provided clear evidence that the lack of functionalisation does not equate to the lack of a sensor. We demonstrate that when the surface adsorption of an analyte is ensured *via* a separate mechanism, in this case the evaporation of a solution under vacuum, a naked PNT can be used as a traditional functionalised template would be. We provide evidence for this by demonstration that a naked nanoparticle template can be used to identify a surface abundance of lead as low as 100 ppm (0.01 atomic %), as both Pb^{++} and $PbSO_3$, from a little as 0.2 mL of solution.

Further to this, we have produced two calibration curves shown, in figure 4.13 and subsequent equations 4.1 and 4.2, that provide evidence that a naked nanoparticle template fabricated with 1 pulse of $500mJcm^{-2}$ can be used to accurately and quantitatively assess the surface abundance of both a given analyte and the original solution concentration, due in part to the clearly linear nature of these relationships.

When considering the potential real-world applications for such a sensing platform, with simple fabrication and necessary measurement equipment, could allow such a sensing system to be used to simultaneously assess the concentration of the water source and monitor the filtration process by quantifying the surface abundance on the filtration material, from a single optical measurement.

While this research aims to provide a clear and definitive proof of principle for the use of a naked PNT as a LSPR spectroscopy style sensing surface, the inherent hydrophobic nature of the nanoparticle templates used and the subsequent use of a binary water:ethanol solution to achieve uniform wetting, does necessarily hinder the potential for uptake as an *in situ* monitoring system. However, the use of the binary water:ethanol solutions were not necessary to make this work possible. Instead they were used to simplify the analysis by removing the need to qualify the influence of the water contact angle. To more accurately represent the intended real-world application, the XPS analysis was performed on samples that were submerged in the prescribed solutions rather than the solutions being drop cast on to the selected nanoparticle templates.

While 24 nanoparticle templates were investigated optically, only two were selected for further characterisation by XPS, to quantify the surface abundance of lead post evaporation. These two PNTs were selected because they represent two distinctly different surface topologies with the 1x500 template exhibiting large (80 - 110 nm) nanoparticles in a sea of much smaller (3 - 10 nm) nanoparticles, while the 6x500 template showed a more uniform distribution of smaller (20 - 60 nm) nanoparticles, but additionally because of their measured optical shift. While the 1x500 template showed an expected response, of the measured spectral shift generally increasing with the solution concentration used, the 6x500 template presented a distinctly different relationship, where there was minimal spectral shift that generally decreased with increased concentration. Of note was the fact that for both the 1x500 and 6x500 template, the 12 ppm solution induced the greatest spectral shift. Despite this unpromising result, the 6x500 template was further assessed with XPS to identify if the surface abundance of the lead would suggest that an additional way of assessing the change to the optical response would be required, such as to monitor the change of peak reflectance $(\Delta R) or the change in peak profile (FWHM/\lambda_{Peak})$. However, from the

XPS analysis it was evident that there exists a remarkably powerful link between the surface abundance and the spectral shift. As such, we here present that it is additionally possible to tune the sensitivity of a naked nanoparticle template through the modification of its nanostructure, allowing for the further simplification of the fabrication of a duplex sensor by producing a series of templates with different laser parameters rather than needing to accurately treat specific areas for traditional functionalisation while preventing any cross-contamination.

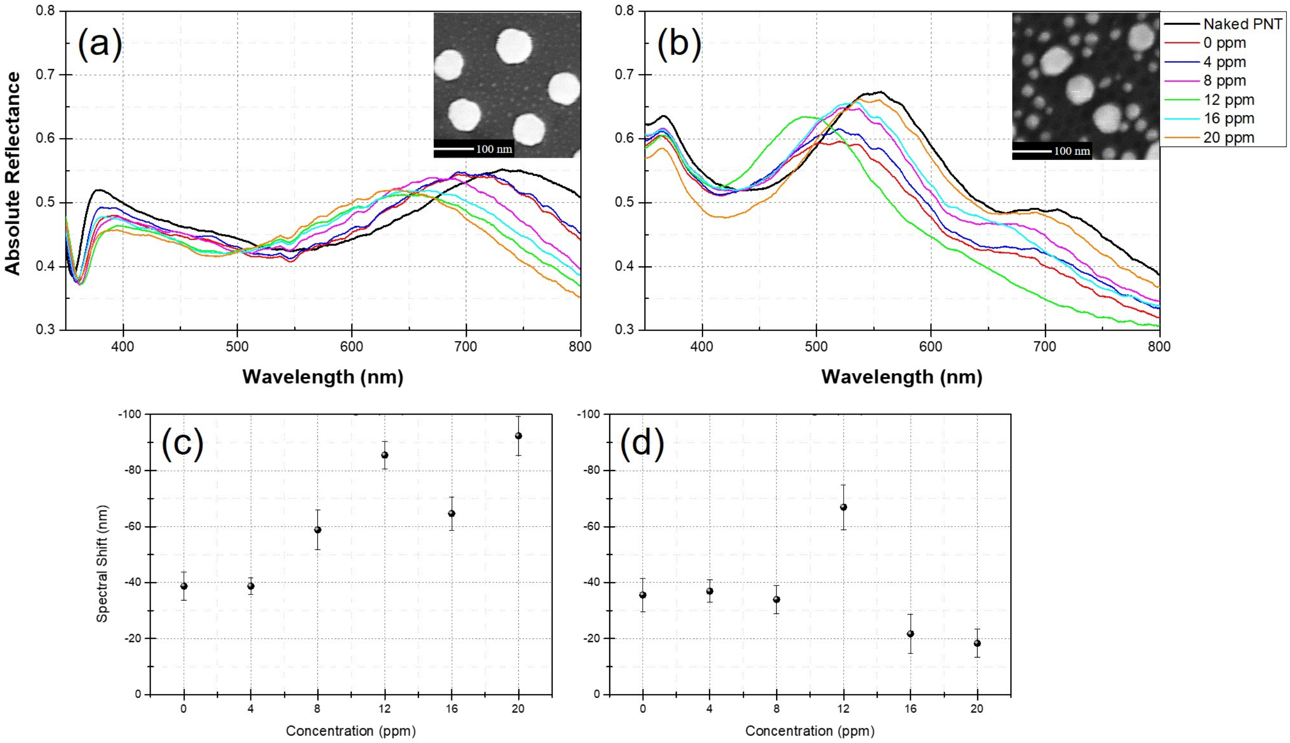

Figure 4.9: Optical reflectance spectroscopy (ORS) measurements of the naked plasmonic nanoparticle templates before and after the treatment with the various Pb_2SO_4 solutions for the (a) $500mJcm^{-2}$, 1 pulse and (b) $500mJcm^{-2}$, 6 pulses templates. With (c) and (d) showing the spectral positions of the primary LSPR reflectance peak after the evaporation of each of the lead solutions for the 1 and 6 pulses templates respectively. The associated SEM micrograph insets show the structure of the as fabricated, naked PNT.

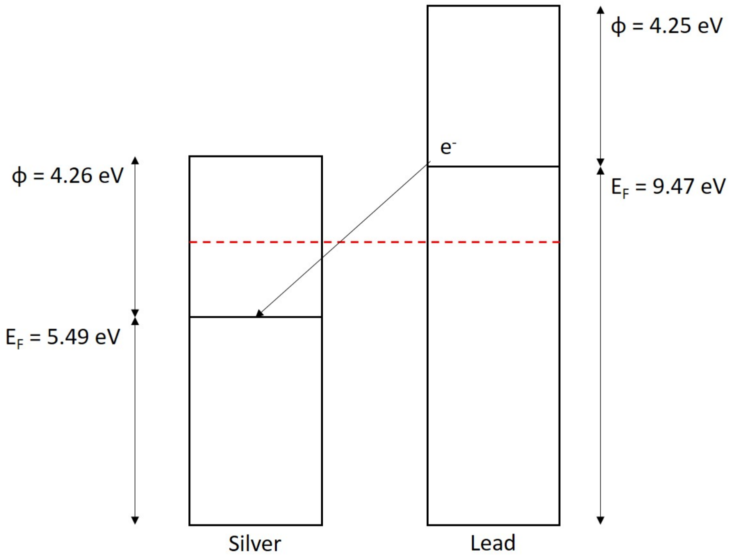

levels.jpg

Figure 4.10: Diagrammatic view of the Fermi Energy (EF) and work function () of silver (left) and lead (right). The Fermi energy of lead is significantly higher than the Fermi energy of silver. This would allow for electrons in the lead to transition to vacant higher energy states within silver. This would result in an increase in the number of electrons (oscillators) within the silver subsequently increasing the plasma frequency and blue-shifting the LSPR peak of silver.

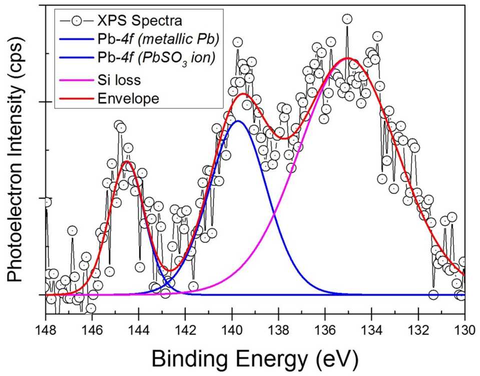

Figure 4.11: Example of the XPS spectra acquired to ascertain the surface composition of the PNTs, focused on the Pb-4f peak, from the $500mJcm^{-2}$ 1 pulse template exposed to the 12 ppm solution.

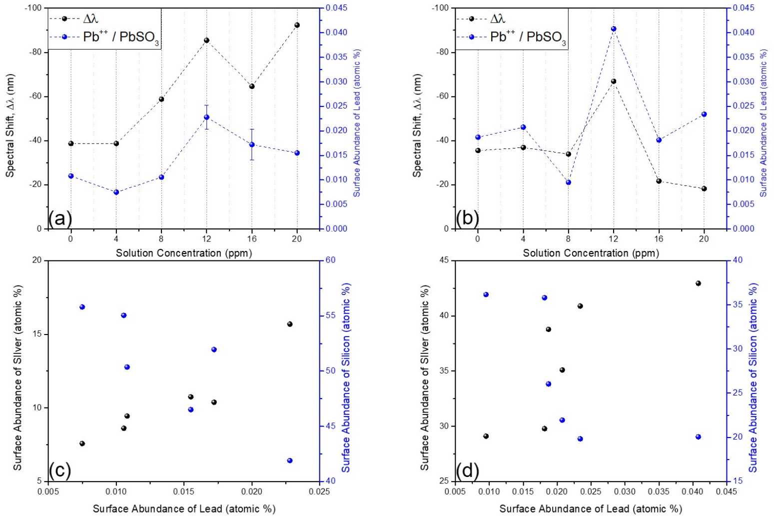

Figure 4.12: X-ray photoelectron spectroscopy analysis, where (a) and (b) show the link between the spectral shift and the surface abundance of lead, while (c) and (d) show the relationship between the surface abundance of lead to silicon and silver, for the $500mJcm^{-2}$ 1 pulse (*left*, (a and c)) and $500mJcm^{-2}$ 6 pulses (*right*, (b and d)) templates respectively.

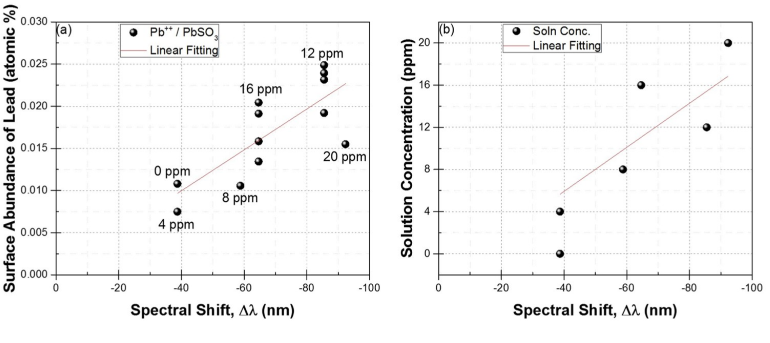

Figure 4.13: Calibration curves, relating the measured spectral shift to the: (a) surface abundance of lead, as Pb^{++} and $PbSO_3$ (atomic %); and (b) the original solution concentration (ppm).

Chapter 5

Plasmonic Nanoparticle Templates on a Polymer Substrate

5.1 Introduction

Periods of history are often described by the material that defines them. As such, it could be considered that we exist within the "*plastic age*". This can be seen by the extent to which we interact with plastics, or polymers, in our daily lives, from drink bottles to food packaging we are surrounded by polymers. Beyond that, the sheer volume of research undertaken worldwide involving polymers [159–164] proves their importance. Polymers are a highly versatile family of materials that can be utilised across an increasingly diverse range of applications due to their low cost; high availability; transparency; ease of used in large-scale processing; and their ability to adjust their properties to suit a given application; in addition to being flexible.

Flexible devices and technologies are becoming increasingly abundant in modern life, from flexible display screens and electronic paper too Disney MagicBands™ [165]. This has led to a much greater demand than ever before for flexible technologies using a wide range of different substrate materials [166]. Among the driving force for this increased interest, is the desirability of wearable devices and technology, especially for devices that can provide accurate, real time information *in situ* and on demand, such as wearable sensors and monitoring systems. The key milestone towards such devices, is the ability to fabricate the necessary nano- and microscale structures on a suitable substrate [167–169]. When selecting a flexible polymer substrate, a prime candidate for such a polymer is polyethylene terephthalate, or PET, thanks to its low cost and variety of readily available forms. Despite the many advantages of a polymeric substrate, polymers suffer from several disadvantages that makes the fabrication of highly specific structures increasingly difficult due to their sensitivity to both temperature and many common chemicals which leads to limited process compatibility.

Despite the extensive use of Raman spectroscopy throughout all aspects of the scientific community, the inherent weakness of Raman spectroscopy is the necessity for inelastic scattering events. This has led to extensive research into a methodology for increasing the intensity of the Raman signal. Since the discovery of an increase in the measured signal from a roughened silver electrode, Surface Enhanced Raman Spectroscopy or SERS [140–143], has become a tool that has led to Raman spectroscopy being able to detect single molecules. SERS makes use of plasmonic nanoparticle templates to enhance either the Raman scattered light, or the probing laser line and can significantly increase the signal to noise ratio of the measured signal by many orders of magnitude. Such surfaces are commercially available, on a rigid substrate. However, to date there does not exist a robust and flexible SERS surface, either within the literature or commercially.

Beyond the use of a polymer substrate as a route towards flexible sensors and potential wearable devices, is the possibility of using a flexible or elastic substrate to be able to mechanically *tune* the response of an existing plasmonic nanoparticle template through the alteration of the surface distribution and interparticle distance [170–176]. This approach offers one of the few available and reported routes towards an end user tuneable plasmonic system.

5.2 Results and Discussion

When using a known substrate, such as silicon, the laser annealing window, the bracket of laser fluence (energy density, $mJcm^{-2}$) and number of laser pulses that induce a transformation from a discontinuous thin metallic film into a metallic nanoparticle template, are well known and understood both experimentally and theoretically. Therefore, when this process is transplanted to an untested substrate, like a polymer, the first task is to identify this processing window. However, initially it was prudent to understand the extent to which the laser interacts would interact with the selected polymer. For this work, the polymer selected was polyethylene terephthalate, or PET, because of its wide range of industrial viable variants of PET and the ease with which a polymer like PET can be transplanted into large scale processes like roll-to-roll fabrication. Due to the absorption coefficient of PET ($\mu_\alpha = 1.00 \times 10^5$) at the processing wavelength (248 nm, from a KrF Excimer laser system). As seen in figure 6.1, there is clear transformation in the optical response of the PET, even when processed with exceptionally low laser fluences. The laser annealing has induced a transformation from the smooth, untreated PET to a distinct island, globule like structure post processing. This provides clear evidence that the absorption of the laser line causes the PET surface to melt and re-solidify. This suggests that when laser annealing a metallic silver film on a PET substrate, there would be a two-fold surface modification: the absorption in the metallic thin film producing a nanoparticle template; and the direct absorption in the PET substrate altering the PET surface, producing a significantly different surface morphology.

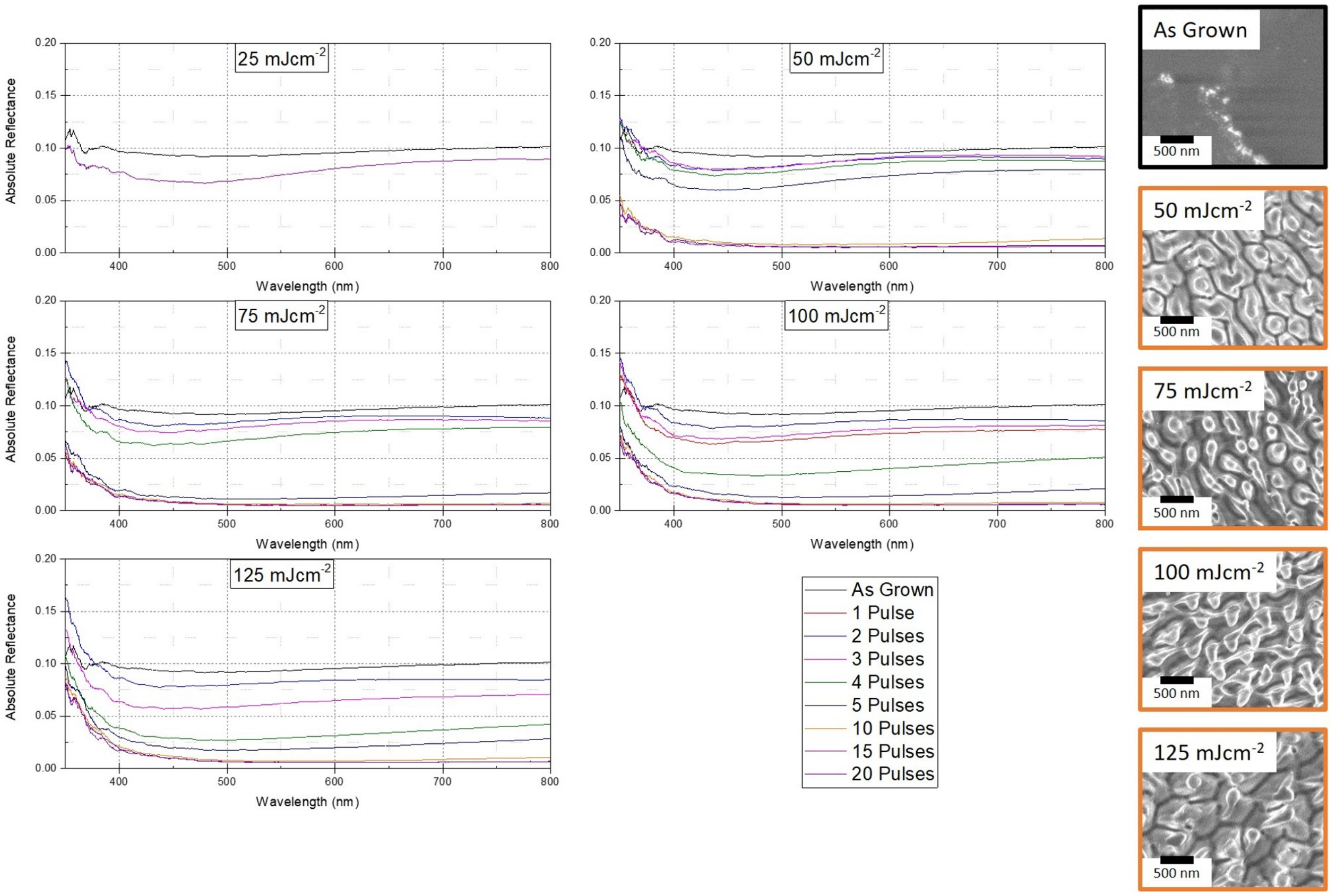

Figure 5.1: Calculated optical reflectance spectroscopy (ORS) absolute reflectance of the unprocessed and laser annealed areas of PET, for a range of fluences. The inset SEM micrographs show the surface structure of the processed areas where the coloured borders correlate to the plot colours.

When considering a PET / Ag sample structure, the absolute reflectance from even the as deposited silver thin film is significantly lower than that seen when using a silicon substrate, which can be attributed to the transparency of the PET substrate. The inherently low reflectance profile of a transparent material compared to a highly reflective material like silicon allows for the reduced reflectance. The silver film was deposited *via* radio frequency magnetron sputtering, in a high vacuum chamber (base pressure of $< 10^{-6} mbar$), from a round (3") Ag target (99.99% purity), in the presence of argon, Ar (99.999% purity), at a fixed flow rate of 4 standard cubic centimetres per minute (sccm) resulting in a working pressure of 5 mTorr. The power applied to the target was set to 40 W while the PET substrates was held on a carrier wafer rotating at 12 revolutions per minute (rpm) to ensure a uniform deposition, to a nominal thickness of 10 nm, resulting in the formation of a thin discontinuous film, with a reflectance profile significantly lower than that of bulk silver.

When considering the laser annealed silver thin film, figure 6.2, we can see that even in the case of low fluence and minimal laser pulses, in particular the $25mJcm^{-2}1pulse$ and $50mJcm^{-2}1pulse$ areas, there is the appearance of a subtle reflectance peak that suggest that a nanoparticle template has been produced. The collaborating SEM micrograms prove that there has been a transformation from a thin film to a nanoparticle template. As seen in figure 6.2. These nanoparticle templates were produced at a significantly lower processing window than that used when working on a silicon substrate (above $200mJcm^{-2}$.As seen, a fluence above $150mJcm^{-2}$ causes the complete ablation of the silver thin film on PET, while of silicon this same fluence is insufficient to produce a nanoparticle template. Due to the inherent interaction of the laser line with the PET substrate, we can conclude that the absorption of the laser in the substrate hinders the production of a plasmonic nanoparticle template.

Additionally, the nanoparticle templates produced on PET are of a much lower quality than those produced on a silicon substrate, based on the low surface coverage of the nanoparticles and the associated large inter-particle distance. The highly disperse structure of the template, in parallel with the transparent nature of the PET, affects the optical profile of the template by minimising the magnitude of the reflectivity as well as shifting the spectral position of any LSPR peak that may exist.

The dramatic difference between the structure of the plasmonic nanoparticle templates fabricated on a PET substrate and a template produced on a silicon substrate, could be explained by considering the discrepancies of the thermal conductivity; specific heat capacity; and thermal bulk of these two substrates. Consequently, it can be theorised that a silicon substrate is better able to deal with the energy dissipation necessary during laser annealing, in both a LISA and MONA-LISA process.

5.2.1 Interlayer Materials

To address this discrepancy of thermal properties and improve the ability of a PET substrate to support the laser fabrication of a nanoparticle template, it was suggested that the inclusion of an interlayer or '*barrier*' material, could be used to modify the properties of the substrate, allowing for a more successful laser annealing process and the fabrication of a higher quality nanoparticle templates. In addition to the modification of the thermal properties, these interlayer materials

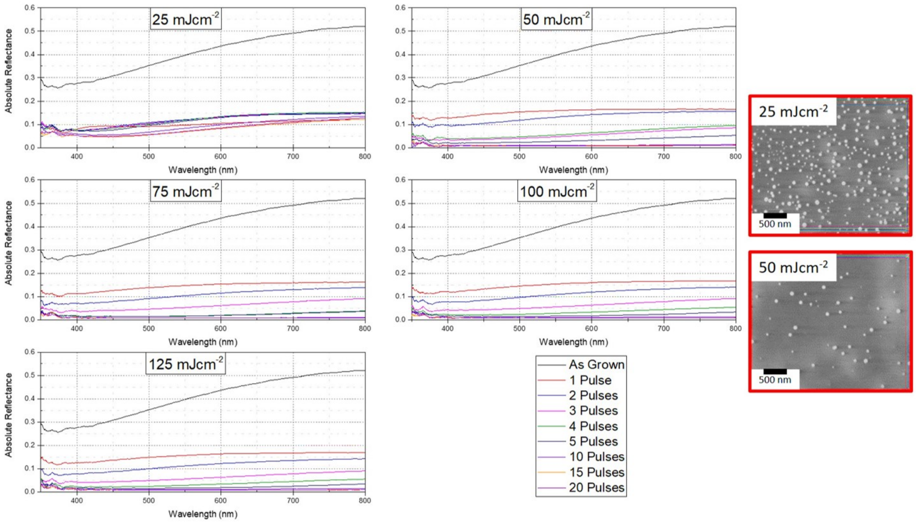

Figure 5.2: Calculated optical reflectance spectroscopy (ORS) absolute reflectance of the unprocessed and laser annealed areas of the thin silver film on a PET substrate, for a range of fluences. The inset SEM micrographs show the surface structure of the processed areas where the coloured borders correlate to the plot colours.

could be used as an active functional layer, essential for the operation of a given device, such as a charge transport layer or a dielectric / conducting layer.

Four specific interlayer materials were identified for investigation, due to the range of physical, thermal and electrical properties they span, as seen in table 6.1. As well as providing a wide range of properties for instigation, these materials are all established within their relevant fields, namely: silicon dioxide (SiO_2) is a classic material used in electronics; yttrium oxide (Y_2O_3) is a highly versatile dielectric material; and indium-tin oxide (ITO) and aluminium-doped zinc oxide (AZO) are used extensively as transparent conductors. All of these materials were deposited as thin films using room temperature RF magnetron sputtering in a high vacuum chamber (base pressure of $< 10^{-6} mbar$), from round (3") targets, in the presence of argon (99.999% purity) and in the specific cases oxygen (99.999% purity), at a fixed flow rates to produce working pressure of 3 - 5 mTorr (depending on the material). Each of these interlayer materials were deposited onto a PET substrate to a range of thicknesses. This allowed for an investigation into both the influence each of the interlayer materials has on the laser annealing process as well as the identifying the influence of interlayer thickness.

Materials	Thermal Conductivity κ $Wm^{-1}K^{-1}$	Specific Heat Capacity C $Jkg^{-1}K^{-1}$	Band Gap E_G eV	Resistivity ρ Ωm	Absorption Coefficient @ 248 nm μ_a cm^{-1}	Dielectric Constant
Substrates						
Si	130	700	1.11	0.1 - 60	5.43×10^{-5}	11.9
PET	0.15 - 0.24	1000	3.87	1.00×10^{21}	1.00×10^{5}	3.4
Air (O_2)	0.0257	1005	5.7	$1.3 \times 10^{16} - 3.3 \times 1{-}^{16}$		1.00059
Interlayer Materials						
SiO_2	1.3 - 1.5	680 - 730	9.3	$1.00 \times 10^{15} - 1.00 \times 10^{19}$	700	3.9
Y_2O_3	13.7	453.5	5.6	1.00×10^{7}	4.00×10^{3}	14 - 18
ITO	20	490	3.5	3.5×10^{-6}	1.07×10^{7}	
AZO	20	494	3.5	1.8×10^{-5}	7.0×10^{6}	

Table 5.1: Table showing the diverse range of properties, both thermal and electrical, of the interlayer (*barrier*), materials. This table allows for the identification of the key physical property or properties necessary for a substrate / interlayer composite to facilitate its use as a laser annealing substrate. Although air does not act as a substrate, when laser annealing in an ambient environment, the air acts as vital thermal conductor during the annealing process in a similar way to the substrate and should therefore be considered in the same context.

Each of these interlayer materials produced a significant change to the optical profile of the resultant nanoparticle templates, but further discussion will be focused on the 100 nm thicknesses of each interlayer material, as this interlayer thicknesses exhibited the greatest influence on the nanoparticle templates. As shown in figure 6.3, the inclusion of the interlayer material induced, in cases where there was not total ablation, the formation of a *bed sheet* like structure. The associated SEM micrograms in figure 6.3, show an obvious creasing and wrinkling of the interlayer / silver composite, which can most clearly be seen in the case of the PET / SiO_2 / Ag sample. Across all the investigated interlayer thicknesses, but most easily observed with an interlayer thickness of 100 nm, it is evident that the ablation threshold, the laser fluence or number of treatment pulses required before the silver thin film is fully ablated has been lowered below that seen without the interlayer material. Additionally, in some cases the interlayer material was ejected or delaminated from the substrate, as evidenced by the presence of large areas of exposed PET, seen as dark areas in the SEM micrographs.

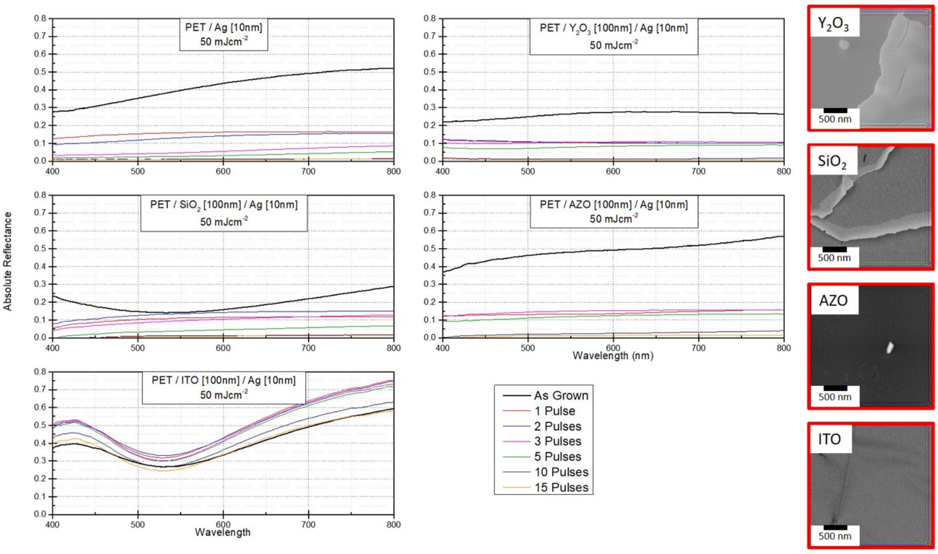

Figure 5.3: SEM micrographs and associated Optical Reflectance Spectroscopy (ORS) spectra of a sample series demonstrating the influence of the different interlayer materials on the formation of laser fabricated plasmonic nanoparticle templates for a single laser energy and an identical pulse progression. Each of the barrier samples shares a structure (PET / Barrier material [100nm] / silver film [10nm]) to understand the effect of the individual barrier layers. Additionally, the PET / silver film [10nm] sample is included for comparison. The inset SEM micrographs show the surface structure of the processed areas where the coloured borders correlate to the plot colours.

In addition to the experimental investigation, a computational investigation into the absorption of the laser line in the PET substrate, the silicon dioxide interlayer and the silver thin film. This study was conducted *via* 3-dimensional finite - difference time - domain (3D FDTD) method. For this investigation, the silica interlayer material was selected for simulation due to the optical response from the experimental PET / silica / silver sample showing the highest potential as an effective interlayer to facilitate the laser fabrication of a nanoparticle template on a PET substrate.

These computational simulations, as seen in figure 6.4, show that at either of the possible processing wavelengths (248 nm from KrF and 193 nm for ArF), the absorption of the laser line in the PET substrate and the silica interlayer are consistent at 50% (39% – 54%) and 3% (0% – 5%) respectively, across all of the simulated silica thicknesses. When considering the absorption within the silver film however, at the three experimental silica thicknesses produced: 50 nm; 100 nm; and 150 nm, we can see that at 193 nm the achieved absorption is at a relative maximum (29% – 35%) while with 248 nm the situation is reversed as the absorption can be seen reach a minimum (7% – 11%). From this, it was concluded that the low absorption in the silver film and the high absorption in the PET substrate could easily lead to the ablation and delamination observed. The discrepancy in the absorption and the resultant thermal heating could lead to this effect by exploiting the low interface adhesion as a mechanism to dissipate the energy gained by the substrate.

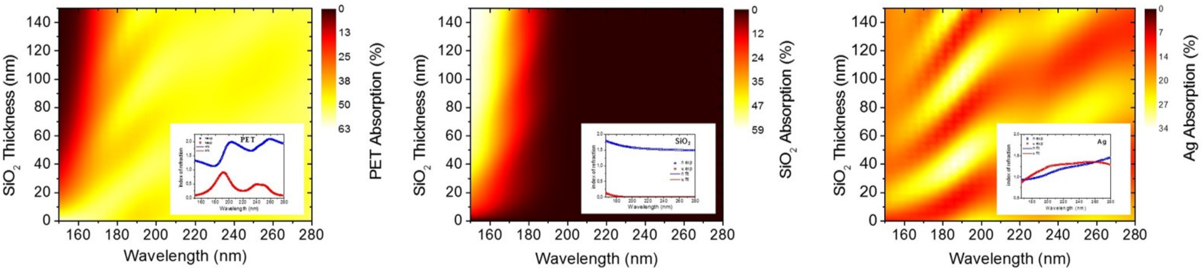

Figure 5.4: The absorption and inset the dielectric function of the PET substrate, silica interlayer and the silver thin film.

5.2.2 Interface Modification

The modification of the processing window is inherent when using a different substrate, as evidenced in figure 6.2. However, the significant increased probability of ablation; the delamination of the interlayer material; and the wrinkled, creased, *bed-sheet* like structure can be clearly attributed to the presence of the interlayers, seen in figure 6.3. It was suggested that in addition to a modification of the properties of the substrate, the inclusion of the interlayer material alters the layer adhesion within the sample, which would attribute to the ease of delamination seen during laser annealing. This low layer adhesion would simultaneously hamper our ability to fabricate a nanoparticle template. Overcoming this phenomenon represents a clear milestone towards the laser fabrication of a plasmonic nanoparticle template, *via* laser annealing, on a PET substrate.

To counter this lowering of layer adhesion, there exist two primary routes towards addressing this layer adhesion, through a physical or chemical process. While a chemical process has several advantages and would be highly successful in increase the adhesion at the PET / interlayer, by necessity, the procedure would need to be unique for each of the interlayer materials used. This significantly complicates the process and forces the inclusion of several additional variables on top of the interlayer thickness and material. Consequently, it was concluded that a physical process would be beneficial, despite the lower adhesion possible. A physical process was selected as it would allow for a single process to be used with all the interlayer materials to increase the interface adhesion. This would allow for the direct identification of the layer adhesion on the laser annealing process. To increase the layer adhesion, the PET surface was roughened prior to the deposition of the interlayer material, *via* plasma etching. This was performed with a Tegal Plasmaline 415 Asher plasma asher, using 2% oxygen in argon (2%O_2 in Ar) gas to produce a plasma with 100 W of applied power at a working pressure of 15 mTorr. The PET substrate was treated for one hour (60 minutes) to modify the surface roughness, as shown in figure 6.5. From figure 6.5, we can see that there is a significant modification to the PET surface, where the transmission of the PET substrate fell from 97% to 65%. The modified substrate, henceforth described as plasma-etched PET or PE.PET, was then deposited with the established interlayer barrier materials, using the RF magnetron sputter deposition technique discussed previously.

Figure 5.5: Image showing the difference between the untreated (*left*) and plasma etched (*right*) PET with an increased surface roughness prior to the deposition of a barrier material.

As the surface of the PE.PET has inherently been modified, it is conceivable that the magnitude of the surface adsorption of gases will be dramatically increase. Due to this, before the deposition of the interlayer materials, the PE.PET substrate was held under vacuum within the deposition chamber for 30 minutes to allow for the substrate to out-gassing and to ensure the quality of the interface produced. This technique allowed for increased layer adhesion demonstrated by the much lower sample damage form routine handling and the increased sample lifetime when compared to the untreated PET substrate. While it is of worth to note that the extended lifetime and improved sample stability of the PE.PET samples, they are still significantly more fragile samples than those produced on a silicon substrate. As it was previously identified that the interlayer materials produced the greatest influence on the production of a nanoparticle template at a thickness of 100 nm, all the barrier materials were deposited onto the PE.PET substrate to this thickness before being topped with a 10 nm discontinuous film of silver and subsequently laser processed.

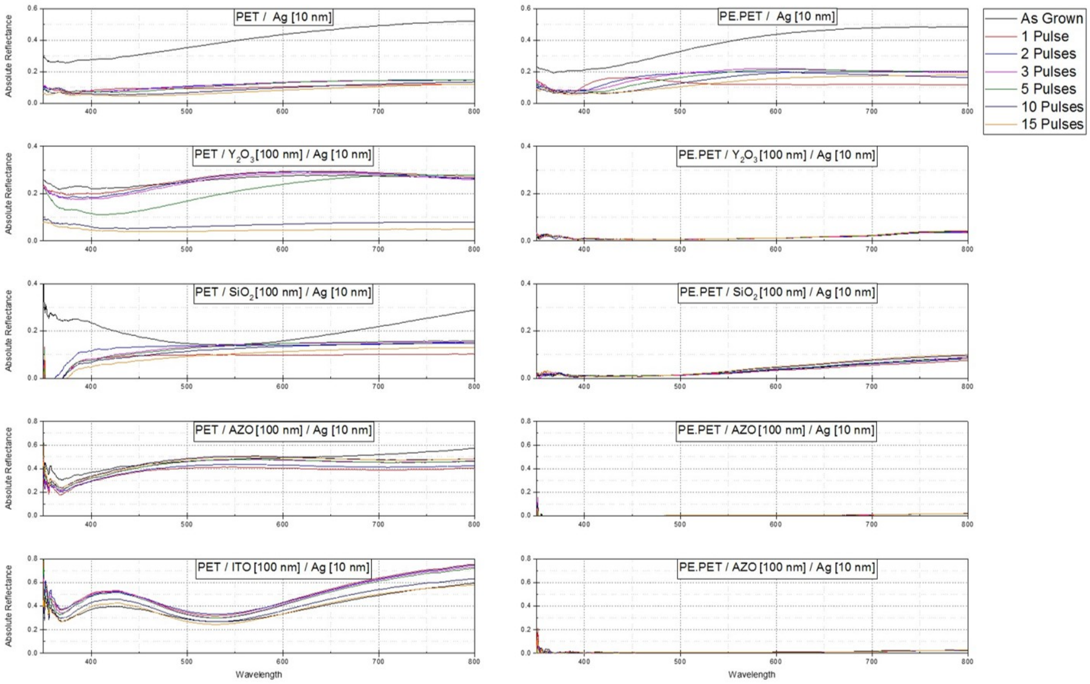

Figure 5.6: The optical reflectance spectroscopy (ORS) calculated absolute reflectance for the interlayer materials deposited onto both the untreated and plasma treated PET treated with a number of laser pulses at a laser fluence of $25mJcm^{-2}$. Where the PET / Ag and PE.PET / Ag are included for comparison.

As shown in figure 6.6, we can see that for the case of both the PE.PET / silver (no interlayer) and PE.PET / silica / silver, the modification of the PET surface had a significant improvement on the optical profile of the laser fabricated nanostructure. The PE.PET /silver sample demonstrate a clear LSPR peak when treated with low fluences and low numbers of laser pulses (most evidently when processed with one laser pulse at $25mJcm^{-2}$). Beyond this, the response seen from subsequent laser pulses suggest that additional laser pulses allow for the modification of the optical response of the nanoparticle template, comparable with the behaviour achieved on a silicon substrate. Additionally, in the case of the PE.PET / silica / silver, all the investigated laser pulses appear to demonstrate a bimodal optical response, with two clear peaks, where again successive laser pulses onto the sample show some modification to the optical response.

In the case of the other interlayer materials, but most prominent in the case of the ITO interlayer, the optical response of the laser processed areas have been quenched, with a reflectance below 1% for all laser fluences and pulses used. Further to this, from the direct comparison between the plasma treated and untreated PET substrate, we can conclude that our ability to successfully fabricate a plasmonic nanoparticle template on a polymeric substrate has been improved by the combination of increasing the surface adhesion and modification of the substrate's properties. This improvement can be attributed to a combination of the increased thermal bulk of the sample due to the inclusion of the interlayer as well as the enhanced layer adhesion due to the increased surface roughness from the plasma treatment of the substrate. The phenomenon of the low reflectance in all cases of the roughened PET substrate can be attributed to the base optical response of the substrate at two stages. Initially, the untreated PET substrate is inherently transparent and as such has a very low optical reflectance, with a reflectivity of 4% - 6%, while when the substrate is plasma etched, the PE.PET which has caused an increased to the surface roughness, significantly increasing scattering and further reducing the optical spectral reflectance. These two factors, in combination with the low ablation limit of the interlayer / silver composite results in an overall low reflectance profile of the laser annealed areas.

5.2.3 SERS Effect on Flexible Substrate

This low reflectance from the laser annealed areas of both the PET / interlayer / silver and PE.PET / interlayer / silver samples, makes the traditional reflectance spectroscopy methodology for characterising and identifying the presence of the plasmonic nanoparticle template unreliable. Consequently, another method for the identification of an additional route towards this. As such, it was concluded that a Raman microscope (Thermo Scientific DXR2) could be used to simultaneously probe the ability of these laser fabricated plasmonic nanoparticle templates to act as a surface enhanced Raman spectroscopy (SERS) surface, while also allowing for the identification of a plasmonic structure and to quantify their spectral position. The Raman spectra were measured with a 532 nm probe wavelength at 0.5 mW in a $100\mu m$ spot size, using a spectroscopic detector with a maximum spectral range of $100-3500cm^{-1}$operating at $16-27^{O}C$.

To this end, an establish Raman active compound, namely the dye rhodamine 110 chloride (Rh110) (Sigma Aldrich, $\geq 88\%$ purity, $\lambda_{max} = 496nm$), was selected due to the corresponding low fluorescence associated with the pumping wavelength of the Raman microscope used (532 nm). The rhodamine dye was produced at three stock solutions at specific concentrations ($40mM$, $40\mu M$ and $40nM$) in ethanol that could be used to assess if there was any SERS enhancement, while also proving a route towards identifying the nanoparticle template that results in the greatest enhancement. This would allow for a single measurement to provide evidence that a plasmonic nanostructure exists with a LSPR peak that lies near the pumping laser wavelength of the Raman microscope while simultaneously assessing the quality of a potential SERS surface. Two samples were selected for assessment with a Raman microscope: the PE.PET / silver [10 nm]; and the PE.PET / silica [100 nm] / silver [10 nm] samples. These samples were selected based on their optical reflectance spectroscopy (ORS) measurements of these two samples demonstrated the clearest indication of a LSPR peak that could allow for a SRES enhancement.

Before any SERS behaviour can be characterised, the inherent detection limit of the Raman microscope must be established. To identify the minimum concentration detectable and to align with the standard concentrations used for SERS measurements, the stock solutions of the Rh110 dye were assessed on the as deposited, 10 nm thin silver film of 3 substrates: plasma etched PET; plasma etched PET / silica [100 nm] composite; and a silicon wafer, as a reference and control sample. Each concentration was evaporated on the as deposited silver film as a microliter ($1\mu L$) droplet and allowed to evaporate under ambient conditions. These Raman spectra can be seen in figure 6.7.

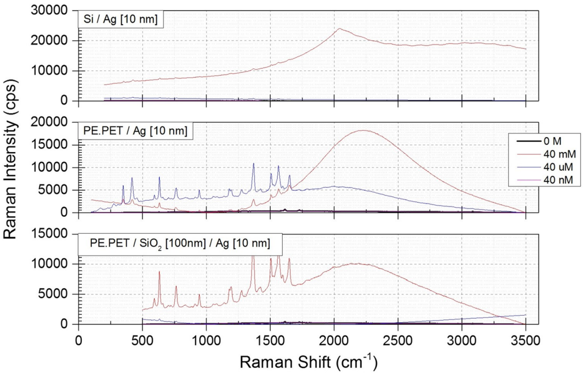

Figure 5.7: Raman spectra from the three stock solutions, 40 mM (red), 40 µM (blue) and 40 nm (pink) of Rh110 dye, as well as the spectra from the as deposited silver thin film (black). Three samples were investigated, Si/Ag, $PE.PET/Ag$ and $PE.PET/SiO_2/Ag$. As can be seen across all samples, the milli-molar (mM) concentration demonstrates a large fluorescence peak despite the selection of a dye with a minimal fluorescence at the laser line of the Raman microscope.

The detection limit of the Raman system, shown by the concentration that displays a clear Raman signal with a minimum number of counts, can be seen to be the 40 nM solution across all three substrates, but most clearly on the PE.PET / silica / silver sample. While the silicon sample exhibits significantly higher counts in all cases than both PET samples, this is to be expected, as the silicon has a significantly higher visible optical reflectance, particularly at the probing laser wavelength (532 nm). Subsequently, the selected laser annealed areas on all three of the tested substrate samples (PE.PET / silver, PE.PET / silica / silver and Si / silver) were exposed to the Rh110 solution as described previously ($1\mu L$ droplets placed on the selected areas and allowed to evaporate under ambient conditions) using the 40 nM concentration, as this concentration most closely resembles the concentrations used for the testing of a SERS surface seen in literature. From each sample, the laser annealed areas were selected based on their optical response and how likely is was that this LSPR peak would allow for a SERS enhancement. As such, the $500mJcm^{-2}$, $25mJcm^{-2}$ and $50mJcm^{-2}$ laser processing fluences were selected for the Si/Ag, $PE.PET/Ag$ and $PE.PET/SiO_2/Ag$ samples respectively, where the measured Raman spectra can be seen in figure 6.8.

The Raman signal from both PE.PET substrates across all the laser annealed areas exhibit almost identical spectra, where the identifiable Raman peaks that can be seen can be attributed to the PET substrate and not the rhodamine dye. For the case of the silica interlayer and the case of the PE.PET / Ag sample treated with 1 pulse, the distinct, broad double peaks around $1400cm^{-1}$ and $1500cm^{-1}$, are indicative of carbon *d*- and *g*- bands, which is indicative of sample burning. The evidence of sample burning (the burning of the Rh110 dye) provides a significant indication that the LSPR of these nanoparticle templates is centred close to the laser wavelength (532 nm) and therefore enhancing the probing laser, leading to this burning, rather than enhancing the Raman signal. The lack of any SERS enhancement could be attributed to the spectral position of the LSPR peak not corresponding to the Raman peaks of the dye, but the evidence of burning suggest that the LSPR peak must lie close to the laser line and consequently should be providing some signal enhancement. Alternatively, due to the inherent low reflectivity and therefore the low measurable signal from the PE.PET samples and the low concentration used, it is possible that the signal is sufficiently low so that it is below the detection limit of the Raman microscope.

To establish which of these effects led to the lack of signal enhancement, a second experimental test was designed, where a second sample series was produced and processed identically to the PE.PET / silver and PE.PET / silica / silver samples described previously. However, this time the samples were exposed to the $40\mu M$ concentration before measuring with the Raman Microscope, to identify if the apparent lack of enhancement could be attributed to the low measurable signal rather than the lack of any enhancement. These spectra can be seen in figure 6.9. It can be clearly seen that for the case of the PE.PET / silver sample, that there are

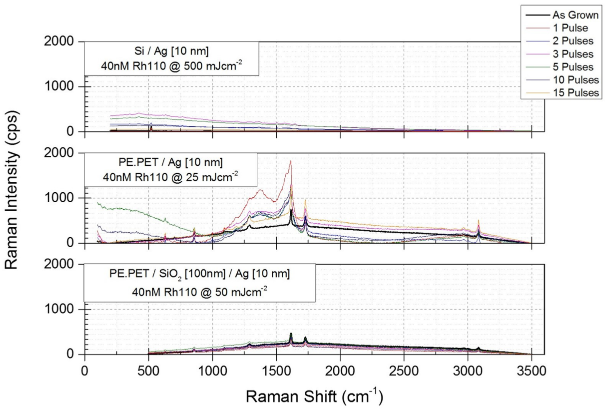

Figure 5.8: Raman spectra from the 40 nM solution of Rh110 dye, as well as the spectra from the as deposited silver thin film (black). The selected laser fluences investigated were selected due to the spectral position of the expected LSPR peak position. Three samples were investigated, Si/Ag, $PE.PET/Ag$ and $PE.PET/SiO_2/Ag$. The dominant peaks between $1400-1500cm^{-1}$ are characteristic of the d- and g- bands of carbon, indicative of burning.

a number of laser processed areas which demonstrate an enhancement to the detected signal, despite no obvious optical fingerprint of a nanoparticle templates seen from the ORS spectra. This enhancement can be seen in the Raman signal allows for the identification of multiple Rh110 specific Raman lines, as well as increasing the measurable signal by orders of magnitude when compared to the signal of the same concentration of the as deposited silver film (black line in figure 6.9. In contrast, when we consider the PE.PET / silica / silver sample, we can see that of all the assessed laser annealed areas, only one demonstrate an enhancement of the Raman signal, namely the $50mJcm^{-2}$, 2 pulses template. This template is not only the only template to exhibit a SERS enhancement, but also the template across both PE.PET samples that show the cleanest enhancement with the most obvious Raman peaks.

From the measure Raman spectra, the two laser processing conditions, one for each substrate, identified that resulted in a significant signal enhancement when compared to the same concentration applied to the as deposited silver film. As can be seen in figure 6.10, both the $PE.PET/Ag$ and the $PE.PET/SiO_2/Ag$ sample demonstrate an obvious enhancement when compared to the same concentration evaporated on the unprocessed silver film, caused by the laser fabrication of a plasmonic nanoparticle template on the PET substrate. Further to this, the greatest enhancement can be seen from the PE.PET / silica / silver sample, where the magnitude of enhancement can be seen to allow for the reliable identification of the compound under investigation by allowing for the clear distinction between the Rh100 specific Raman lines and the Raman signal from the PET substrate, showing a SERS enhancement factor of $G = 45$. As

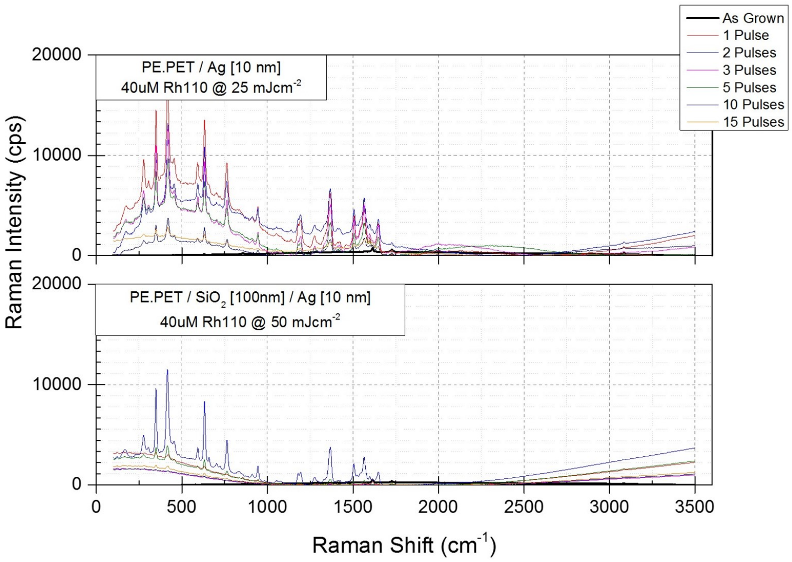

Figure 5.9: Raman spectra from a solution of $40\mu M$ Rh110 dye in ethanol evaporated onto the laser processed areas from two PE.PET substrate samples. The highest signal can be identified from each sample as $25mJcm^{-2}$, 1 pulse for the $PE.PET/Ag$ sample and $50mJcm^{-2}$, 2 pulses for the $PE.PET/SiO_2/Ag$ sample. Both of these laser treated areas demonstrate an enhanced signal, with clear Rh110 specific Raman peaks, that cannot be seen when the identical solution was evaporated onto the untreated silver film.

such this measurement, simultaneously provides evidence that a plasmonic nanoparticle templates have been successful laser fabricated on a flexible and transparent polymer substrate, while also allowing for confirmation that such a template can be used as a SERS substrate for the enhancement of the Raman signal of a given compound.

5.3 Conclusions

The ability to reliably and with control, produce a nanostructure on a flexible polymer substrate represent a clear and distinct barrier that needs to be overcome before such substrates can become more widely utilised, and this is no less the case for the field of plasmonics. Therefore, the development of a methodology for the laser fabrication of a plasmonic nanoparticle template on a PET substrate is necessary to develop a flexible polymer SERS surface as well as other applications.

The transfer of the laser annealing process from a rigid silicon substrate to the PET polymer, introduce a series of difficulties, including the significant decrease of the available processing window and additional interactions of the laser line with the substrate. This equates to a

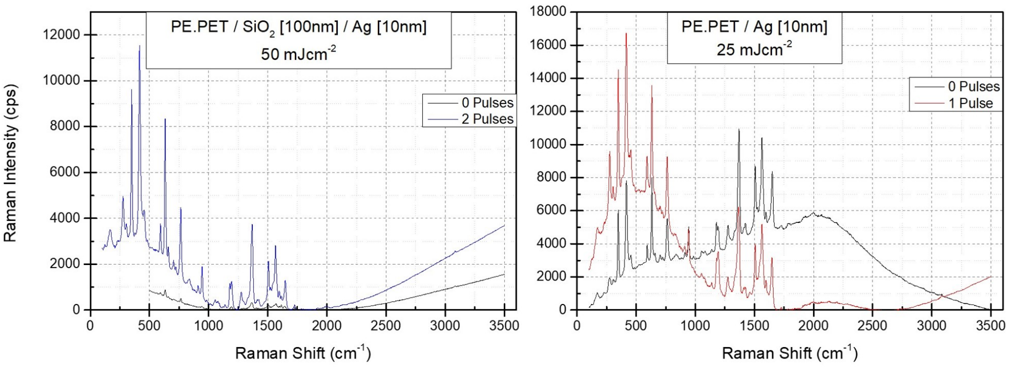

Figure 5.10: Raman spectra of Rhodamine 110 chloride on two different plasmonic nanoparticle templates, one fabricated in a $PE.PET/SiO_2(100nm)/Ag(10nm)$ structure processed with 0 and 2 pulses of $50mJcm^{-2}$ (left) and one fabricated in a $PE.PET/Ag(10nm)$ structure processed with 0 and 1 pulses of $25mJcm^{-2}$ (right). Spectra showing the variation of Raman signal caused by the Ag nanostructuring caused by the laser annealing process.

dramatic loss of control in the fabrication and the nanoparticle templates that were produced, had an exceptionally low optical reflectance and lacked a clear LSPR peak. Resulting in the direct transference of the laser annealing process onto a polymer substrate not being possible. However, this is not a complete road block towards the use of such a substrate.

The thermal mass, specific heat capacity and the thermal conductivity of PET is notably lower than that of silicon, which could account for the difficultly of producing a nanoparticle template. To counter this, an interlayer material could be used to counteract this discrepancy of the properties. The addition of an interlayer or barrier material introduced another series of challenges, but primarily the remarkable ease of delamination during the laser annealing process and producing the wrinkling and creasing of the interlayer / silver film complex without any modification of adjustment of the processing window. It can be concluded that the thermal and electrical properties of the substrate and sample cannot be used exclusively to predetermine the success or failure of the laser annealing process.

Therefore, in addition to the addition of an interlayer, it was clear that a method for increasing the layer adhesion, by increasing the surface roughness of the PET substrate prior to the deposition of the interlayer, allow for a significant decrease of the observed delamination. However, and more vitally, the combination of increase interface strength and the presence of a barrier material allow for both production and modification of a plasmonic nanoparticle template through laser annealing, allowing for the use of a polymer substrate to be used as a leaser annealing substrate. Beyond facilitating the production and alteration of a nanoparticle template, the combination of an interlayer material and increased interface strength, enabled the plasmonic nanoparticle templates to be used as an effective surface enhanced Raman spectroscopy substrate, allowing for the enhancement of the measurable signal from the a Raman active, namely the dye rhodamine 11o chloride, by 4 orders of magnitude, allowing for the clear identification of both the dye specific and substrate specific Raman lines that was impossible without the presence of the laser fabricated nanoparticle templates.

Chapter 6

Plasmonic Nanoparticle Templates on a Polymer Substrate

6.1 Introduction

Periods of history are often described by the material that defines them. As such, it could be considered that we exist within the "*plastic age*". This can be seen by the extent to which we interact with plastics, or polymers, in our daily lives, from drink bottles to food packaging we are surrounded by polymers. Beyond that, the sheer volume of research undertaken worldwide involving polymers [159–164] proves their importance. Polymers are a highly versatile family of materials that can be utilised across an increasingly diverse range of applications due to their low cost; high availability; transparency; ease of used in large-scale processing; and their ability to adjust their properties to suit a given application; in addition to being flexible.

Flexible devices and technologies are becoming increasingly abundant in modern life, from flexible display screens and electronic paper too Disney MagicBands™ [165]. This has led to a much greater demand than ever before for flexible technologies using a wide range of different substrate materials [166]. Among the driving force for this increased interest, is the desirability of wearable devices and technology, especially for devices that can provide accurate, real time information *in situ* and on demand, such as wearable sensors and monitoring systems. The key milestone towards such devices, is the ability to fabricate the necessary nano- and microscale structures on a suitable substrate [167–169]. When selecting a flexible polymer substrate, a prime candidate for such a polymer is polyethylene terephthalate, or PET, thanks to its low cost and variety of readily available forms. Despite the many advantages of a polymeric substrate, polymers suffer from several disadvantages that makes the fabrication of highly specific structures increasingly difficult due to their sensitivity to both temperature and many common chemicals which leads to limited process compatibility.

Despite the extensive use of Raman spectroscopy throughout all aspects of the scientific community, the inherent weakness of Raman spectroscopy is the necessity for inelastic scattering events. This has led to extensive research into a methodology for increasing the intensity of the Raman signal. Since the discovery of an increase in the measured signal from a roughened silver electrode, Surface Enhanced Raman Spectroscopy or SERS [140–143], has become a tool that has led to Raman spectroscopy being able to detect single molecules. SERS makes use of plasmonic nanoparticle templates to enhance either the Raman scattered light, or the probing laser line and can significantly increase the signal to noise ratio of the measured signal by many orders of magnitude. Such surfaces are commercially available, on a rigid substrate. However, to date there does not exist a robust and flexible SERS surface, either within the literature or commercially.

Beyond the use of a polymer substrate as a route towards flexible sensors and potential wearable devices, is the possibility of using a flexible or elastic substrate to be able to mechanically *tune* the response of an existing plasmonic nanoparticle template through the alteration of the surface distribution and interparticle distance [170–176]. This approach offers one of the few available and reported routes towards an end user tuneable plasmonic system.

6.2 Results and Discussion

When using a known substrate, such as silicon, the laser annealing window, the bracket of laser fluence (energy density, $mJcm^{-2}$) and number of laser pulses that induce a transformation from a discontinuous thin metallic film into a metallic nanoparticle template, are well known and understood both experimentally and theoretically. Therefore, when this process is transplanted to an untested substrate, like a polymer, the first task is to identify this processing window. However, initially it was prudent to understand the extent to which the laser interacts would interact with the selected polymer. For this work, the polymer selected was polyethylene terephthalate, or PET, because of its wide range of industrial viable variants of PET and the ease with which a polymer like PET can be transplanted into large scale processes like roll-to-roll fabrication. Due to the absorption coefficient of PET ($\mu_\alpha = 1.00 \times 10^5$) at the processing wavelength (248 nm, from a KrF Excimer laser system). As seen in figure 6.1, there is clear transformation in the optical response of the PET, even when processed with exceptionally low laser fluences. The laser annealing has induced a transformation from the smooth, untreated PET to a distinct island, globule like structure post processing. This provides clear evidence that the absorption of the laser line causes the PET surface to melt and re-solidify. This suggests that when laser annealing a metallic silver film on a PET substrate, there would be a two-fold surface modification: the absorption in the metallic thin film producing a nanoparticle template; and the direct absorption in the PET substrate altering the PET surface, producing a significantly different surface morphology.

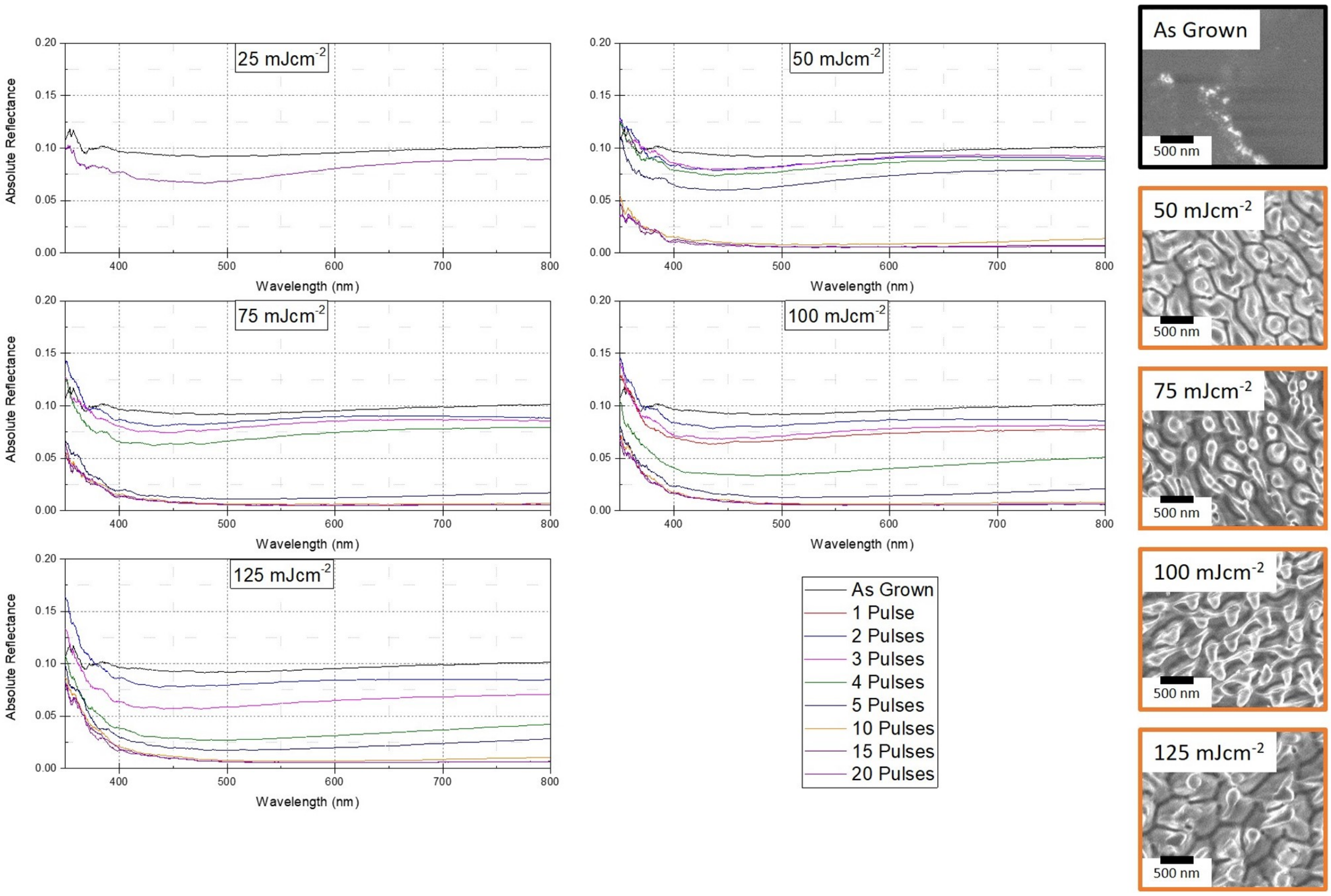

Figure 6.1: Calculated optical reflectance spectroscopy (ORS) absolute reflectance of the unprocessed and laser annealed areas of PET, for a range of fluences. The inset SEM micrographs show the surface structure of the processed areas where the coloured borders correlate to the plot colours.

When considering a PET / Ag sample structure, the absolute reflectance from even the as deposited silver thin film is significantly lower than that seen when using a silicon substrate, which can be attributed to the transparency of the PET substrate. The inherently low reflectance profile of a transparent material compared to a highly reflective material like silicon allows for the reduced reflectance. The silver film was deposited *via* radio frequency magnetron sputtering, in a high vacuum chamber (base pressure of $< 10^{-6} mbar$), from a round (3") Ag target (99.99% purity), in the presence of argon, Ar (99.999% purity), at a fixed flow rate of 4 standard cubic centimetres per minute (sccm) resulting in a working pressure of 5 mTorr. The power applied to the target was set to 40 W while the PET substrates was held on a carrier wafer rotating at 12 revolutions per minute (rpm) to ensure a uniform deposition, to a nominal thickness of 10 nm, resulting in the formation of a thin discontinuous film, with a reflectance profile significantly lower than that of bulk silver.

When considering the laser annealed silver thin film, figure 6.2, we can see that even in the case of low fluence and minimal laser pulses, in particular the $25mJcm^{-2}1pulse$ and $50mJcm^{-2}1pulse$ areas, there is the appearance of a subtle reflectance peak that suggest that a nanoparticle template has been produced. The collaborating SEM micrograms prove that there has been a transformation from a thin film to a nanoparticle template. As seen in figure 6.2. These nanoparticle templates were produced at a significantly lower processing window than that used when working on a silicon substrate (above $200mJcm^{-2}$.As seen, a fluence above $150mJcm^{-2}$ causes the complete ablation of the silver thin film on PET, while of silicon this same fluence is insufficient to produce a nanoparticle template. Due to the inherent interaction of the laser line with the PET substrate, we can conclude that the absorption of the laser in the substrate hinders the production of a plasmonic nanoparticle template.

Additionally, the nanoparticle templates produced on PET are of a much lower quality than those produced on a silicon substrate, based on the low surface coverage of the nanoparticles and the associated large inter-particle distance. The highly disperse structure of the template, in parallel with the transparent nature of the PET, affects the optical profile of the template by minimising the magnitude of the reflectivity as well as shifting the spectral position of any LSPR peak that may exist.

The dramatic difference between the structure of the plasmonic nanoparticle templates fabricated on a PET substrate and a template produced on a silicon substrate, could be explained by considering the discrepancies of the thermal conductivity; specific heat capacity; and thermal bulk of these two substrates. Consequently, it can be theorised that a silicon substrate is better able to deal with the energy dissipation necessary during laser annealing, in both a LISA and MONA-LISA process.

6.2.1 Interlayer Materials

To address this discrepancy of thermal properties and improve the ability of a PET substrate to support the laser fabrication of a nanoparticle template, it was suggested that the inclusion of an interlayer or '*barrier*' material, could be used to modify the properties of the substrate, allowing for a more successful laser annealing process and the fabrication of a higher quality nanoparticle templates. In addition to the modification of the thermal properties, these interlayer materials

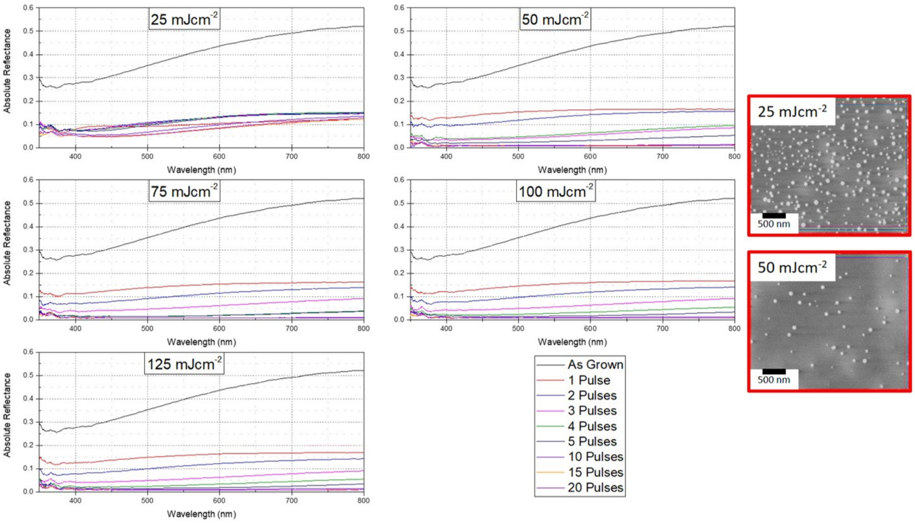

Figure 6.2: Calculated optical reflectance spectroscopy (ORS) absolute reflectance of the unprocessed and laser annealed areas of the thin silver film on a PET substrate, for a range of fluences. The inset SEM micrographs show the surface structure of the processed areas where the coloured borders correlate to the plot colours.

could be used as an active functional layer, essential for the operation of a given device, such as a charge transport layer or a dielectric / conducting layer.

Four specific interlayer materials were identified for investigation, due to the range of physical, thermal and electrical properties they span, as seen in table 6.1. As well as providing a wide range of properties for instigation, these materials are all established within their relevant fields, namely: silicon dioxide (SiO_2) is a classic material used in electronics; yttrium oxide (Y_2O_3) is a highly versatile dielectric material; and indium-tin oxide (ITO) and aluminium-doped zinc oxide (AZO) are used extensively as transparent conductors. All of these materials were deposited as thin films using room temperature RF magnetron sputtering in a high vacuum chamber (base pressure of $< 10^{-6} mbar$), from round (3”) targets, in the presence of argon (99.999% purity) and in the specific cases oxygen (99.999% purity), at a fixed flow rates to produce working pressure of 3 - 5 mTorr (depending on the material). Each of these interlayer materials were deposited onto a PET substrate to a range of thicknesses. This allowed for an investigation into both the influence each of the interlayer materials has on the laser annealing process as well as the identifying the influence of interlayer thickness.

Materials	Thermal Conductivity κ $Wm^{-1}K^{-1}$	Specific Heat Capacity C $Jkg^{-1}K^{-1}$	Band Gap E_G eV	Resistivity ρ Ωm	Absorption Coefficient @ 248 nm μ_a cm^{-1}	Dielectric Constant
Substrates						
Si	130	700	1.11	0.1 - 60	5.43×10^{-5}	11.9
PET	0.15 - 0.24	1000	3.87	1.00×10^{21}	1.00×10^{5}	3.4
Air (O_2)	0.0257	1005	5.7	$1.3 \times 10^{16} - 3.3 \times 1{-}^{16}$		1.00059
Interlayer Materials						
SiO_2	1.3 - 1.5	680 - 730	9.3	$1.00 \times 10^{15} - 1.00 \times 10^{19}$	700	3.9
Y_2O_3	13.7	453.5	5.6	1.00×10^{7}	4.00×10^{3}	14 - 18
ITO	20	490	3.5	3.5×10^{-6}	1.07×10^{7}	
AZO	20	494	3.5	1.8×10^{-5}	7.0×10^{6}	

Table 6.1: Table showing the diverse range of properties, both thermal and electrical, of the interlayer (*barrier*), materials. This table allows for the identification of the key physical property or properties necessary for a substrate / interlayer composite to facilitate its use as a laser annealing substrate. Although air does not act as a substrate, when laser annealing in an ambient environment, the air acts as vital thermal conductor during the annealing process in a similar way to the substrate and should therefore be considered in the same context.

Each of these interlayer materials produced a significant change to the optical profile of the resultant nanoparticle templates, but further discussion will be focused on the 100 nm thicknesses of each interlayer material, as this interlayer thicknesses exhibited the greatest influence on the nanoparticle templates. As shown in figure 6.3, the inclusion of the interlayer material induced, in cases where there was not total ablation, the formation of a *bed sheet* like structure. The associated SEM micrograms in figure 6.3, show an obvious creasing and wrinkling of the interlayer / silver composite, which can most clearly be seen in the case of the PET / SiO_2 / Ag sample. Across all the investigated interlayer thicknesses, but most easily observed with an interlayer thickness of 100 nm, it is evident that the ablation threshold, the laser fluence or number of treatment pulses required before the silver thin film is fully ablated has been lowered below that seen without the interlayer material. Additionally, in some cases the interlayer material was ejected or delaminated from the substrate, as evidenced by the presence of large areas of exposed PET, seen as dark areas in the SEM micrographs.

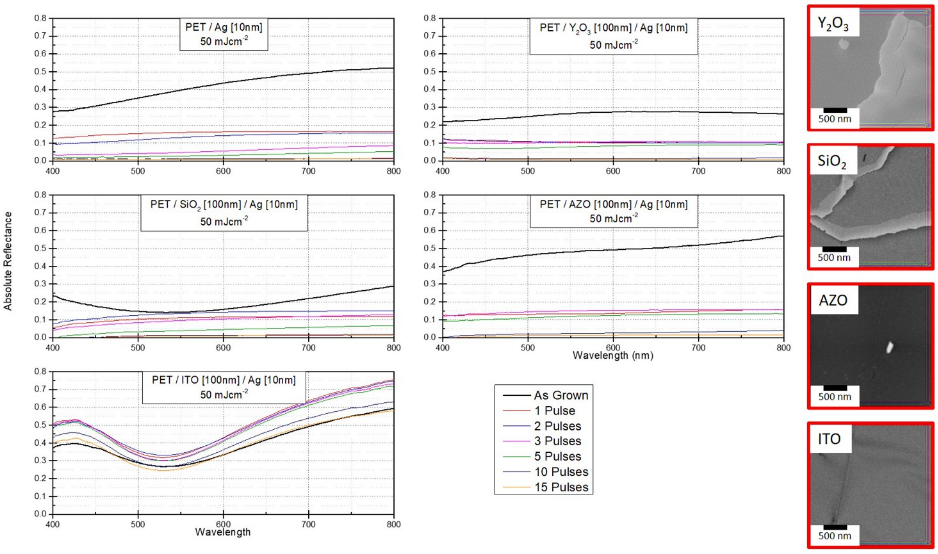

Figure 6.3: SEM micrographs and associated Optical Reflectance Spectroscopy (ORS) spectra of a sample series demonstrating the influence of the different interlayer materials on the formation of laser fabricated plasmonic nanoparticle templates for a single laser energy and an identical pulse progression. Each of the barrier samples shares a structure (PET / Barrier material [100nm] / silver film [10nm]) to understand the effect of the individual barrier layers. Additionally, the PET / silver film [10nm] sample is included for comparison. The inset SEM micrographs show the surface structure of the processed areas where the coloured borders correlate to the plot colours.

In addition to the experimental investigation, a computational investigation into the absorption of the laser line in the PET substrate, the silicon dioxide interlayer and the silver thin film. This study was conducted *via* 3-dimensional finite - difference time - domain (3D FDTD) method. For this investigation, the silica interlayer material was selected for simulation due to the optical response from the experimental PET / silica / silver sample showing the highest potential as an effective interlayer to facilitate the laser fabrication of a nanoparticle template on a PET substrate.

These computational simulations, as seen in figure 6.4, show that at either of the possible processing wavelengths (248 nm from KrF and 193 nm for ArF), the absorption of the laser line in the PET substrate and the silica interlayer are consistent at 50% (39% – 54%) and 3% (0% – 5%) respectively, across all of the simulated silica thicknesses. When considering the absorption within the silver film however, at the three experimental silica thicknesses produced: 50 nm; 100 nm; and 150 nm, we can see that at 193 nm the achieved absorption is at a relative maximum (29% – 35%) while with 248 nm the situation is reversed as the absorption can be seen reach a minimum (7% – 11%). From this, it was concluded that the low absorption in the silver film and the high absorption in the PET substrate could easily lead to the ablation and delamination observed. The discrepancy in the absorption and the resultant thermal heating could lead to this effect by exploiting the low interface adhesion as a mechanism to dissipate the energy gained by the substrate.

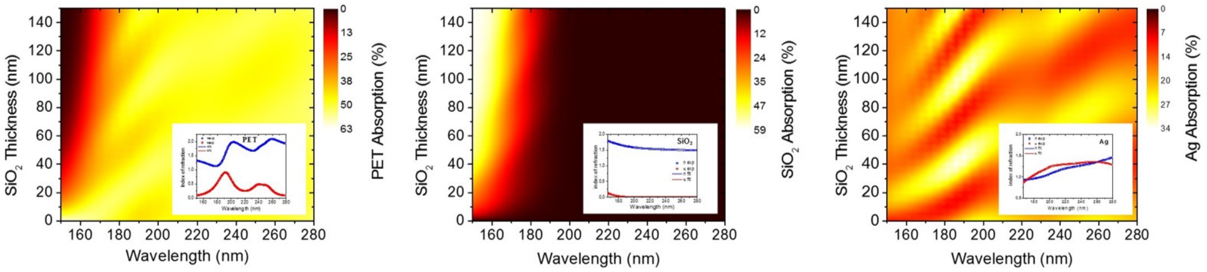

Figure 6.4: The absorption and inset the dielectric function of the PET substrate, silica interlayer and the silver thin film.

6.2.2 Interface Modification

The modification of the processing window is inherent when using a different substrate, as evidenced in figure 6.2. However, the significant increased probability of ablation; the delamination of the interlayer material; and the wrinkled, creased, *bed-sheet* like structure can be clearly attributed to the presence of the interlayers, seen in figure 6.3. It was suggested that in addition to a modification of the properties of the substrate, the inclusion of the interlayer material alters the layer adhesion within the sample, which would attribute to the ease of delamination seen during laser annealing. This low layer adhesion would simultaneously hamper our ability to fabricate a nanoparticle template. Overcoming this phenomenon represents a clear milestone towards the laser fabrication of a plasmonic nanoparticle template, *via* laser annealing, on a PET substrate.

To counter this lowering of layer adhesion, there exist two primary routes towards addressing this layer adhesion, through a physical or chemical process. While a chemical process has several advantages and would be highly successful in increase the adhesion at the PET / interlayer, by necessity, the procedure would need to be unique for each of the interlayer materials used. This significantly complicates the process and forces the inclusion of several additional variables on top of the interlayer thickness and material. Consequently, it was concluded that a physical process would be beneficial, despite the lower adhesion possible. A physical process was selected as it would allow for a single process to be used with all the interlayer materials to increase the interface adhesion. This would allow for the direct identification of the layer adhesion on the laser annealing process. To increase the layer adhesion, the PET surface was roughened prior to the deposition of the interlayer material, *via* plasma etching. This was performed with a Tegal Plasmaline 415 Asher plasma asher, using 2% oxygen in argon ($2\%O_2$ in Ar) gas to produce a plasma with 100 W of applied power at a working pressure of 15 mTorr. The PET substrate was treated for one hour (60 minutes) to modify the surface roughness, as shown in figure 6.5. From figure 6.5, we can see that there is a significant modification to the PET surface, where the transmission of the PET substrate fell from 97% to 65%. The modified substrate, henceforth described as plasma-etched PET or PE.PET, was then deposited with the established interlayer barrier materials, using the RF magnetron sputter deposition technique discussed previously.

Figure 6.5: Image showing the difference between the untreated (*left*) and plasma etched (*right*) PET with an increased surface roughness prior to the deposition of a barrier material.

As the surface of the PE.PET has inherently been modified, it is conceivable that the magnitude of the surface adsorption of gases will be dramatically increase. Due to this, before the deposition of the interlayer materials, the PE.PET substrate was held under vacuum within the deposition chamber for 30 minutes to allow for the substrate to out-gassing and to ensure the quality of the interface produced. This technique allowed for increased layer adhesion demonstrated by the much lower sample damage form routine handling and the increased sample lifetime when compared to the untreated PET substrate. While it is of worth to note that the extended lifetime and improved sample stability of the PE.PET samples, they are still significantly more fragile samples than those produced on a silicon substrate. As it was previously identified that the interlayer materials produced the greatest influence on the production of a nanoparticle template at a thickness of 100 nm, all the barrier materials were deposited onto the PE.PET substrate to this thickness before being topped with a 10 nm discontinuous film of silver and subsequently laser processed.

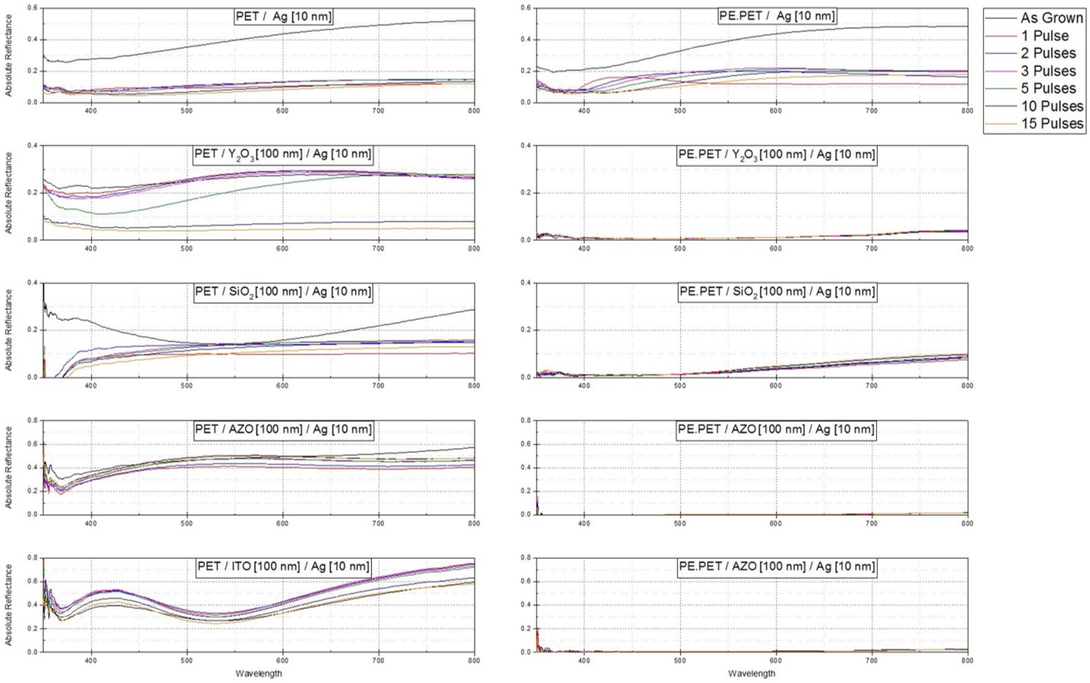

Figure 6.6: The optical reflectance spectroscopy (ORS) calculated absolute reflectance for the interlayer materials deposited onto both the untreated and plasma treated PET treated with a number of laser pulses at a laser fluence of $25mJcm^{-2}$. Where the PET / Ag and PE.PET / Ag are included for comparison.

As shown in figure 6.6, we can see that for the case of both the PE.PET / silver (no interlayer) and PE.PET / silica / silver, the modification of the PET surface had a significant improvement on the optical profile of the laser fabricated nanostructure. The PE.PET /silver sample demonstrate a clear LSPR peak when treated with low fluences and low numbers of laser pulses (most evidently when processed with one laser pulse at $25mJcm^{-2}$). Beyond this, the response seen from subsequent laser pulses suggest that additional laser pulses allow for the modification of the optical response of the nanoparticle template, comparable with the behaviour achieved on a silicon substrate. Additionally, in the case of the PE.PET / silica / silver, all the investigated laser pulses appear to demonstrate a bimodal optical response, with two clear peaks, where again successive laser pulses onto the sample show some modification to the optical response.

In the case of the other interlayer materials, but most prominent in the case of the ITO interlayer, the optical response of the laser processed areas have been quenched, with a reflectance below 1% for all laser fluences and pulses used. Further to this, from the direct comparison between the plasma treated and untreated PET substrate, we can conclude that our ability to successfully fabricate a plasmonic nanoparticle template on a polymeric substrate has been improved by the combination of increasing the surface adhesion and modification of the substrate's properties. This improvement can be attributed to a combination of the increased thermal bulk of the sample due to the inclusion of the interlayer as well as the enhanced layer adhesion due to the increased surface roughness from the plasma treatment of the substrate. The phenomenon of the low reflectance in all cases of the roughened PET substrate can be attributed to the base optical response of the substrate at two stages. Initially, the untreated PET substrate is inherently transparent and as such has a very low optical reflectance, with a reflectivity of 4% - 6%, while when the substrate is plasma etched, the PE.PET which has caused an increased to the surface roughness, significantly increasing scattering and further reducing the optical spectral reflectance. These two factors, in combination with the low ablation limit of the interlayer / silver composite results in an overall low reflectance profile of the laser annealed areas.

6.2.3 SERS Effect on Flexible Substrate

This low reflectance from the laser annealed areas of both the PET / interlayer / silver and PE.PET / interlayer / silver samples, makes the traditional reflectance spectroscopy methodology for characterising and identifying the presence of the plasmonic nanoparticle template unreliable. Consequently, another method for the identification of an additional route towards this. As such, it was concluded that a Raman microscope (Thermo Scientific DXR2) could be used to simultaneously probe the ability of these laser fabricated plasmonic nanoparticle templates to act as a surface enhanced Raman spectroscopy (SERS) surface, while also allowing for the identification of a plasmonic structure and to quantify their spectral position. The Raman spectra were measured with a 532 nm probe wavelength at 0.5 mW in a $100\mu m$ spot size, using a spectroscopic detector with a maximum spectral range of $100-3500cm^{-1}$operating at $16-27^{O}C$.

To this end, an establish Raman active compound, namely the dye rhodamine 110 chloride (Rh110) (Sigma Aldrich, $\geq 88\%$ purity, $\lambda_{max} = 496nm$), was selected due to the corresponding low fluorescence associated with the pumping wavelength of the Raman microscope used (532 nm). The rhodamine dye was produced at three stock solutions at specific concentrations ($40mM$, $40\mu M$ and $40nM$) in ethanol that could be used to assess if there was any SERS enhancement, while also proving a route towards identifying the nanoparticle template that results in the greatest enhancement. This would allow for a single measurement to provide evidence that a plasmonic nanostructure exists with a LSPR peak that lies near the pumping laser wavelength of the Raman microscope while simultaneously assessing the quality of a potential SERS surface. Two samples were selected for assessment with a Raman microscope: the PE.PET / silver [10 nm]; and the PE.PET / silica [100 nm] / silver [10 nm] samples. These samples were selected based on their optical reflectance spectroscopy (ORS) measurements of these two samples demonstrated the clearest indication of a LSPR peak that could allow for a SRES enhancement.

Before any SERS behaviour can be characterised, the inherent detection limit of the Raman microscope must be established. To identify the minimum concentration detectable and to align with the standard concentrations used for SERS measurements, the stock solutions of the Rh110 dye were assessed on the as deposited, 10 nm thin silver film of 3 substrates: plasma etched PET; plasma etched PET / silica [100 nm] composite; and a silicon wafer, as a reference and control sample. Each concentration was evaporated on the as deposited silver film as a microliter ($1\mu L$) droplet and allowed to evaporate under ambient conditions. These Raman spectra can be seen in figure 6.7.

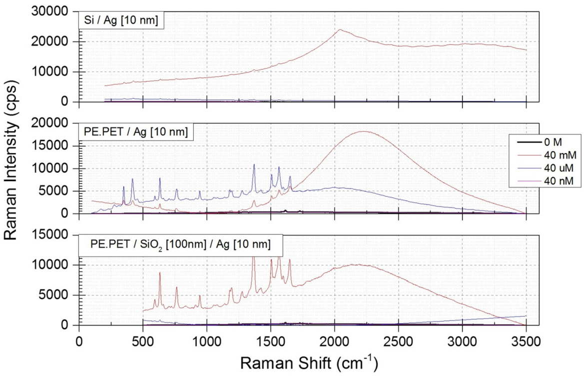

Figure 6.7: Raman spectra from the three stock solutions, 40 mM (red), 40 µM (blue) and 40 nm (pink) of Rh110 dye, as well as the spectra from the as deposited silver thin film (black). Three samples were investigated, Si/Ag, $PE.PET/Ag$ and $PE.PET/SiO_2/Ag$. As can be seen across all samples, the milli-molar (mM) concentration demonstrates a large fluorescence peak despite the selection of a dye with a minimal fluorescence at the laser line of the Raman microscope.

The detection limit of the Raman system, shown by the concentration that displays a clear Raman signal with a minimum number of counts, can be seen to be the 40 nM solution across all three substrates, but most clearly on the PE.PET / silica / silver sample. While the silicon sample exhibits significantly higher counts in all cases than both PET samples, this is to be expected, as the silicon has a significantly higher visible optical reflectance, particularly at the probing laser wavelength (532 nm). Subsequently, the selected laser annealed areas on all three of the tested substrate samples (PE.PET / silver, PE.PET / silica / silver and Si / silver) were exposed to the Rh110 solution as described previously ($1\mu L$ droplets placed on the selected areas and allowed to evaporate under ambient conditions) using the 40 nM concentration, as this concentration most closely resembles the concentrations used for the testing of a SERS surface seen in literature. From each sample, the laser annealed areas were selected based on their optical response and how likely is was that this LSPR peak would allow for a SERS enhancement. As such, the $500mJcm^{-2}$, $25mJcm^{-2}$ and $50mJcm^{-2}$ laser processing fluences were selected for the Si/Ag, $PE.PET/Ag$ and $PE.PET/SiO_2/Ag$ samples respectively, where the measured Raman spectra can be seen in figure 6.8.

The Raman signal from both PE.PET substrates across all the laser annealed areas exhibit almost identical spectra, where the identifiable Raman peaks that can be seen can be attributed to the PET substrate and not the rhodamine dye. For the case of the silica interlayer and the case of the PE.PET / Ag sample treated with 1 pulse, the distinct, broad double peaks around $1400cm^{-1}$ and $1500cm^{-1}$, are indicative of carbon *d*- and *g*- bands, which is indicative of sample burning. The evidence of sample burning (the burning of the Rh110 dye) provides a significant indication that the LSPR of these nanoparticle templates is centred close to the laser wavelength (532 nm) and therefore enhancing the probing laser, leading to this burning, rather than enhancing the Raman signal. The lack of any SERS enhancement could be attributed to the spectral position of the LSPR peak not corresponding to the Raman peaks of the dye, but the evidence of burning suggest that the LSPR peak must lie close to the laser line and consequently should be providing some signal enhancement. Alternatively, due to the inherent low reflectivity and therefore the low measurable signal from the PE.PET samples and the low concentration used, it is possible that the signal is sufficiently low so that it is below the detection limit of the Raman microscope.

To establish which of these effects led to the lack of signal enhancement, a second experimental test was designed, where a second sample series was produced and processed identically to the PE.PET / silver and PE.PET / silica / silver samples described previously. However, this time the samples were exposed to the $40\mu M$ concentration before measuring with the Raman Microscope, to identify if the apparent lack of enhancement could be attributed to the low measurable signal rather than the lack of any enhancement. These spectra can be seen in figure 6.9. It can be clearly seen that for the case of the PE.PET / silver sample, that there are

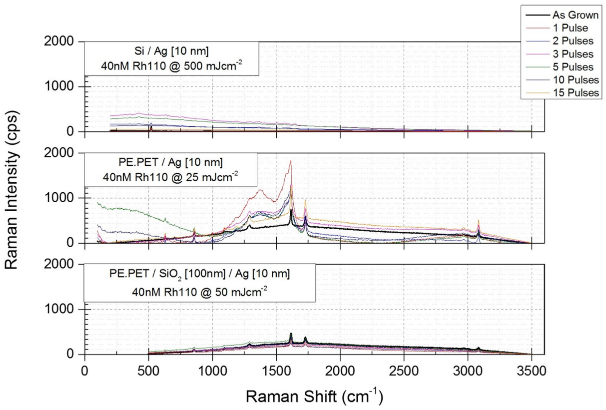

Figure 6.8: Raman spectra from the 40 nM solution of Rh110 dye, as well as the spectra from the as deposited silver thin film (black). The selected laser fluences investigated were selected due to the spectral position of the expected LSPR peak position. Three samples were investigated, Si/Ag, $PE.PET/Ag$ and $PE.PET/SiO_2/Ag$. The dominant peaks between $1400 - 1500cm^{-1}$ are characteristic of the *d*- and *g*- bands of carbon, indicative of burning.

a number of laser processed areas which demonstrate an enhancement to the detected signal, despite no obvious optical fingerprint of a nanoparticle templates seen from the ORS spectra. This enhancement can be seen in the Raman signal allows for the identification of multiple Rh110 specific Raman lines, as well as increasing the measurable signal by orders of magnitude when compared to the signal of the same concentration of the as deposited silver film (black line in figure 6.9. In contrast, when we consider the PE.PET / silica / silver sample, we can see that of all the assessed laser annealed areas, only one demonstrate an enhancement of the Raman signal, namely the $50mJcm^{-2}$, 2 pulses template. This template is not only the only template to exhibit a SERS enhancement, but also the template across both PE.PET samples that show the cleanest enhancement with the most obvious Raman peaks.

From the measure Raman spectra, the two laser processing conditions, one for each substrate, identified that resulted in a significant signal enhancement when compared to the same concentration applied to the as deposited silver film. As can be seen in figure 6.10, both the $PE.PET/Ag$ and the $PE.PET/SiO_2/Ag$ sample demonstrate an obvious enhancement when compared to the same concentration evaporated on the unprocessed silver film, caused by the laser fabrication of a plasmonic nanoparticle template on the PET substrate. Further to this, the greatest enhancement can be seen from the PE.PET / silica / silver sample, where the magnitude of enhancement can be seen to allow for the reliable identification of the compound under investigation by allowing for the clear distinction between the Rh100 specific Raman lines and the Raman signal from the PET substrate, showing a SERS enhancement factor of $G = 45$. As

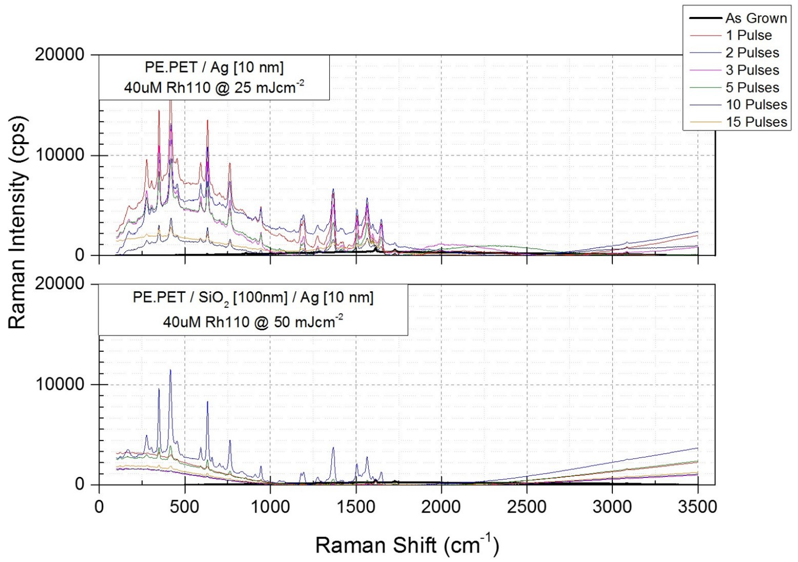

Figure 6.9: Raman spectra from a solution of $40\mu M$ Rh110 dye in ethanol evaporated onto the laser processed areas from two PE.PET substrate samples. The highest signal can be identified from each sample as $25mJcm^{-2}$, 1 pulse for the $PE.PET/Ag$ sample and $50mJcm^{-2}$, 2 pulses for the $PE.PET/SiO_2/Ag$ sample. Both of these laser treated areas demonstrate an enhanced signal, with clear Rh110 specific Raman peaks, that cannot be seen when the identical solution was evaporated onto the untreated silver film.

such this measurement, simultaneously provides evidence that a plasmonic nanoparticle templates have been successful laser fabricated on a flexible and transparent polymer substrate, while also allowing for confirmation that such a template can be used as a SERS substrate for the enhancement of the Raman signal of a given compound.

6.3 Conclusions

The ability to reliably and with control, produce a nanostructure on a flexible polymer substrate represent a clear and distinct barrier that needs to be overcome before such substrates can become more widely utilised, and this is no less the case for the field of plasmonics. Therefore, the development of a methodology for the laser fabrication of a plasmonic nanoparticle template on a PET substrate is necessary to develop a flexible polymer SERS surface as well as other applications.

The transfer of the laser annealing process from a rigid silicon substrate to the PET polymer, introduce a series of difficulties, including the significant decrease of the available processing window and additional interactions of the laser line with the substrate. This equates to a

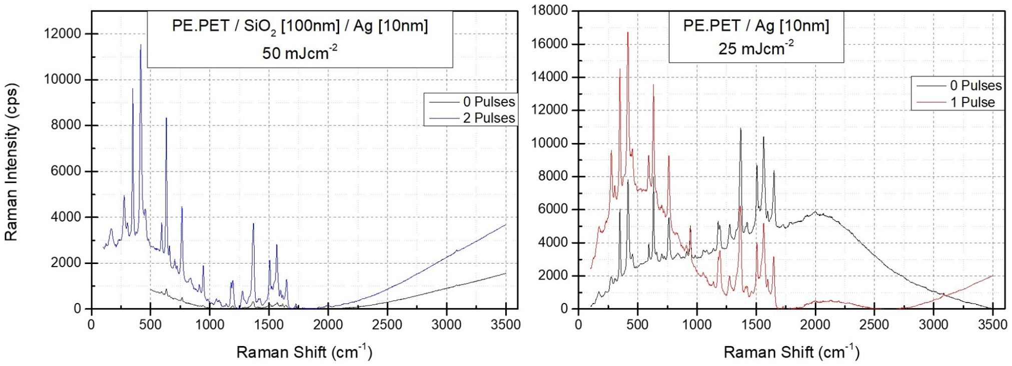

Figure 6.10: Raman spectra of Rhodamine 110 chloride on two different plasmonic nanoparticle templates, one fabricated in a $PE.PET/SiO_2(100nm)/Ag(10nm)$ structure processed with 0 and 2 pulses of $50mJcm^{-2}$ (left) and one fabricated in a $PE.PET/Ag(10nm)$ structure processed with 0 and 1 pulses of $25mJcm^{-2}$ (right). Spectra showing the variation of Raman signal caused by the Ag nanostructuring caused by the laser annealing process.

dramatic loss of control in the fabrication and the nanoparticle templates that were produced, had an exceptionally low optical reflectance and lacked a clear LSPR peak. Resulting in the direct transference of the laser annealing process onto a polymer substrate not being possible. However, this is not a complete road block towards the use of such a substrate.

The thermal mass, specific heat capacity and the thermal conductivity of PET is notably lower than that of silicon, which could account for the difficultly of producing a nanoparticle template. To counter this, an interlayer material could be used to counteract this discrepancy of the properties. The addition of an interlayer or barrier material introduced another series of challenges, but primarily the remarkable ease of delamination during the laser annealing process and producing the wrinkling and creasing of the interlayer / silver film complex without any modification of adjustment of the processing window. It can be concluded that the thermal and electrical properties of the substrate and sample cannot be used exclusively to predetermine the success or failure of the laser annealing process.

Therefore, in addition to the addition of an interlayer, it was clear that a method for increasing the layer adhesion, by increasing the surface roughness of the PET substrate prior to the deposition of the interlayer, allow for a significant decrease of the observed delamination. However, and more vitally, the combination of increase interface strength and the presence of a barrier material allow for both production and modification of a plasmonic nanoparticle template through laser annealing, allowing for the use of a polymer substrate to be used as a leaser annealing substrate. Beyond facilitating the production and alteration of a nanoparticle template, the combination of an interlayer material and increased interface strength, enabled the plasmonic nanoparticle templates to be used as an effective surface enhanced Raman spectroscopy substrate, allowing for the enhancement of the measurable signal from the a Raman active, namely the dye rhodamine 11o chloride, by 4 orders of magnitude, allowing for the clear identification of both the dye specific and substrate specific Raman lines that was impossible without the presence of the laser fabricated nanoparticle templates.

Chapter 7

Angle and Polarisation Dependent Reflectance Spectroscopy

7.1 Introduction

This chapter will focus on the development of a novel optical assessment technique for measuring the angle and polarisation dependent reflectance for a plasmonic nanoparticle template, or any given sample. Plasmonic nanoparticle templates have been used extensively across a wide range of applications from memory devices [177], photovoltaic devices [178], photocatalytic surfaces [179] and used extensively within sensing and sensor devices [180, 181]. Plasmonic nanoparticles are compatible with such a highly divers and large number of applications due to their powerful and unique optical properties that manifest at the nanoscale based, on the localised surface plasmon resonance effect. This is a resonance oscillation of the surface electrons between the electric field of the incident photons and the restoring force of the positive nuclei This results in a significant increase of the scattering and absorption cross section, producing a characteristic macroscopic reflectance peak [19, 182]. There are many factors that dictate the exact position of this LSPR peak from a plasmonic nanoparticle template, including the nature of the metal they are made from, their size, shape and distribution over the surface and the local dielectric environment, to name but a few [98]. These factors determine the spectral position of this characteristic reflectance peak [7]. This reflectance peak is traditionally assessed normal to the surface, or at normal incidence, where the angle of incidence and detection is 0°. However, this does not necessarily allow for the full understanding of the optical properties of the nanoparticle template. With the rapid and widespread development of flexible [173,173] and elastic [172,175] plasmonic devices, the response of a plasmonic nanostructure at normal incidence is not a true understanding of the optical properties.

There exists within the literature many studies into the optical properties [183] of a plasmonic nanoparticle template including the angular [183,184] or polarisation [185,186] dependent optical properties, covering reflectance, absorption and transmission [187]. These computational and theoretical investigations have focused on a wide variety of applications including LSPR tuning [188], directional emission control [189–191], sensing [192, 193] a perfect absorbing surfaces

7.2 Results and Discussion

7.2.1 Angular Reflectance System

This section will focus on the design, construction, calibration and the measurements from a custom-built angle and polarisation dependent reflectance system produced as part of this research.

Design, Construction and Calibration

At a fundamental level, a successful angular reflectance spectroscopy system must allow for the selection and positioning of specific incidence angles onto a given samples and allow for the selection of specific detection angles. Where the angle of incidence and detection could be equivalent to ascertain the specular reflectance of a given sample but need not be to allow for the measurement of the diffuse reflectance. These two principle requirements heavily dictate the design and construction of an ARS system. The core of the ARS system is an analogue optical diffractometer, traditionally used for the identification and measurement of the Brewster's angle. A diffractometer consists of a fixed position arm, a rotating arm and a rotating sample stage. Both the sample stage and rotating arm are positioned accurately with a goniometer, fitted with a Vernier scale, allowing for angular positioning with a precision of 1 arcminute ($1'$ or $1/60°$). The core components of this diffractometer clearly allows for the two primary goals of selecting and accurately positioning the incident and detection angles for any given measurement. Despite the ease with which the diffractometer allows for the key requirements of this system, the base system uses small scale telescope like assembly fitted with an adjustable slit and an eyepiece on the light delivery and detection arrays respectively.

As most modern light sources and spectrometers are fitted with standardised optical fibre connectors, it was established that the completed ARS system must be compatible with optical fibres. Therefore, it was concluded that the light delivery and detection assemblies must be redesigned. Due to the necessity to include optical fibres, and the inherent dispersion of light from the tip of the fibres, there was a clear and obvious need to limit this dispersion due to two specific situations: firstly the intensity of light incident to the sample could become sufficiently low to minimise the reliability of these measurements; and secondly the area of the sample illuminated, in particular at steeper angles, which could become significantly larger than a single plasmonic nanoparticle template. This would subsequently lead to the measured reflectance being an amalgam of the reflectance for the areas illuminated by the light spot, rather than that of a specific nanoparticle template. Due to this, it was established that in addition to the light delivery and detection assembly allowing for optical fibre coupling, there is a need to include collimating optics to minimise the dispersion and ensure parallel-beam illumination and detection. To achieve this, a custom multi-layer acrylic mounting plate was fabricated that would allow for the independent variation of the illumination-sample and sample-detection distance, to ensure a high detected signal to noise ratio. Additionally, a vertical component to this mounting assembly was fabricated with a hole that was subsequently threaded, to allow for a fibre coupled collimating lens (Ocean Optics 74-UV collimating lens cover a wavelength range of 182 - 2500 nm) to be connected and securely held in place during use. This mounting plate assembly allows for the implementation of both the optical fibres (Ocean Optics QP200-2-UV-VIS fibres covering wavelength range of 300- 1100 nm) feeding in the illumination and detection as well as enabling the use of the collimating optics to ensure parallel beams.

Despite the significant advantages of this acrylic assembly and the number of distinct advantages it has over the original telescopes, the assembly was not capable of supporting the inclusion of the liner polarisers, necessary to establish the polarisation specific reflectance and any polarisation transformation during reflection. The acrylic support struts, while sufficiently strong to support the lenses and optical fibres, are unable to support the liner polarisers necessary to be able to measure both the S-, P- and N-polarisation dependent reflectance from a given sample. As such, the design of the acrylic illumination and detection mountings was taken as a base and re-fabricated in aluminium, to increase the strength of the mounting assembly and to allow for the inclusion of a bracket to hold the linear polarisers. As previously, these aluminium mounting assemblies allowed for the alteration of the illumination-sample and sample-detection distance to ensure a high signal to noise ratio, as well as having a threaded connection for the collimating lens, as described previously, to connect too. For the measurements described in this work, the illumination-sample and sample-detection distance were kept constant at the maximum possible value of 125 mm and the collimating lenses were set to ensure the incident and reflected beams wereparallel, with a spot size at the sample of 2 mm. The final design for this angular reflectance system can be seen in figure 7.1.

The quality of any system is based on the confidence and reliability of the results it provides. As such, it was necessary to devise a method for the calibration of the ARS system. This would ensure that any results achieved from future experiments would be reliable and as accurate as

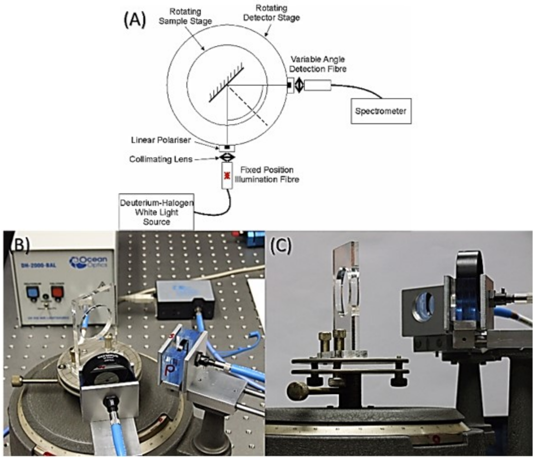

Figure 7.1: Diagrammatic (A), and photographic (B) and (C), views of the custom built, goniometric system for the investigation of the angular reflectance of nanoparticle templates. This system allows for the independent angular positioning of both the sample and detector to allow for the measurements at the largest possible angular variation. Polarisers have been inserted on both the illumination and detection fibres to allow for the identification and assessment of individual polarisation reflectance.

possible. As the focus of this system is to assess the angular reflectance of a plasmonic nanoparticle template, it was therefore concluded that the measurement of the reflectance interference peaks from a metallised diffraction grating, where the correlation between the calculated angular position and the measured angular position of these reflectance peaks can be used to calibrate both the reliability and precision of the angular measurements. Additionally, this test would allow for the quantification any 0 off-set inherent with the produced ARS system. This calibration can be seen in figure 7.2. To achieve this calibration, the fabricated ARS system was modified by removing the two linear polarisers and to the connection a red (653 nm, 5mW) laser diode in place of a white light source to use a stable monochromatic light source and achieve a single set of interference peaks.

It can be clearly seen that there is no systematic error or numerical off-set in the measured reflectance peak position and as such we can conclude that there is no 0 off-set present. Further to this, we can see that the calculated and know values lie comfortably within the experimental error of the measured values. In addition to the experimental values being in strong agreement with calculated and known values, demonstrating that the fabricated ARS system has a great deal of reliability and has a high level of precision. This result provides significant confidence in the angular positioning of the ARS system, where the precision of the angular position can be read with an error of $\pm 1'$ over an specular range of 25° to 90°. Measurements of the angular

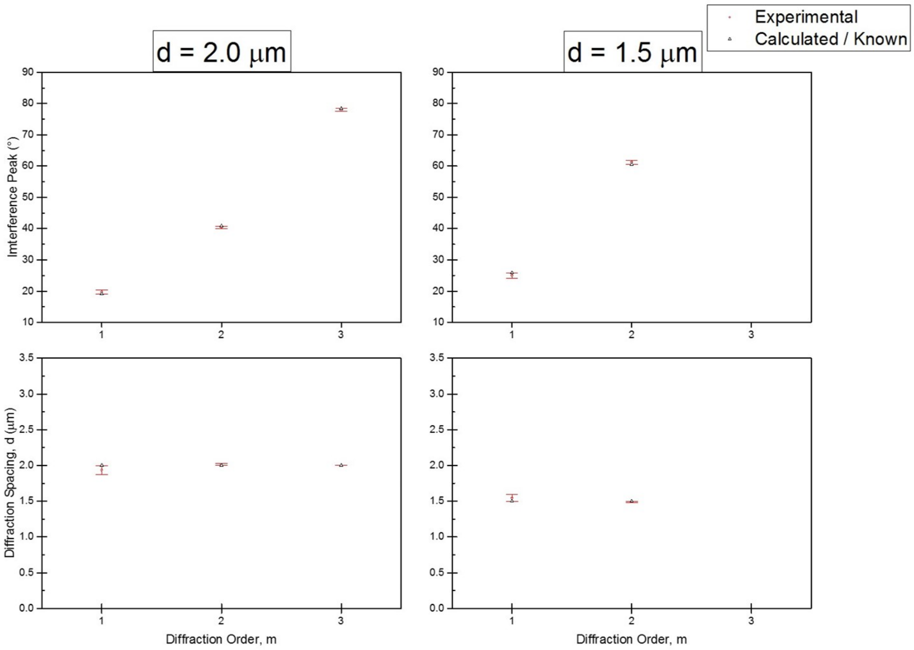

Figure 7.2: Calibration between the calculated angular position of the diffraction interference peaks (*top*) and the know spacing of the diffraction grating (*bottom*) and the corresponding experimentally measured angular position of the diffraction interference peaks and the grating spacing calculated from these values. This has been performed for two specific metallic diffraction gratings with a known grating spacing of $2.0\mu m$ (*left*) and $1.5\mu m$ (*right*). Each of the experimental data points is the average of 3 measured values.

reflectance closer than 25 are not possible bue to the necessary size of the polariser mounting bracket.

Angular Reference Calculations

To calculate the absolute reflectance (AR) of any given sample or material, the following standard reflectance equation can be used:

$$AR = \left(\frac{I_{Sample} - I_{Dark}}{I_{Ref} - I_{Dark}} \right) \times R_{Ref} \tag{7.1}$$

Where I_{Sample}, I_{Dark} and I_{Ref} are the reflected intensities of the sample under investigation, the dark spectrum and the reference material respectively and R_{Ref} is the known reflectance of the reference material. It is here that one of the greatest complications associated with angular reflectance spectroscopy (ARS) is found. The *monochromatic* angular reflectance and the broadband polarisation dependent reflectance *at normal incidence* (0°) of a wide variety of materials are readily available within the literature. However, there is no available reliable source for the broadband angle and polarisation dependent reflectance for any material. As such, a method for the calculation of the theoretical reflectance of the standard reference materials (silicon, gold, silver and aluminium) used in this research must be established before the angular absolute reflectance of a nanoparticle template can be calculated.

It is well known that the reflectance at any angle of incidence of a dielectric material can be calculated using the Fresnel equations:

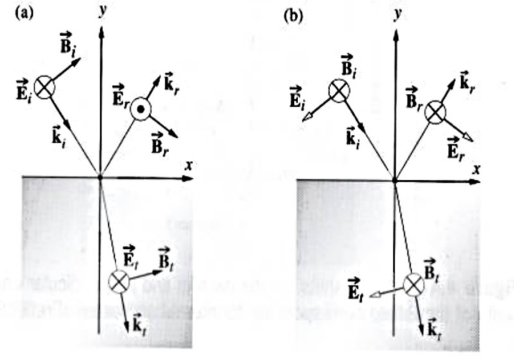

Figure 7.3: Image taken from: ‘Optics, Fourth Edition’; E. Hecht; Adelphi University; Addison Wesley; 0-321-18878-0; Chapter 4, page 117, Figure 4.43. Image (a) shows the electric field vector perpendicular to the plane of incidence – S polarisation. While image (b) show the case of the electric field vector parallel to the plane of incidence – P polarisation.

$$\left(\frac{E_r}{E_i}\right)_S = \frac{n_1 cos\theta_1 - n_2 cos\theta_2}{n_1 cos\theta_1 + n_2 cos\theta_2} \tag{7.2}$$

$$\left(\frac{E_r}{E_i}\right)_P = \frac{n_2 cos\theta_1 - n_1 cos\theta_2}{n_2 cos\theta_1 + n_1 cos\theta_2} \tag{7.3}$$

Where n_1 and n_2 are the refractive indexes of medium 1 and medium 2 respectively, while θ_1 and θ_2 are the angles of incidence and refraction / transmission, where this can be seen in figure 7.3. In the specific case of a reference material for ARS, we are considering light incident onto a metallic reference material, so that n_2 is the refractive index of a metal. However, for the case of a metal, the refractive index can only be fully described using a complex index such as $\bar{n} = n + ik$, so for our specific situation, where we are selecting medium 2 as a metal, we can conclude that:

$$\bar{n}_2 = n_2 + ik_2 \tag{7.4}$$

Additionally, to be able to solve the Fresnel equations numerically, there must be a numerical value for θ_2, the angle of refraction or transmission. This presents a further complication as for a metal surface, the electric field component of an incident light wave is attenuated to practically 0, within a few nanometres of the surface, described as the skin depth, and therefore the intrinsic value of θ_2 cannot be measured. Therefore, to solve this situation numerically, we can use Snell's Law ($n_1 sin\theta_1 = n_2 sin\theta_2$)and a trigonometric identity ($sin\theta^2 + cos\theta^2 = 1$)to describe $cos\theta_2$ as:

$$cos\theta_2 = \sqrt{1 - \left(\frac{n_1}{n_2} sin\theta_1\right)^2} \tag{7.5}$$

Further to this, if we assume that medium 1 is a vacuum ($n_1 = 1$) and that medium 2 is a metal ($\bar{n}_2 = n_2 + ik_2$), we can redefine equation 7.5 as:

$$cos\theta_2 = \sqrt{1 - \left(\frac{1}{n_2 + ik_2} sin\theta_1\right)^2} \tag{7.6}$$

Where from this, we can see that $cos\theta_2$ has inherently both a real ($\Re$) and imaginary ($\Im$) component. As such, henceforth, we will define the solution to equation 7.6 to simplify the further stages:

$$cos\theta_2 = \Re[cos\theta_2] + i\Im[cos\theta_2] \tag{7.7}$$

This now enables us to recreate the Fresnel equations by substituting 7.4 and 7.7 into equations 7.2 and 7.3:

$$R_S = \left(\frac{E_r}{E_i}\right)_S^2 = \left(\frac{cos\theta_1 - (n_2 + ik_2)(\Re[cos\theta_2] + i\Im[cos\theta_2])}{cos\theta_1 + (n_2 + ik_2)(\Re[cos\theta_2] + i\Im[cos\theta_2])}\right)^2 \tag{7.8}$$

$$R_P = \left(\frac{E_r}{E_i}\right)_P^2 = \left(\frac{(n_2 + ik_2)cos\theta_1 - (\Re[cos\theta_2] + i\Im[cos\theta_2])}{(n_2 + ik_2)cos\theta_1 + (\Re[cos\theta_2] + i\Im[cos\theta_2])}\right)^2 \tag{7.9}$$

These equations allow for the calculation of the three-specific polarisation: S; P; and N (where the N-polarisation is the mathematical average of S and P) reflectance of any material, with known n and k values, for any angle of incidence (θ_1). Subsequently, this allows for the calculation of the reflectance of each of our reference materials and for the use of equation 7.1 to calculate the angle and polarisation dependent reflectance of a plasmonic nanoparticle template.

The reference material of choice for these angular reflectance measurements is aluminium, due to its highly uniform reflectance across the UV-VIS range, the ease of access of its n and k values across a wide range of wavelengths and, potentially most importantly, the lack of aluminium within the assessed sample structure. To identify the specific polarisation response, the S- and P-polarisations will be individually measured, while the natural (N) polarisation, will be calculated as the mathematical average of S and P. If we consider the isolated S- and P-polarisation reflectance of a plane surface, there is a theoretical expectation that there will be a general increase / decrease of the broadband reflectance of the sample respectively as we move to steeper angles, while the natural or N-polarisation will again steadily increase at steeper angles as it is the average of the two, as shown in figure 7.4. However, of note is the fact that with our reference materials, we are considering the reflectance of a metallic surface, the reference materials will not show a P - polarisation 0 reflectance minimum, more commonly referred to as the Brewster's angle or the polarisation angle (θ_B or θ_P), as we would expect with a dielectric surface. While the P - polarisation reflection of a metallic surface will exhibit a characteristic minimum, this minimum will not reach 0 reflectance.

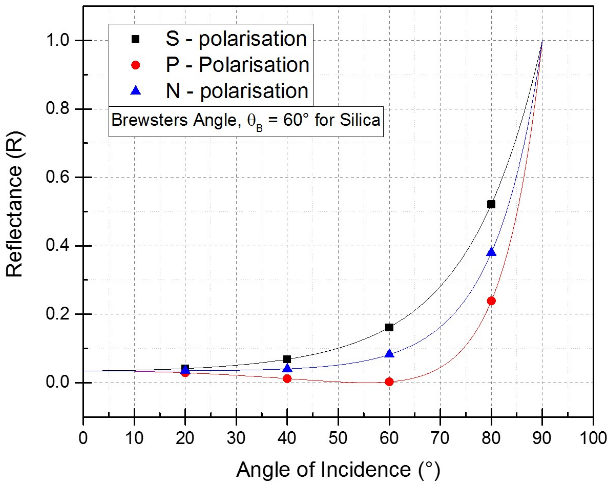

Figure 7.4: Graph showing the polarisation dependent reflectance from a planar surface of bulk silica (SiO_2), where the Brewster's angle or polarisation angle = 60°. Data from RefractiveIndex.org.

7.2.2 ARS Measurements

With the successful design, construction, calibration and preliminary calculations completed, it was clear that a series of samples must be produced so that the angle and polarisation dependent reflectance of a laser fabricated plasmonic nanoparticle template could be assessed. From previous work, it was seen that when a sample consisted of a silica interlayer, thicker than that of the native oxide, there was a clear variation in the observed colouration depending on the angle of illumination and the angle of observation. This effect was not seen for samples where the silica interlayer was not increased beyond the native oxide. As such, a sample series was proposed, so that this colouration variation can be quantified, and the influence of the silica interlayer can be understood.

These samples were produced on a commercial n-type silicon (Si), (100) wafer substrate, where the increased silica interlayer was grown using thermal oxidation in an electrical Carbolite CWF1200 high temperature oven at 1100 °C for set periods of time to allow for the growth of specific interlayer thicknesses. A series of samples were produced; however, this discussion will focus of the 2 nm (native oxide) and 61 nm silica interlayer films. These silicon / silica substrates were subsequently coated with a discontinuous layer of silver, produced *via* RF magnetron sputtering in a high vacuum chamber (base pressure of $< 10^{-6} mbar$), from a round (3”) Ag target (99.99% purity), in the presence of argon (Ar) (99.999% purity), at a fixed flow rate of 4 standard cubic centimetres per minute(sccm) resulting in a working pressure of 5 mTorr. The power applied to the target was set to 40 W while the Si substrates was rotated at 12 revolutions per minute (rpm) to ensure a uniform deposition. The deposition time was set in conjunction with the use of a quartz crystal microbalance to achieve an effective thickness of 10 nm. Following the growth process, all these samples were subsequently laser annealed following a UV MONA-LISA process, using a krypton fluorine, KrF, excimer laser system, delivering unpolarised 248 nm light up to 1200 mJ per pulse (25 ns pule width, 1 Hz repetition rate). The samples were exposed to four specific fluences: $350 mJcm^{-2}$, $500 mJcm^{-2}$, $650 mJcm^{-2}$ and $800 mJcm^{-2}$, with 6 different numbers of treatment pulses, 1, 2, 3, 5, 10 and 15 pulses to produce 24 plasmonic nanoparticle templates on each silica thickness so that the direct influence of the silica thickness on the angular response.

Initially, it was necessary to understand the angle and polarisation dependent reflectance of the as grown silica ($Si/SiO_2[xxnm]$ complex) and the as deposited silver film ($Si/SiO_2[xxnm]/Ag[10nm]$ complex), so the optical response of the untreated sample can be understood and to provide an understanding of the extent of the influence of the thin film interference caused by the presence of the silica interlayer. These spectra can be seen in figure 7.5. When looking at both the native oxide silica and the native oxide silver composite, we can clearly see that while there is a distinct and expected angular variation to the magnitude of the measured reflectance, there is little variation to the spectral shape and characteristics. As the characteristic silicon peak is maintained. Conversely, when we consider the 61 nm silica and silica silver composite, we can see again that there is the expected increase and decrease of the overall reflectance of the S - and P - polarisation reflectance respectively. However, in this case, there is an alteration of the spectral profile. It can be most clearly seen with the silica interlayer silver composite, in the case of the P - polarisation, where at steeper angles there is a significant shift of the reflectance to the UV region, with a corresponding decrease in reflectance at longer wavelengths. This can be attributed to the increased transparency of the silica interlayer at steeper angles, where a greater influence from the silicon substrate can be seen in the reflectance profile of the sample.

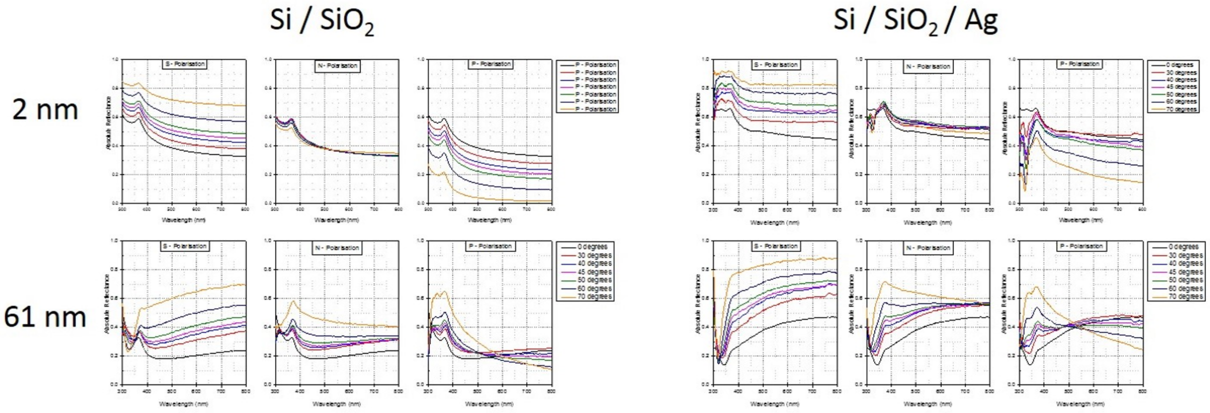

Figure 7.5: Angle and polarisation dependent optical reflectance (ARS) spectra of the as grown silica interlayer (*left*) and the as grown silver film (*right*) on an identical silicon wafer substrate. These spectra are shown for both the native oxide thickness (2 nm) (*top*) and a 61 nm silica interlayer (*bottom*). As expected, there is a general decrease of reflectance when considering the P - polarisation, while conversely, there is a general increase in reflectance when considering the S -polarisation, where the N - or natural polarisation is the mathematical average of the S - and P - polarisation.

With this understanding of the optical response of the as grown films, both the silica interlayer and silver thin film, we can more accurately assess the response from a plasmonic nanoparticle template on both the native oxide (2 nm) and the 61 nm silica interlayer. This will allow us to see if the presence of the nanoparticles induce an additional effect beyond those seen with the as grown films. These spectra can be seen in figure 7.6. When considering the native oxide (2 nm) silica interlayer, we can see that the reflectance across the specific S - and N - polarisations, that there is minimal change to the spectral position of the LSPR peak. However, when we consider the P - polarisation reflectance, we can see that in addition to a general decrease of reflectance, the characteristic LSPR peak can be clearly seen to experience a blue - shift. As seen previously with the as grown films, the S - and P - polarisation of both silica interlayer samples exhibit an expected an overall increase and decrease of reflectance. With the specific S - polarisation reflectance exhibiting a negligible spectral shift, with the primary LSPR peak being altered by the incidence angle by $9nm$ and $15nm$ respectively across the native oxide and 61 nm silica samples. However, when considering the P - polarisation reflectance of the 61 nm silica sample there is significant variation beyond the changing magnitude of reflectance. As seen with both the as grown 61 nm silica and silver films, at steeper angles, the characteristic silicon peak becomes increasingly apparent while simultaneously reducing the reflectivity at longer wavelengths. In this case there is an additional affect to this, where the LSPR peak can be seen to undergo a clear blue - shift at steep angles, shifting to shorter wavelengths and therefore higher energies. This suggesting that the nanoparticle template shows a different optical profile at steeper angles and that the overall observed colouration change cannot be solely due to a thin film interference effect. Instead, this shift is at least in part due to the presence of these plasmonic nanoparticle templates. The change of colouration observed with the naked eye, can be clearly seen when considering the calculated N - polarisation reflectance, where this is the mathematical average of the S - and P - polarisation reflectance. As seen with the P - polarisation reflectance, can be seen to undergo a blue - shift at steeper angles in combination with a general increased reflectance.

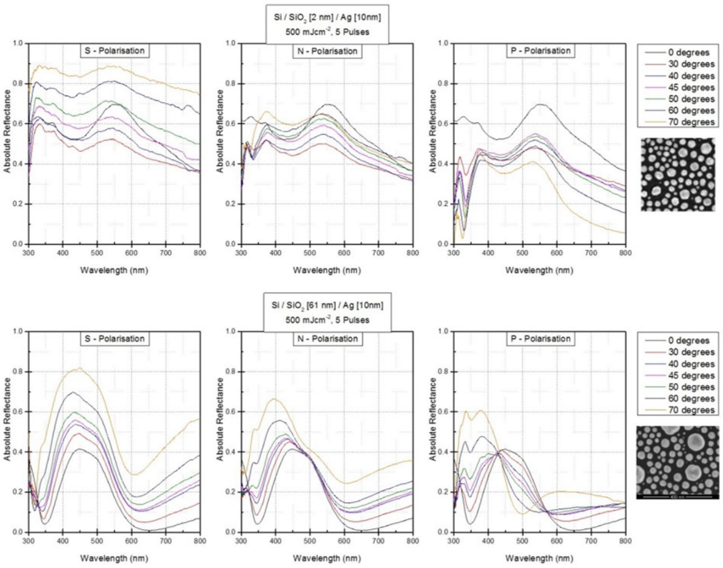

Figure 7.6: Angle and polarisation dependent optical reflectance (ARS) spectra of a plasmonic nanoparticle templates fabricated with identical laser annealing parameters on a $Si/SiO_2(2nm)/Ag(10nm)$ (*top*) and $Si/SiO_2(61nm)/Ag(10nm)$ substrates, where these plasmonic nanoparticle templates were fabricated with 5 pulses of $500mJcm^{-2}$. Were the individual polarisation dependant reflectance for the S - (*left*), N - (*centre*) and P - polarisation (*right*) can be seen individually. The Inset SEM micrographs show the morphology of these nanoparticle templates.

While the absolute reflectance allows for the visualisation of the complete reflectance of the sample, where the absolute reflectance comprises of the optical influence from the substrate and all additional layers, here we require an understanding of how the optical response of a plasmonic nanoparticle templates changes depending on the incidence angle and the polarisation. As such, by assessing the reflectance relative to the effective substrate, or RRES, spectra, where the reflected intensities of the complete sample are normalised by the sample's effective substrate, which is here defined as the layers below the nanoparticle templates. In this specific case the effective substrate is the composite of the silicon wafer substrate and the silica interlayer (Si/SiO_2). The RRES spectra act to minimise the effect of the effective substrate while simultaneously enhancing the prominence of the optical reflectance of the nanoparticle templates, to allow for a greater understanding of the specific spectral position and nature of the LSPR peak associated. Due to the significant blue - shift seen from the 61 nm silica interlayer film, the RRES spectra for the S - and P - polarisation reflectance can be seen in figure 7.7. From the RRES spectra, it can be identified that the blue - shift seen previously in the case of the P - polarisation is not solely due to thin film interference within the silica layer as there is an obvious angular variation of the optical response of the nanoparticle template. However, due to the minimisation of the effect of the silicon silica substrate we can clearly see that the significant increase of reflectance below 400 nm can be attributed to the increased transparency of the silica at steeper angles, as the RRES spectra clearly shows. Similarly, when we consider the specific S- polarisation, we again see a minimal spectral shift of the dominant LSPR peak ($17nm$) however it can be seen that there is a clear and distinct broadening of the LSPR peak, where the contribution of the two nanoparticle size families is equalised and subsequently acting to broaden the LSPR peak.

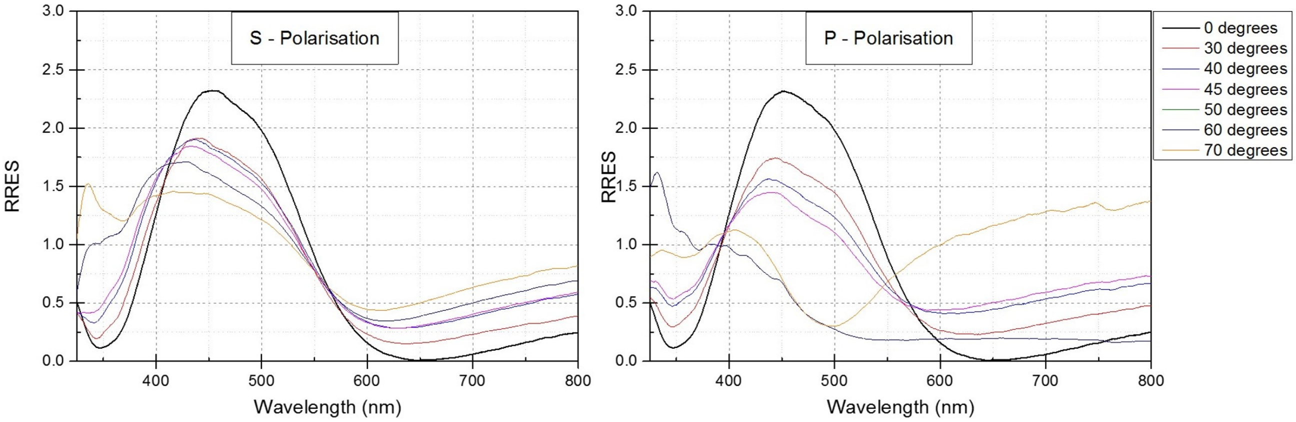

Figure 7.7: Angular reflectance relative to the effective substrate spectra for the $Si/SiO_2(61nm)/Ag(10nm)$ sample, where the specific S - polarisation (*left*) and P - polarisation (*right*) are shown separately.

From the assessment of both the absolute reflectance and the reflectance relative to the effective substrate, we can see that there are two parallel processes leading to the colouration variation seen when the samples are viewed at different angles of illumination and detection. Firstly, there exists interference within the silica interlayer and increased transparency of the silica at steeper angles, when this layer is grown to a greater thickness than the native oxide. This interference leads to a modulation of the reflected light. Simultaneously, the optical response of the nanoparticle template is altered by the angle of incidence. This phenomenon can be attributed to the interaction of the specific polarisations with the inherent shape of the nanoparticles, as seen in figure 7.8. If we consider the nanoparticles to be hemispherical and firstly consider a reflectance measurement at normal incidence (where the angle of incidence and detection is

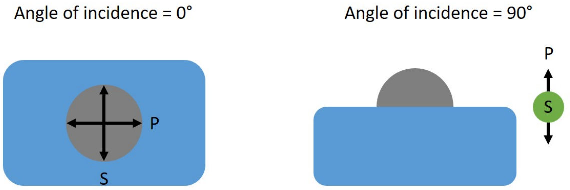

Figure 7.8: Diagrammatic explanation of the mechanism behind the reflectance peak shift found in the P-polarisation ARS. As the ARS is measured at steeper angles, the P-polarisation is probing the vertical axis of the PNP, while the S-polarisation always probes the horizontal axis which will remain constant.

This correlation between the spectral position of the LSPR peak of the plasmonic nanoparticle template at normal incidence (0°) and at steeper angles, such as (60° and 70°), we can use this ARS system to gain a general, qualitative understanding of the morphology of the plasmonic nanoparticle template. Based on the position of the LSPR peak at normal incidence and at steep angles, considering both the S- and P-polarisations, it is possible to draw a conclusion as to a relative ratio of the horizontal and vertical dimensions. Here we can take the example of the 61 nm silica interlayer sample, where we can clearly see that the reflectance peak of the P-polarisation is clearly located at a shorter wavelength than the peak identified in the S-polarisation, suggesting that the vertical axis of the nanoparticle is smaller than the lateral axis. This allows us to conclude that the vertical size (normal to the surface) is smaller than the horizontal size and further to this we can assess that theses nanoparticles are indeed hemispherical in shape.

7.3 Conclusions

Here we present the development, fabrication, calibration and selected real world measurements from a unique, custom, goniometric, angle and polarisation optical reflectance measurement system designed and built in house. This investigation offers a unique experimental investigation of the angular reflectance of a nanoparticle template on specific silica interlayer thicknesses. We present the distinct differences between the specific S -, P - and N - polarisation reflectance across a wide range of angles, from 0° (normal incidence) to 70°. From these nanoparticle templates, we can provide evidence that the spectral shift seen in the N - polarisation is driven by two complimentary mechanism, firstly the inherent thin film interference within the silica interlayer and the secondly the specific polarisations probing the two axis (lateral and vertical) of the individual nanoparticles, giving rise to the significant shift seen from the P - polarisation reflectance and real world colour change. The comparison of the reflectance of the S - and P - polarisation at normal incidence and at 70° , it is possible to gain a quantitative understanding of the relative lateral and vertical size of the nanoparticles under investigation. This unique optical measurement system can further be used to provide the only experimental method for the end user of a given optical device, to modify the optical response to better suit the given application based exclusively on the angle of incidence.

Chapter 8

Conclusions Future Work

8.1 Introduction

This research was conducted with the aim of providing clear evidence that a laser fabricated plasmonic nanoparticle template on a silicon substrate and a polymer substrate can act as an effective sensing surface. The nanoparticle template was fabricated with a custom laser annealing methodology from a discontinuous 10 nm thin film produced via RF magnetron sputtering. Each sample was processed with a range of laser parameters to produce the widest possible range of nanoparticle morphologies; assessed optically *via* ORS; and where appropriate, additional surface analysis techniques such as SEM imaging or XPS analysis. This chapter will discuss the key conclusions from this work, as well as proposing avenues for future work.

8.2 Conclusions

The most vital conclusion from this work, is that the high control in the surface morphology of the laser fabricated nanoparticle temples offered by laser annealing, enables the production of a sensing surface of remarkable diversity and range of applications.

The initial investigation in chapter 4 focused on assessing a laser fabricated nanoparticle template on a known substrate, namely silicon, to act as a sensing surface. We presented a simple yet sophisticated alteration to an established LSPR sensing methodology. This involved the removal of an inherently complicated functionalisation stage in the fabrication of a LSPR spectroscopy sensor, to produce a *naked* nanoparticle sensing surface. Through the optical characterisation of the as fabricated nanoparticle templates, the treatment of each template with a lead salt solution, post treatment optical characterisation and finally the analysis of each template *via* XPS, it was evident that the lack of functionalisation did not result in the lack of a sensing surface. The naked nanoparticle sensing surface was able to detect a concentration of 100 ppm of lead at the surface. Of note was the discrepancy of the pre- and post-lead treatment optical response of the naked nanoparticle sensing surface when compared to the behaviour seen in the literature, with the naked nanoparticles showing a unique blue-shift. This unexpected phenomenon can be attributed to difference in the Fermi energies allowing for electron transfer from higher energy states in the lead to vacant lower energy states in the silver due to the adsorption of the lead directly onto the silver nanoparticles.

In chapter 5, focused on assessing the compatibility of laser annealing process on a PET polymer substrate and assessing if a nanoparticle template on a PET substrate could also act as a sensing surface. It was shown that a direct duplication of the laser annealing process, as both a LISA and MONA-LISA process, did not allow for a duplication of the effect seen on a silicon substrate. This can be easily explained by the dramatic difference between the physical properties of silicon and PET. To counteract this, the inclusion of an interlayer materiel between the substrate and the silver tin film into the sample structure, where a range of interlayer materials and thicknesses were investigated to cover a range of thermal and electrical properties. Of the investigated interlayer materials and thicknesses, it was shown that the inclusion of a silicon dioxide interlayer with a thickness of 100 nm allowed for the greatest improvement to the nanoparticle template produced. Despite the improvement seen with the interlayer, there was a significant increase in the probability of ablation and delamination at even low laser fluences. To counteract this low layer adhesion, the PET substrate was roughened, *via* plasma etching, prior to the deposition of the interlayer. The combination of the inclusion of an interlayer and the roughening of the PET substrate, resulted in the most promising optical response seen in this investigation. However, due to the transparent nature of the PET as well as the increased scattering associated with increasing the surface roughening, the optical response of the produced templates was difficult to identify through simple ORS measurements. However, an alternative methodology for probing the LSPR of the produced nanoparticle templates was identified, namely probing a Raman active compound adsorbed onto the PET / interlayer material / silver nanoparticles samples with a Raman microscope. Beyond providing clear evidence that a plasmonic nanoparticle template had been produced, this investigation proved that a plasmonic nanoparticle template on a plasma etched PET substrate, covered with a 100 nm interlayer of silicon dioxide and capped with a 10 nm silver film produced the greatest surface-enhanced Raman spectra. The SERS enhancement for this sample allowed for the clear detection of the specific Raman lines for both the rhodamine 110 dye and the PET substrate by 4 orders of magnitude.

Chapter 6 attempted to resolve several unanswered questions raised from the work present in chapter 5, namely the exact influence that an interlayer has on the laser annealing process. Due to the difficulty of transplanting the laser annealing process onto a polymer substrate, it was shown previously, that the inclusion of an interlayer provides an improvement to the ability to produce a nanoparticle template on a polymer substrate. However, this introduced a number of new variables to the already variable rich process of laser annealing. Consequently, to minimise the number of parameters under investigation in a single experimental series, the concept of including an interlayer was simplified. This was achieved by using a well-known substrate, silicon; a single understood interlayer, silicon dioxide; and single pulse, or LISA processing across a specific laser fluence range. Allowing for a single variable, namely the silicon dioxide interlayer thickness to be investigated at a time. This was carried out simultaneously as both an experimental and theoretical investigation. The theoretical computational study showed that at specific silica thicknesses there was a significant increase in the absorption of the laser line in the silver thin film, while at opposing thicknesses, the inverse was true where the absorption in the silver film was minimised. These bands of high and low absorption of the laser line predicted in the theoretical calculations was matched perfectly by the modification of the annealing window at the corresponding thicknesses - high absorption in the silver leading to a narrowing and shifting to lower energies, while low absorption in the silver film shits the annealing window to higher energies. Further to this, analysis of nanoparticle templates with similar morphologies revealed that irrespective of the interlayer thickness, these templates had experienced comparable: absolute peak temperatures; cooling times; or time spent above the melting temperature of silver. The multiple reflections of the laser line within the silica film off us an additional level of control on the laser annealing process by allow the pre-determination of the level of absorption of the laser pulse in the silver film.

Similarly, to the previous chapter, chapter 7 addresses a peculiar phenomenon identified when viewing silicon / silicon dioxide / silver nanoparticle templates, at different angles of incidence or angles of illumination, where the samples appeared to change colour. This effect, like that of an opal, is one that to the best of the authors' knowledge cannot be accurately measured with any commercially available optical measurement system. Consequently, to fully analyse this effect, it was necessary to design, engineer and construct a system that would allow for this. The system was designed and built around a two-stage goniometric base comprising a sample stage and rotating detector arm, that can freely rotate 360° and a fixed position illumination arm. The illumination and detection arms deliver and acquire light through a fibre coupled collimating lens. Additionally, due to the polarisation dependence of reflectance at steep angles, such as angles above the *Brewster's angle*, the system was built to incorporate a linear polariser into both the illumination and detection arms. This custom-built system allows for the angle and polarisation dependent absolute reflectance or transmission of any given sample to be accurately and reliably measured. Measurements of silicon / silicon dioxide / silver nanoparticles at a range of angles, showed that the spectral position of the LSPR peak in S-polarisation shown no variation, the P-polarisation showed a clear blue-shift of the LSPR peak position at steeper angles. This effect can be attributed to two compound factors: the S-polarisation probing the $x - y$ place dimension of the nanoparticle template and having limited penetration into the silica interlayer; and the P-polarisation probing the z axis of the nanoparticles and having high penetration into the silica interlayer. We can therefore state that the colour change effect is due to the hemispherical shape of the individual nanoparticles and a thin film interference effect caused by the silica interlayer.

8.3 Future Prospects

As is the case with all research, answering one question often produces two more. Here we will present a possible route towards furthering the research presented here.

8.3.1 Naked nanoparticle monitoring

In chapter 4 we have presented the proof of principle of a novel approach to an existing sensing methodology. The lack of functionalisation offers far more than the simplification of sensor fabrication. The lack of specificity of the naked nanoparticle sensing surface means that a single sensing surface could be used to monitor the surface adsorption of multiple compounds with comparable levels of accuracy as shown here. This could provide the perfect *in situ* monitoring technique for assessing the uptake of a filtering medium. This work would require the investigation of the optical effect caused by the adsorption of multiple compounds individually onto a naked nanoparticle template, again, cross calibrating the optical response change to the measured surface abundance. Following this, there would need to be an investigation into the ability of a naked nanoparticle template to respond to multiple compound simultaneously - studying if these compounds can be individually identified. Finally, it would be necessary to investigate if a nanoparticle template produced on a filtration medium could be used for *in situ* monitoring.

8.3.2 The influence of an interlayer on laser annealing

Combining the insight gained from chapter 5 and 6, it may be possible to recreate the same quality off nanoparticle templates as seen on silicon on a polymer substrate. To this end, it would be necessary to recreate the multiple interfaces present in the silicon / silica / silver structure on a polymer substrate. This would require the inclusion of a back-reflector to be deposited onto the polymer. This new sample structure of polymer substrate / back-reflector / silica interlayer / silver thin film could allow us to exactly recreate the effects seen on silicon on a polymer. The material selected for the back reflector either silicon, to more accurately emulate the silicon situation, or aluminium, to maximise the reflection at the reflector / interlayer interface. The inclusion of the back-reflector into the sample structure could allow for an identical laser annealing process to be carried out on a rigid substrate as on a flexible substrate, resulting in the production of identical, high quality nanoparticle templates. If successful, even at lower laser fluences that those used on a true silicon substrate, would mark a key milestone towards the rapid and controllable process for flexible plasmonic devices and applications.

8.3.3 Angle and polarisation dependent reflectance

Chapter 7 describes not only a novel measurement technique but a viable route towards an *end - user* tuneable plasmonic surface. The optical response of a plasmonic nanostructures is dictated by the material, size, shape and surface coverage of the nanostructure the optical response is fixed. If for a given application or system such as a Raman microscope, a single user may require the use of multiple probing laser wavelengths and would equally require multiple SERS surfaces corresponding to each laser used. This however could be vastly simplified by instead using a single surface that can be positioned at a specific angle to achieve a desired LSPR peak wavelength. To achieve this several theoretical computational studies must be undertaken. Primarily, an investigation into the extent to which the nanostructures shape plays on the angle dependence of the reflectance - do nanoscale pillars offer a greater variation to the optical response than a hemispherical nanoparticle. Such a computational study could be used to guide an associated experimental program aiming to attempt to recreate the effect of an angle tuneable LSPR surface.

Bibliography

[1] JJ Mock, M Barbic, DR Smith, DA Schultz, and S Schultz. Shape effects in plasmon resonance of individual colloidal silver nanoparticles. *The Journal of Chemical Physics*, 116(15):6755–6759, 2002.

[2] Nikolaos A Vainos. *Laser growth and processing of photonic devices*. Elsevier, 2012.

[3] RH Ritchie. Plasma losses by fast electrons in thin films. *Physical Review*, 106(5):874, 1957.

[4] Mark Fox. Optical properties of solids, 2002.

[5] David B Tanner. Optical effects in solids. *Department of Physics, University of Florida, USA*, 2013.

[6] Stefan Alexander Maier. *Plasmonics: fundamentals and applications*. Springer Science & Business Media, 2007.

[7] Stefan A. Maier. *Fundamentals and Applications*, volume 8. 2015.

[8] M I Stockman, Katrin Kneipp, S I Bozhevolnyi, Saha S, and a Datta. Roadmap on plasmonics. *J. Opt.*, 20(2018):043001, 2018.

[9] Anatoly V Zayats, Igor I Smolyaninov, and Alexei A Maradudin. Nano-optics of surface plasmon polaritons. *Physics reports*, 408(3):131–314, 2005.

[10] P Cheyssac, VA Sterligov, SI Lysenko, and R Kofman. Surface plasmon-polaritons. *physica status solidi(a)*, 175(1):253–258, 1999.

[11] H Ditlbacher, JR Krenn, G Schider, A Leitner, and FR Aussenegg. Two-dimensional optics with surface plasmon polaritons. *Applied Physics Letters*, 81(10):1762–1764, 2002.

[12] Hyuk Rok Gwon and Seong Hyuk Lee. Spectral and angular responses of surface plasmon resonance based on the kretschmann prism configuration. *Materials transactions*, 51(6):1150–1155, 2010.

[13] Ryo Naraoka, Haruki Okawa, Kazuhiko Hashimoto, and Kotaro Kajikawa. Surface plasmon resonance enhanced second-harmonic generation in kretschmann configuration. *Optics communications*, 248(1):249–256, 2005.

[14] Heinz Raether. Surface plasmons on smooth surfaces. In *Surface plasmons on smooth and rough surfaces and on gratings*, pages 4–39. Springer, 1988.

[15] Emmanuel K Akowuah, Terry Gorman, and Shyqyri Haxha. Design and optimization of a novel surface plasmon resonance biosensor based on otto configuration. *Optics express*, 17(26):23511–23521, 2009.

[16] Gustav Mie. Beiträge zur optik trüber medien, speziell kolloidaler metallösungen. *Annalen der physik*, 330(3):377–445, 1908.

[17] Stefan A Maier and Harry A Atwater. Plasmonics: Localization and guiding of electromagnetic energy in metal/dielectric structures. *Journal of applied physics*, 98(1):10, 2005.

[18] Stefan A Maier, Mark L Brongersma, Pieter G Kik, Scheffer Meltzer, Ari AG Requicha, and Harry A Atwater. Plasmonics—a route to nanoscale optical devices. *Advanced Materials*, 13(19):1501–1505, 2001.

[19] K. Lance Kelly, Eduardo Coronado, Lin Lin Zhao, and George C. Schatz. The Optical Properties of Metal Nanoparticles: The Influence of Size, Shape, and Dielectric Environment. *The Journal of Physical Chemistry B*, 107(3):668–677, 2003.

[20] Traci R Jensen, Michelle Duval Malinsky, Christy L Haynes, and Richard P Van Duyne. Nanosphere lithography: tunable localized surface plasmon resonance spectra of silver nanoparticles. *The Journal of Physical Chemistry B*, 104(45):10549–10556, 2000.

[21] Jennifer A Dionne and Harry A Atwater. Plasmonics: metal-worthy methods and materials in nanophotonics. *MRS Bulletin*, 37(8):717–724, 2012.

[22] S Pillai and MA Green. Plasmonics for photovoltaic applications. *Solar Energy Materials and Solar Cells*, 94(9):1481–1486, 2010.

[23] KR Catchpole and Albert Polman. Plasmonic solar cells. *Optics express*, 16(26):21793–21800, 2008.

[24] Naveen Gandra, Christopher Portz, Saide Z Nergiz, Andrew Fales, Tuan Vo-Dinh, and Srikanth Singamaneni. Inherently stealthy and highly tumor-selective gold nanoraspberries for photothermal cancer therapy. *Scientific reports*, 5:10311, 2015.

[25] Xiaohua Huang, Prashant K Jain, Ivan H El-Sayed, and Mostafa A El-Sayed. Plasmonic photothermal therapy (pptt) using gold nanoparticles. *Lasers in medical science*, 23(3):217, 2008.

[26] Alessandro Ciattoni, Carlo Rizza, and Elia Palange. All-optical active plasmonic devices with memory and power-switching functionalities based on ε-near-zero nonlinear metamaterials. *Physical Review A*, 83(4):043813, 2011.

[27] Alexandros Emboras, Ilya Goykhman, Boris Desiatov, Noa Mazurski, Liron Stern, Joseph Shappir, and Uriel Levy. Nanoscale plasmonic memristor with optical readout functionality. *Nano letters*, 13(12):6151–6155, 2013.

[28] Zhanghua Han and Sergey I Bozhevolnyi. Radiation guiding with surface plasmon polaritons. *Reports on Progress in Physics*, 76(1):016402, 2012.

[29] Zhanghua Han and Sergey I. Bozhevolnyi. Radiation guiding with surface plasmon polaritons. *Reports on Progress in Physics*, 76(1), 2013.

[30] Rupert F Oulton, Volker J Sorger, DA Genov, DFP Pile, and X Zhang. A hybrid plasmonic waveguide for subwavelength confinement and long-range propagation. *Nature Photonics*, 2(8):496–500, 2008.

[31] Mark I Stockman. Nanofocusing of optical energy in tapered plasmonic waveguides. *Physical review letters*, 93(13):137404, 2004.

[32] Arnaldo D'Amico and Corrado Di Natale. A contribution on some basic definitions of sensors properties. *IEEE Sensors Journal*, 1(3):183–190, 2001.

[33] Stefan A Maier. Plasmonic field enhancement and sers in the effective mode volume picture. *Optics Express*, 14(5):1957–1964, 2006.

[34] Andreas Otto, I Mrozek, H Grabhorn, and W Akemann. Surface-enhanced raman scattering. *Journal of Physics: Condensed Matter*, 4(5):1143, 1992.

[35] Gary A Baker and David S Moore. Progress in plasmonic engineering of surface-enhanced raman-scattering substrates toward ultra-trace analysis. *Analytical and bioanalytical chemistry*, 382(8):1751–1770, 2005.

[36] Alan Campion and Patanjali Kambhampati. Surface-enhanced raman scattering. *Chemical society reviews*, 27(4):241–250, 1998.

[37] Jian Feng Li, Yi Fan Huang, Yong Ding, Zhi Lin Yang, Song Bo Li, Xiao Shun Zhou, Feng Ru Fan, Wei Zhang, Zhi You Zhou, Bin Ren, et al. Shell-isolated nanoparticle-enhanced raman spectroscopy. *nature*, 464(7287):392–395, 2010.

[38] Martin Moskovits. Surface-enhanced raman spectroscopy: a brief retrospective. *Journal of Raman Spectroscopy*, 36(6-7):485–496, 2005.

[39] Katrin Kneipp, Yang Wang, Harald Kneipp, Lev T Perelman, Irving Itzkan, Ramachandra R Dasari, and Michael S Feld. Single molecule detection using surface-enhanced raman scattering (sers). *Physical review letters*, 78(9):1667, 1997.

[40] Hongxing Xu, Javier Aizpurua, Mikael Käll, and Peter Apell. Electromagnetic contributions to single-molecule sensitivity in surface-enhanced raman scattering. *Physical Review E*, 62(3):4318, 2000.

[41] Katrin Kneipp, Harald Kneipp, and Henrik Bohr. Single-molecule sers spectroscopy. *Surface-Enhanced Raman Scattering*, pages 261–277, 2006.

[42] Chad A Mirkin, Robert L Letsinger, Robert C Mucic, and James J Storhoff. A dna-based method for rationally assembling nanoparticles into macroscopic materials. *Nature*, 382(6592):607–609, 1996.

[43] Nathaniel L Rosi and Chad A Mirkin. Nanostructures in biodiagnostics. *Chemical reviews*, 105(4):1547–1562, 2005.

[44] Jeffrey N Anker, W Paige Hall, Mary P Lambert, Pauline T Velasco, Milan Mrksich, William L Klein, and Richard P Van Duyne. Detection and identification of bioanalytes with high resolution lspr spectroscopy and maldi mass spectrometry. *The Journal of Physical Chemistry C*, 113(15):5891–5894, 2009.

[45] Kazuhiko Fujiwara, Hitoshi Watarai, Hideaki Itoh, Erika Nakahama, and Nobuaki Ogawa. Measurement of antibody binding to protein immobilized on gold nanoparticles by localized surface plasmon spectroscopy. *Analytical and bioanalytical chemistry*, 386(3):639–644, 2006.

[46] Katherine A Willets and Richard P Van Duyne. Localized surface plasmon resonance spectroscopy and sensing. *Annu. Rev. Phys. Chem.*, 58:267–297, 2007.

[47] Matthew E Stewart, Christopher R Anderton, Lucas B Thompson, Joana Maria, Stephen K Gray, John A Rogers, and Ralph G Nuzzo. Nanostructured plasmonic sensors. *Chemical reviews*, 108(2):494–521, 2008.

[48] Jiří Homola. Present and future of surface plasmon resonance biosensors. *Analytical and bioanalytical chemistry*, 377(3):528–539, 2003.

[49] Jiřı Homola, Sinclair S Yee, and Günter Gauglitz. Surface plasmon resonance sensors. *Sensors and Actuators B: Chemical*, 54(1):3–15, 1999.

[50] Priyabrata Pattnaik. Surface plasmon resonance. *Applied biochemistry and biotechnology*, 126(2):79–92, 2005.

[51] TheEmergingFuture.com. Estimating the Speed of Exponential Technological Advancement. 2012.

[52] Edward D Wolf. Nanofabrication: Opportunities for Interdisciplinary Research. *Microelectronic Engineeering*, 9, 1989.

[53] KL Lee and H Ahmed. An e-beam microfabrication system for nanolithography. *Journal of Vacuum Science and Technology*, 19(4):946–949, 1981.

[54] KL Lee and H Ahmed. Fabrication of nanometer metal structures by a combination of techniques of metal evaporation and e-beam nanolithography. *IEEE Electron Device Letters*, 4(7):243–245, 1983.

[55] T Tamamura, K Sukegawa, and S Sugawara. Resolution limit of negative electron resist exposed on a thin film substrate. *Journal of The Electrochemical Society*, 129(8):1831–1835, 1982.

[56] MS Isaacson and A Muray. Nanolithography using in situ electron beam vaporization of very low molecular weight resists. In *Workshop on Molecular Electronic Devices, Naval Research Laboratory (March 23–24, 1981)*, 1981.

[57] David C Joy. The spatial resolution limit of electron lithography. *Microelectronic Engineering*, 1(2):103–119, 1983.

[58] David F Kyser. Spatial resolution limits in electron beam nanolithography. *Journal of Vacuum Science & Technology B: Microelectronics Processing and Phenomena*, 1(4):1391–1397, 1983.

[59] Y N Xia and G M Whitesides. Soft lithography. *Annual Review Of Materials Science*, 37(5):551–575, 1998.

[60] HW Deckman and JH Dunsmuir. Natural lithography. *Applied Physics Letters*, 41(4):377–379, 1982.

[61] Seung-Man Yang, Se Gyu Jang, Dae-Geun Choi, Sarah Kim, and Hyung Kyun Yu. Nanomachining by colloidal lithography. *small*, 2(4):458–475, 2006.

[62] Amar B Pawar and Ilona Kretzschmar. Fabrication, assembly, and application of patchy particles. *Macromolecular rapid communications*, 31(2):150–168, 2010.

[63] B. J Y Tan, C. H. Sow, K. Y. Lim, F. C. Cheong, G. L. Chong, A. T S Wee, and C. K. Ong. Fabrication of a two-dimensional periodic non-close-packed array of polystyrene particles. *Journal of Physical Chemistry B*, 108(48):18575–18579, 2004.

[64] V Ng, YV Lee, BT Chen, and AO Adeyeye. Nanostructure array fabrication with temperature-controlled self-assembly techniques. *Nanotechnology*, 13(5):554–558, 2002.

[65] Anjeanette D. Ormonde, Erin C.M. Hicks, Jimmy Castillo, and Richard P. Van Duyne. Nanosphere lithography: Fabrication of large-area Ag nanoparticle arrays by convective self-assembly and their characterization by scanning UV - Visible extinction spectroscopy. *Langmuir*, 20(16):6927–6931, 2004.

[66] Paulina A Rincon Delgadillo, Roel Gronheid, Christopher J Thode, Hengpeng Wu, Yi Cao, Mark Neisser, Mark Somervell, Kathleen Nafus, and Paul F Nealey. Implementation of a chemo-epitaxy flow for directed self-assembly on 300-mm wafer processing equipment. *Journal of Micro/Nanolithography, MEMS, and MOEMS*, 11(3):031302–1, 2012.

[67] Hongyou Fan, Yunfeng Lu, Aaron Stump, Scott T. Reed, Tom Baer, Randy Schunk, Victor Perez-Luna, Gabriel P. López, and C. Jeffrey Brinker. Rapid prototyping of patterned functional nanostructures. *Nature*, 405(6782):56–60, 2000.

[68] Robert Brunner, Oliver Sandfuchs, Claudia Pacholski, Christoph Morhard, and Joachim Spatz. Lessons from nature: biomimetic subwavelength structures for high-performance optics. *Laser & Photonics Reviews*, 6(5):641–659, 2012.

[69] Ray C Schmidt and Kevin E Healy. Controlling biological interfaces on the nanometer length scale. *Journal of Biomedical Materials Research Part A*, 90(4):1252–1261, 2009.

[70] Lin Jiang, Xiaodong Chen, Nan Lu, and Lifeng Chi. Spatially confined assembly of nanoparticles. *Accounts of Chemical Research*, 47(10):3009–3017, 2014.

[71] C. H. Chang, L. Tian, W. R. Hesse, H. Gao, H. J. Choi, J. G. Kim, M. Siddiqui, and G. Barbastathis. From two-dimensional colloidal self-assembly to three-dimensional nanolithography. *Nano Letters*, 11(6):2533–2537, 2011.

[72] Jason D. Fowlkes, Lou Kondic, Javier Diez, Yueying Wu, and Philip D. Rack. Self-assembly versus directed assembly of nanoparticles via pulsed laser induced dewetting of patterned metal films. *Nano Letters*, 11(6):2478–2485, 2011.

[73] Chengxiang Xiang, Michael A. Thompson, Fan Yang, Erik J. Menke, Li Mei C Yang, and Reginald M. Penner. Lithographically patterned nanowire electrodeposition. *Physica Status Solidi (C) Current Topics in Solid State Physics*, 5(11):3503–3505, 2008.

[74] DV Korobkin and E Yablonovitch. Two-fold spatial resolution enhancement by two-photon exposure of the photographic film. In *Lasers and Electro-Optics, 2001. CLEO'01. Technical Digest. Summaries of papers presented at the Conference on*, pages 434–435. IEEE, 2001.

[75] Henry E Williams, Daniel J Freppon, Stephen M Kuebler, Raymond C Rumpf, and Marco A Melino. Fabrication of three-dimensional micro-photonic structures on the tip of optical fibers using su-8. *Optics express*, 19(23):22910–22922, 2011.

[76] Vaida Auzelyte, Christian Dais, Patrick Farquet, Detlev Grützmacher, Laura J Heyderman, Feng Luo, Sven Olliges, Celestino Padeste, Pratap K Sahoo, Tom Thomson, et al. Extreme ultraviolet interference lithography at the paul scherrer institut. *Journal of Micro/Nanolithography, MEMS, and MOEMS*, 8(2):021204–021204, 2009.

[77] J Ullrich, R Moshammer, A N Perumal, and R Moshammer. Reports on Progress in Physics Related content Recoil-ion and electron momentum spectroscopy : Recoil-ion and electron momentum spectroscopy :. 2003.

[78] Avanish Kumar Dubey and Vinod Yadava. Laser beam machining-A review. *International Journal of Machine Tools and Manufacture*, 48(6):609–628, 2008.

[79] Anoop N. Samant and Narendra B. Dahotre. Laser machining of structural ceramics-A review. *Journal of the European Ceramic Society*, 29(6):969–993, 2009.

[80] Jörg Krüger and Wolfgang Kautek. Ultrashort pulse laser interaction with dielectrics and polymers. *polymers and light*, pages 247–290, 2004.

[81] Sanjay Kumar. Selective laser sintering: a qualitative and objective approach. *JOM Journal of the Minerals, Metals and Materials Society*, 55(10):43–47, 2003.

[82] B. N. Chichkov, C. Momma, S. Nolte, F. von Alvensleben, and A. Tünnermann. Femtosecond, picosecond and nanosecond laser ablation of solids. *Applied Physics A: Materials Science & Processing*, 63(2):109–115, 1996.

[83] Alfredo M Morales and Charles M Lieber. A Laser Ablation Method for the Synthesis of Crystalline Semiconductor Nanowires Author (s): Alfredo M . Morales and Charles M . Lieber Published by : American Association for the Advancement of Science Stable URL : http://www.jstor.org/stable/2893988 R. 279(5348):208–211, 2016.

[84] Evans Chikarakara, Sumsun Naher, and Dermot Brabazon. Analysis of Microstructural Changes during Pulsed CO2 Laser Surface Processing of AISI 316L Stainless Steel. *Advanced Materials Research*, 264-265:1401–1408, 2011.

[85] Wolfgang Kautek and Jörg Krüger. Femtosecond pulse laser ablation of metallic, semiconducting, ceramic, and biological materials. In *Proc. SPIE*, volume 2207, pages 600–610, 1994.

[86] J Ihlemann, A Scholl, H Schmidt, and B Wolff-Rottke. Nanosecond and femtosecond excimer-laser ablation of oxide ceramics. *Applied Physics A: Materials Science & Processing*, 60(4):411–417, 1995.

[87] R. Srinivasan and Bodil Braren. Ultraviolet Laser Ablation of Organic Polymers. *Chemical Reviews*, 89(6):1303–1316, 1989.

[88] R Srinivasan. Ablation of polymers and biological tissue by ultraviolet lasers. *Science*, 234:559–566, 1986.

[89] FE Livingston, LF Steffeney, and H Helvajian. Genotype-inspired laser material processing: a new experimental approach and potential applications to protean materials. *Applied Physics A*, 93(1):75, 2008.

[90] V Craciun and RK Singh. Characteristics of the surface layer of barium strontium titanate thin films deposited by laser ablation. *Applied Physics Letters*, 76(14):1932–1934, 2000.

[91] JM Ballesteros, R Serna, J Solıs, CN Afonso, AK Petford-Long, DH Osborne, and RF Haglund Jr. Pulsed laser deposition of cu: Al 2 o 3 nanocrystal thin films with high third-order optical susceptibility. *Applied physics letters*, 71(17):2445–2447, 1997.

[92] Choong-Rae Cho and Alex Grishin. Self-assembling ferroelectric na 0.5 k 0.5 nbo 3 thin films by pulsed-laser deposition. *Applied physics letters*, 75(2):268–270, 1999.

[93] Marc Ullmann, Sheldon K Friedlander, and Andreas Schmidt-Ott. Nanoparticle formation by laser ablation. *Journal of Nanoparticle Research*, 4(6):499–509, 2002.

[94] Zoltán Pászti, Zsolt E Horváth, Gábor Pető, Albert Karacs, and L Guczi. Nanoparticle formation during laser ablation. In *Solid State Phenomena*, volume 56, pages 207–212. Trans Tech Publ, 1997.

[95] Fumitaka Mafuné, Jun-ya Kohno, Yoshihiro Takeda, Tamotsu Kondow, and Hisahiro Sawabe. Formation and size control of silver nanoparticles by laser ablation in aqueous solution. *The Journal of Physical Chemistry B*, 104(39):9111–9117, 2000.

[96] Fumitaka Mafuné, Jun-ya Kohno, Yoshihiro Takeda, Tamotsu Kondow, and Hisahiro Sawabe. Formation of gold nanoparticles by laser ablation in aqueous solution of surfactant. *The Journal of Physical Chemistry B*, 105(22):5114–5120, 2001.

[97] SF Lombardo, S Boninelli, F Cristiano, G Fisicaro, G Fortunato, MG Grimaldi, G Impellizzeri, M Italia, A Marino, R Milazzo, et al. Laser annealing in si and ge: Anomalous physical aspects and modeling approaches. *Materials Science in Semiconductor Processing*, 62:80–91, 2017.

[98] S. Link, C. Burda, B. Nikoobakht, and M. a. El-Sayed. Laser-Induced Shape Changes of Colloidal Gold Nanorods Using Femtosecond and Nanosecond Laser Pulses. *Journal of Physical Chemistry B*, 104(26):6152–6163, 2000.

[99] Fumitaka Mafuné, Jun-ya Kohno, Yoshihiro Takeda, and Tamotsu Kondow. Full physical preparation of size-selected gold nanoparticles in solution: laser ablation and laser-induced size control. *The Journal of Physical Chemistry B*, 106(31):7575–7577, 2002.

[100] Vincenzo Amendola and Moreno Meneghetti. Laser ablation synthesis in solution and size manipulation of noble metal nanoparticles. *Physical chemistry chemical physics*, 11(20):3805–3821, 2009.

[101] Saurabh Saxena and Jin Jang. Rapid-thermal annealing of amorphous silicon on oxide semiconductors. *IEICE Transactions on Electronics*, 93(10):1495–1498, 2010.

[102] Yang Lu, Hui Zhang, and Ting Mei. The influence of rapid thermal annealing processed metal-semiconductor contact on plasmonic waveguide under electrical pumping. *Journal of the Optical Society of Korea*, 20(1):130–134, 2016.

[103] R Stanowski and JJ Dubowski. Laser rapid thermal annealing of quantum semiconductor wafers: a one step bandgap engineering technique. *Applied Physics A: Materials Science & Processing*, 94(3):667–674, 2009.

[104] AK Baker and PE Dyer. Refractive-index modification of polymethylmethacrylate (pmma) thin films by krf-laser irradiation. *Applied Physics A: Materials Science & Processing*, 57(6):543–544, 1993.

[105] GR Levinson and VI Smilga. Laser processing of thin films. *Soviet Journal of Quantum Electronics*, 6(8):885, 1976.

[106] Ian W Boyd. *Laser processing of thin films and microstructures: oxidation, deposition and etching of insulators*, volume 3. Springer Science & Business Media, 2013.

[107] Byoung Hun Lee, Laegu Kang, Renee Nieh, Wen-Jie Qi, and Jack C Lee. Thermal stability and electrical characteristics of ultrathin hafnium oxide gate dielectric reoxidized with rapid thermal annealing. *Applied Physics Letters*, 76(14):1926–1928, 2000.

[108] Eric Verploegen, Rajib Mondal, Christopher J Bettinger, Seihout Sok, Michael F Toney, and Zhenan Bao. Effects of thermal annealing upon the morphology of polymer–fullerene blends. *Advanced Functional Materials*, 20(20):3519–3529, 2010.

[109] Karim Huet, Fulvio Mazzamuto, Toshiyuki Tabata, Ines Toque-Tresonne, and Yoshihiro Mori. Doping of semiconductor devices by laser thermal annealing. *Materials Science in Semiconductor Processing*, 62:92–102, 2017.

[110] Clara Goyes, Maurizio Ferrari, Cristina Armellini, Alessandro Chiasera, Yoann Jestin, Giancarlo C Righini, Faruk Fonthal, and Efraín Solarte. Co 2 laser annealing on erbium-activated glass–ceramic waveguides for photonics. *Optical Materials*, 31(9):1310–1314, 2009.

[111] N Misra, L Xu, MS Rogers, SH Ko, and CP Grigoropoulos. Pulsed laser annealing of semiconductor structures for functional devices. *physica status solidi (c)*, 5(10):3264–3270, 2008.

[112] Toshio Joshua Kudo. Double-pulsed laser annealing technologies and related applications. In *Advanced Thermal Processing of Semiconductors, 2006. RTP'06. 14th IEEE International Conference on*, pages 21–29. IEEE, 2006.

[113] Kiyotaka Wasa, Isaku Kanno, and Hidetoshi Kotera. *Handbook of sputter deposition technology: fundamentals and applications for functional thin films, nano-materials and MEMS.* William Andrew, 2012.

[114] Bernhard Wolf. *Handbook of ion sources.* CRC press, 2017.

[115] Donald M. Mattox. *The Foundations of Vacuum Coating Technology.* 2003.

[116] John A. Thornton. Influence of apparatus geometry and deposition conditions on the structure and topography of thick sputtered coatings. *Journal of Vacuum Science and Technology*, 11(4):666–670, 1974.

[117] Milton Ohring. *Materials science of thin films.* Elsevier, 2001.

[118] John A Thornton. Influence of apparatus geometry and deposition conditions on the structure and topography of thick sputtered coatings. *Journal of Vacuum Science and Technology*, 11(4):666–670, 1974.

[119] Joseph Blanc. A revised model for the oxidation of si by oxygen. *Applied Physics Letters*, 33(5):424–426, 1978.

[120] Mingchao Liu, Peng Jin, Zhiping Xu, Dorian AH Hanaor, Yixiang Gan, and Changqing Chen. Two-dimensional modeling of the self-limiting oxidation in silicon and tungsten nanowires. *Theoretical and Applied Mechanics Letters*, 6(5):195–199, 2016.

[121] August George. Moscap oxide charges. 2015.

[122] Chao Lu and Alvin Warren Czanderna. *Applications of piezoelectric quartz crystal microbalances*, volume 7. Elsevier, 2012.

[123] Diethelm Johannsmann. *The Quartz Crystal Microbalance in Soft Matter Research*. Springer, 2014.

[124] Günter Sauerbrey. Verwendung von schwingquarzen zur wägung dünner schichten und zur mikrowägung. *Zeitschrift für physik*, 155(2):206–222, 1959.

[125] A Arnau, T Sogorb, and Y Jimenez. Qcm100-quartz crystal microbalance theory and calibration. *Rev. Sci. Instrum*, 71:2563, 2000.

[126] Oliver S Heavens. *Optical properties of thin solid films*. Courier Corporation, 1991.

[127] DG Stavenga. Thin film and multilayer optics cause structural colors of many insects and birds. *Mater. Today*, 1(Suppl 1):109–121, 2014.

[128] Nikolaos Kalfagiannis, Anastasios Siozios, Dimitris V. Bellas, Dimosthenis Toliopoulos, Leon Bowen, Nikolaos Pliatsikas, Wayne M. Cranton, Constantinos Kosmidis, Demosthenes C. Koutsogeorgis, Elefterios Lidorikis, and Panos Patsalas. Selective modification of nanoparticle arrays by laser-induced self assembly (MONA-LISA): putting control into bottom-up plasmonic nanostructuring. *Nanoscale*, 8(15):8236–8244, 2016.

[129] D. V. Bellas, D. Toliopoulos, N. Kalfagiannis, A. Siozios, P. Nikolaou, P. C. Kelires, D. C. Koutsogeorgis, P. Patsalas, and E. Lidorikis. Simulating the opto-thermal processes involved in laser induced self-assembly of surface and sub-surface plasmonic nano-structuring. *Thin Solid Films*, 630:7–24, 2017.

[130] SJ Henley, JD Carey, and SRP Silva. Pulsed-laser-induced nanoscale island formation in thin metal-on-oxide films. *Physical Review B*, 72(19):195408, 2005.

[131] Thomas R Powers and Raymond E Goldstein. Pearling and pinching: propagation of rayleigh instabilities. *Physical review letters*, 78(13):2555, 1997.

[132] ME Toimil Molares, AG Balogh, TW Cornelius, R Neumann, and C Trautmann. Fragmentation of nanowires driven by rayleigh instability. *Applied physics letters*, 85(22):5337–5339, 2004.

[133] Daniel L Flamm and Orlando Auciello. *Plasma deposition, treatment, and etching of polymers: the treatment and etching of polymers.* Elsevier, 2012.

[134] John W Coburn and Harold F Winters. Ion-and electron-assisted gas-surface chemistry—an important effect in plasma etching. *Journal of Applied physics*, 50(5):3189–3196, 1979.

[135] A. Siozios, N. Kalfagiannis, D.V. Bellas, C. Bazioti, G.P. Dimitrakopulos, G. Vourlias, W.M. Cranton, E. Lidorikis, D.C. Koutsogeorgis, and P. Patsalas. Sub-surface laser nanostructuring in stratified metal/dielectric media: A versatile platform towards flexible, durable and large-scale plasmonic writing. *Nanotechnology*, 26(15):155301, 2015.

[136] Dennis M Sullivan. *Electromagnetic simulation using the FDTD method.* John Wiley & Sons, 2013.

[137] Kane Yee. Numerical solution of initial boundary value problems involving maxwell's equations in isotropic media. *IEEE Transactions on antennas and propagation*, 14(3):302–307, 1966.

[138] Ewen Smith and Geoffrey Dent. *Modern Raman spectroscopy: a practical approach.* John Wiley & Sons, 2013.

[139] Jiři Homola, Sinclair S. Yee, and Günter Gauglitz. Surface plasmon resonance sensors: review. *Sensors and Actuators B: Chemical*, 54(1):3–15, 1999.

[140] Giuseppe V. Bianco, Maria Losurdo, Maria M. Giangregorio, Pio Capezzuto, and Giovanni Bruno. Direct Fabrication Route to Plastic-Supported Gold Nanoparticles for Flexible NIR-SERS. *Plasmonics*, 8(1):159–165, 2013.

[141] Chang H Lee, Mikella E Hankus, Limei Tian, Paul M Pellegrino, and Srikanth Singamaneni. Highly Sensitive Surface Enhanced Raman Scattering Substrates. *Analytical chemistry*, 83(23):8953–8958, 2011.

[142] Dian He, Bo Hu, Qiao-feng Yao, Kan Wang, and Shu-hong Yu. Large-Scale Synthesis of Flexible Free- Sensitivity : Electrospun PVA Nanofibers of Silver Nanoparticles. *ACS Nano*, 3(12):3993–4002, 2009.

[143] Aram J Chung, Yun Suk Huh, and David Erickson. Large area flexible SERS active substrates using engineered nanostructures. *Nanoscale*, 3(7):2903–2908, 2011.

[144] R Gupta and WA Weimer. High enhancement factor gold films for surface enhanced raman spectroscopy. *Chemical physics letters*, 374(3-4):302–306, 2003.

[145] Joseph I Goldstein, Dale E Newbury, Joseph R Michael, Nicholas WM Ritchie, John Henry J Scott, and David C Joy. *Scanning electron microscopy and X-ray microanalysis*. Springer, 2017.

[146] David Briggs. Handbook of x-ray photoelectron spectroscopy cd wanger, wm riggs, le davis, jf moulder and ge muilenberg perkin-elmer corp., physical electronics division, eden prairie, minnesota, usa, 1979. 190 pp. 195.$SurfaceandInterfaceAnalysis, 3(4) : v - -v, 1981$.

[147] Albert Einstein. Concerning an heuristic point of view toward the emission and transformation of light. *American Journal of Physics*, 33(5):367, 1965.

[148] Richard P Van Duyne, Amanda J Haes, and Adam D McFarland. Nanoparticle optics: sensing with nanoparticle arrays and single nanoparticles. In *Proceedings of SPIE*, volume 5223, pages 197–207, 2003.

[149] Isabella Dalle-Donne, Ranieri Rossi, Daniela Giustarini, Aldo Milzani, and Roberto Colombo. Protein carbonyl groups as biomarkers of oxidative stress. *Clinica Chimica Acta*, 329(1-2):23–38, 2003.

[150] T Klar, M Perner, S Grosse, G Von Plessen, W Spirkl, and J Feldmann. Surface-plasmon resonances in single metallic nanoparticles. *Physical Review Letters*, 80(19):4249, 1998.

[151] R. P. Sagle, L. B.; Ruvuna, L. K.; Ruemmele, J. A.; Van Duyne. Advances in localized surface plasmon resonance spectroscopy biosensing. *Nanomedicine*, pages 1447 – 1462, 2011.

[152] Wanbo Li, Yongcai Qiu, Li Zhang, Lelun Jiang, Zhangkai Zhou, Huanjun Chen, and Jianhua Zhou. Aluminum nanopyramid array with tunable ultraviolet-visible-infrared wavelength plasmon resonances for rapid detection of carbohydrate antigen 199. *Biosensors and Bioelectronics*, 79:500–507, 2016.

[153] Shuyan Gao, Naoto Koshizaki, Emiko Koyama, Hideo Tokuhisa, Takeshi Sasaki, Jae Kwan Kim, Youngsong Cho, Deok Soo Kim, and Yoshiki Shimizu. Innovative platform for transmission localized surface plasmon transducers and its application in detecting heavy metal Pd(II). *Analytical Chemistry*, 81(18):7703–7712, 2009.

[154] George H Chan, Jing Zhao, George C Schatz, and Richard P Van Duyne. Localized Surface Plasmon Resonance Spectroscopy of Triangular Aluminum Nanoparticles. *Journal of Physical Chemistry C*, pages 13958–13963, 2008.

[155] Richard P. Van Duyne Adam D. McFarland. Single Silver Nanoparticles As Real Time Optical Sensors With Zeptomole Sensitivity. *Nano Letters,*, 3:1057–1062., 2003.

[156] Yap Wing Fen and W. Mahmood Mat Yunus. Surface plasmon resonance spectroscopy as an alternative for sensing heavy metal ions: a review. *Sensor Review*, 33(4):305–314, 2013.

[157] Harvey Marcovitch. *Black's medical dictionary.* A&C Black, 2005.

[158] K D Esmeryan, G McHale, C L Trabi, N R Geraldi, and M I Newton. Manipulated wettability of a superhydrophobic quartz crystal microbalance through electrowetting. *Journal of Physics D: Applied Physics*, 46(34):345307, 2013.

[159] Hideyuki Nakanishi, Kyle J M Bishop, Bartlomiej Kowalczyk, Abraham Nitzan, Emily A. Weiss, Konstantin V Tretiakov, Mario M Apodaca, Rafal Klajn, J Fraser Stoddart, and Bartosz A. Grzybowski. Photoconductance and inverse photoconductance in films of functionalized metal nanoparticles. *Nature*, 460(7253):371–375, 2009.

[160] Lakshminarayana Polavarapu and Luis M Liz-Marzán. Towards low-cost flexible substrates for nanoplasmonic sensing. *Physical Chemistry Chemical Physics*, 15(15):5288–300, 2013.

[161] Yuefan Wei, Lin Ke, Junhua Kong, Hong Liu, Zhihui Jiao, Xuehong Lu, Hejun Du, and Xiao Wei Sun. Enhanced photoelectrochemical water-splitting effect with a bent ZnO nanorod photoanode decorated with Ag nanoparticles. *Nanotechnology*, 23(23):235401, 2012.

[162] Thomas D. Lazzara, Gilles R. Bourret, R. Bruce Lennox, and Theo G M Van De Ven. Polymer templated synthesis of AgCN and Ag nanowires. *Chemistry of Materials*, 21(10):2020–2026, 2009.

[163] Akram Boukai. High E ffi ciency Thin Upgraded Metallurgical-Grade Silicon Solar Cells on Flexible Substrates. 2012.

[164] Nikolaus Meyerbröker, Thomas Kriesche, and Michael Zharnikov. Novel ultrathin poly(ethylene glycol) films as flexible platform for biological applications and plasmonics. *ACS Applied Materials and Interfaces*, 5(7):2641–2649, 2013.

[165] Disney. Disney Magic Bands.

[166] Han Zhu, Ming Liang Du, Ming Zhang, Pan Wang, Shi Yong Bao, Meiling Zou, Ya Qin Fu, and Ju Ming Yao. Self-assembly of various Au nanocrystals on functionalized water-stable PVA/PEI nanofibers: A highly efficient surface-enhanced Raman scattering substrates with high density of "hot" spots. *Biosensors and Bioelectronics*, 54:91–101, 2014.

[167] Gerasimos Konstantatos and EH Sargent. Nanostructured materials for photon detection. *Nature nanotechnology*, 5(6):391–400, 2010.

[168] Oscar Vazquez-Mena, Takumi Sannomiya, Mahmut Tosun, Luis G. Villanueva, Veronica Savu, Janos Voros, and Juergen Brugger. High-resolution resistless nanopatterning on polymer and flexible substrates for plasmonic biosensing using stencil masks. *ACS Nano*, 6(6):5474–5481, 2012.

[169] Yaowu Hu, Prashant Kumar, Rong Xu, Kejie Zhao, and Gary J Cheng. Ultrafast direct fabrication of flexible substrate-supported designer plasmonic nanoarrays. *Nanoscale*, 8(1):172–182, 2015.

[170] Hyelim Kang, Chul Joon Heo, Hwan Chul Jeon, Su Yeon Lee, and Seung Man Yang. Durable plasmonic cap arrays on flexible substrate with real-time optical tunability for high-fidelity SERS devices. *ACS Applied Materials and Interfaces*, 5(11):4569–4574, 2013.

[171] Takumi Sannomiya, Christian Hafner, and Janos Vörös. Strain mapping with optically coupled plasmonic particles embedded in a flexible substrate. *Optics letters*, 34(13):2009–11, 2009.

[172] Robin M. Cole, Sumeet Mahajan, and Jeremy J. Baumberg. Stretchable metal-elastomer nanovoids for tunable plasmons. *Applied Physics Letters*, 95(15):3–6, 2009.

[173] Andrea Di Falco, Martin Ploschner, and Thomas F. Krauss. Flexible metamaterials at visible wavelengths. *New Journal of Physics*, 12, 2010.

[174] Xiaolong Zhu, Lei Shi, Xiaohan Liu, Jian Zi, and Zhenlin Wang. A mechanically tunable plasmonic structure composed of a monolayer array of metal-capped colloidal spheres on an elastomeric substrate. *Nano Research*, 3(11):807–812, 2010.

[175] Li Fan, Leo T. Varghese, Yi Xuan, Jian Wang, Ben Niu, and Minghao Qi. Direct fabrication of silicon photonic devices on a flexible platform and its application for strain sensing. *Optics Express*, 20(18):20564, 2012.

[176] Matthew G. Millyard, Fu Min Huang, Richard White, Elisabetta Spigone, Jani Kivioja, and Jeremy J. Baumberg. Stretch-induced plasmonic anisotropy of self-assembled gold nanoparticle mats. *Applied Physics Letters*, 100(7):2012–2015, 2012.

[177] Ch Sargentis, K. Giannakopoulos, A. Travlos, and D. Tsamakis. Fabrication and electrical characterization of a MOS memory device containing self-assembled metallic nanoparticles. *Physica E: Low-Dimensional Systems and Nanostructures*, 38(1-2):85–88, 2007.

[178] Harry A Atwater and Albert Polman. Plasmonics for improved photovoltaic devices. *Nat. Mater.*, 9(10):865–865, 2010.

[179] Mya Mya Khin, A. Sreekumaran Nair, V. Jagadeesh Babu, Rajendiran Murugan, and Seeram Ramakrishna. A review on nanomaterials for environmental remediation. *Energy & Environmental Science*, 5(8):8075, 2012.

[180] Hye Jin Lee, Alastair W. Wark, and Robert M. Corn. Enhanced bioaffinity sensing using surface plasmons, surface enzyme reactions, nanoparticles and diffraction gratings. *The Analyst*, 133(5):596, 2008.

[181] Amy M. Michaels, M. Nirmal, and L. E. Brus. Surface enhanced Raman spectroscopy of individual rhodamine 6G molecules on large Ag nanocrystals. *Journal of the American Chemical Society*, 121(43):9932–9939, 1999.

[182] Jennifer A. Dionne and Harry A. Atwater. Plasmonics: Metal-worthy methods and materials in nanophotonics. *MRS Bulletin*, 37(08):717–724, 2012.

[183] Pablo Albella, Borja Garcia-cueto, Francisco Gonz, Fernando Moreno, Pae C Wu, Tong-ho Kim, April Brown, Yang Yang, Henry O Everitt, Gorden Videen, Stanley P. Burgos, Rene de Waele, Albert Polman, Harry A. Atwater, Wei Ting Chen, Kuang Yu Yang, Chih Ming Wang, Yingzhou Yao Wei Huang, Greg Sun, I. Da Chiang, Chun Yen Liao, Wei Lun Hsu, Hao Tsun Lin, Shulin Sun, Lei Zhou, Ai Qun Liu, Din Ping Tsai, J Homola, I Koudela, S S Yee, Nicholas S. King, Yang Li, Ciceron Ayala-Orozco, Travis Brannan, Peter Nordlander, Naomi J. Halas, Joseph R. Lakowicz, Zhipeng Li, Feng Hao, Yingzhou Yao Wei Huang, Yurui Fang, Peter Nordlander, Hongxing Xu, Syed Mubeen, Shunping Zhang, Namhoon Kim, Seungjoon Lee, Stephan Kramer, Hongxing Xu, N. M B Perney, Jeremy J. Baumberg, Majd E. Zoorob, M. D B Charlton, Caterina M. Netti, Timur Shegai, Bjorn Brian, Vladimir D Miljkovic, Mikael Kall, Vladimir D. Miljković, Kui Bao, Hongxing Xu, Peter Nordlander, Peter Johansson, Mikael Käll, Ting Xu, Amit Agrawal, Maxim Abashin, Kenneth J. Chau, and Henri J. Lezec. Surface plasmon resonance sensor based on diffraction gratings and prism coupler: sensitivity comparison. *Nano Letters*, 14(2):3531–3537, 2011.

[184] Nicholas S. King, Yang Li, Ciceron Ayala-Orozco, Travis Brannan, Peter Nordlander, and Naomi J. Halas. Angle- and spectral-dependent light scattering from plasmonic nanocups. *ACS Nano*, 5(9):7254–7262, 2011.

[185] Jeppe S. Clausen, Emil H??jlund-Nielsen, Alexander B. Christiansen, Sadegh Yazdi, Meir Grajower, Hesham Taha, Uriel Levy, Anders Kristensen, and N. Asger Mortensen. Plasmonic metasurfaces for coloration of plastic consumer products. *Nano Letters*, 14(8):4499–4504, 2014.

[186] Stanley P. Burgos, Rene de Waele, Albert Polman, and Harry A. Atwater. A single-layer wide-angle negative-index metamaterial at visible frequencies. *Nature Materials*, 9(5):407–412, 2010.

[187] Ludivine Malassis, Pascal Masse, Mona Tre, Patrick Weisbecker, Vasyl Kravets, Alexander Grigorenko, and Philippe Barois. Bottom-up Fabrication and Optical Characterization of Dense Films of Meta-Atoms Made of Core Shell Plasmonic Nanoparticles. 2013.

[188] J.J.Baumberg N.M.B. Perney M.E.Zoorob, M.D.B.Charlton, S. Mahnkopf and C.M.Netti. Tuning localized plasmons in nanostructured substrates for SERS. *ePrints Soton - University of Southampton*, 14(2):824–830, 2005.

[189] Joseph R. Lakowicz. Radiative decay engineering 3. Surface plasmon-coupled directional emission. *Analytical Biochemistry*, 324(2):153–169, 2004.

[190] Kui Bao, Hongxing Xu, Peter Nordlander, Peter Johansson, and K Mikael. Unidirectional Broadband Light Emission from Supported. *Nano*, pages 706–711, 2011.

[191] Zhipeng Li, Feng Hao, Yingzhou Huang, Yurui Fang, Peter Nordlander, and Hongxing Xu. Directional light emission from propagating surface plasmons of silver nanowires. *Nano Letters*, 9(12):4383–4386, 2009.

[192] Timur Shegai, Bjorn Brian, Vladimir D Miljkovic, and Mikael Kall. Angular Distribution of Surface-Enhanced Raman Scattering from Individual Au Nanoparticle Aggregates. *ACS Nano*, 5(3):2036–2041, 2011.

[193] Makoto Akagi, Sayaka Yanagida, and Atsuo Yasumori. Fabrication of LSPR sensor using porous titania-glass composite loading Au nanoparticles by photocatalytic deposition method. *Procedia Engineering*, 36:154–159, 2012.